Cherenkov Radiation by Particles Traversing the Background Radiation[1]

I. M. Dremin

Lebedev Physical Institute, Russian Academy of Sciences, Moscow, 119991 Russia
e-mail: dremin@lpi.ru
Received January 15, 2002

High-energy particles traversing the Universe through cosmic microwave background radiation can, in principle, emit Cherenkov radiation. It is shown that the energy threshold for this radiation is extremely high and its intensity would be too low due to the low density of the "relic photons gas" and very weak interaction of two photons. © *2002 MAIK "Nauka/Interperiodica".*

PACS numbers: 13.85.Tp; 41.60.Bq; 98.70.Vc

Recently, particles with energies exceeding 10^{20} eV were observed in cosmic ray studies. Their sources have not yet been identified, but they most likely originate outside of our galaxy. One could hope that some knowledge about the distance from these sources would be possible to obtain, in principle, from studies of Cherenkov radiation by such particles, since its intensity is proportional to the distance covered by a particle.

Let us consider Cherenkov radiation by a high-energy particle traversing the "gas" of relic photons with a temperature of 2.73 K. Even though the density ν of such photons is very low in the Universe $\nu \approx 500$ photons/cm^3, the particle path could be rather large, up to tens Mpc (1 Mpc $\approx 3 \times 10^{24}$ cm), and one could hope to register its Cherenkov radiation because the intensity is proportional to the path length.

The necessary conditions for Cherenkov radiation to be observed are the excess of the index of refraction n over 1; i.e.,

$$\Delta n = n - 1 > 0 \tag{1}$$

and the real emission angle, given by the formula

$$\cos\theta = 1/\beta n, \tag{2}$$

where $\beta = v/c = \sqrt{1 - m^2/E^2}$ (m, E are the particle mass and energy). For small values of m/E and Δn, one gets

$$\theta \approx \sqrt{2\Delta n - m^2/E^2}. \tag{3}$$

From this, the condition for the energy threshold E_{th} is written as

$$E \geq E_{\text{th}} = m/\sqrt{2\Delta n}. \tag{4}$$

It is easily seen that the threshold can become very high for small Δn.

The number of Cherenkov photons emitted by a particle with the electric charge e in the interval of frequencies $d\omega$ from the path length dl is given by the common expression [1]

$$dN/d\omega dl = 2\alpha\Delta n, \tag{5}$$

where the fine-structure constant $\alpha = e^2 \approx 1/137$. Thus, all physical characteristics of the process are determined by the value Δn. The intensity of the radiation (5) decreases with the threshold energy (4) increase:

$$dN/d\omega dl = \frac{\alpha m^2}{E_{\text{th}}^2}. \tag{6}$$

Surely, it is possible to use the notion of the medium (and, consequently, the macroscopic approach) only in the case of extremely long-wavelength radiation for the very diluted gas of relic photons. At the same time, it is well known that in usual media the value of Δn is uniquely related to the polarization operator of the medium. If this relation is also valid in the case treated here, one must consider the polarization operator of the light–light scattering or the real part of the forward elastic light–light scattering amplitude $\mathrm{Re}\,F(\omega, 0^0)$. For the index of refraction slightly different from unity[2], this relationship is given in the quantum scattering theory by the common formula [2, 3]:

$$\Delta n = \frac{2\pi\nu}{\omega^2}\mathrm{Re}\,F(\omega, 0^0), \tag{7}$$

where the elastic scattering amplitude of the two gamma-ray quanta $F(\omega)$ has been normalized to the

---

[1] This article was submitted by the author in English.

[2] The more general formula of Lorentz–Lorentz (see [2], p. 693) can be applied without this restriction.

total cross section $\sigma_{\gamma\gamma}(\omega)$ according to the optical theorem

$$\operatorname{Im} F(\omega, 0^0) = \frac{\omega}{4\pi}\sigma_{\gamma\gamma}(\omega). \tag{8}$$

Using these formulas, one easily gets

$$\Delta n = \nu\sigma_{\gamma\gamma}\rho/2\omega, \tag{9}$$

where $\rho = \operatorname{Re} F(\omega, 0^0)/\operatorname{Im} F(\omega, 0^0)$. From this and from Eq. (5), it follows that

$$dN/d(\ln\omega)dl = \alpha\nu\sigma_{\gamma\gamma}\rho, \tag{10}$$

and

$$E_{\text{th}} = m\sqrt{\omega}/\sqrt{\nu\sigma_{\gamma\gamma}\rho}; \tag{11}$$

i.e., the radiation threshold increases with the energy of the registered quanta.

The impressive strong limit is imposed on the energy threshold for Cherenkov radiation in the gas of relic photons. In electrodynamical processes, the total cross section $\sigma_{\gamma\gamma}$ reaches its maximum value of about 1.6 μb at the total energy of the two photons in their center-of-mass system $\omega_c \approx 3m_e$ where the electron mass is $m_e \approx 0.5$ MeV (see [4, 5]). At lower energies, below the threshold for the creation of the electron–positron pair (in particular, for a visible light), only elastic scattering is important, the real part of the amplitude dominates, and the cross section decreases at $\omega \longrightarrow 0$ proportionally to ω_c^6 (see the discussion at the end of the paper). At high energies, as seen from Eq. (9), the value of Δn tends to zero at $\omega \longrightarrow \infty$, and, therefore, the decline from the linear dispersion law $\omega = k$ can become noticeable only in the region near the maximum of the cross section $\sigma_{\gamma\gamma}$.

The CM energy of the two-photon system varies from 0 (when photons move in the same direction in the laboratory system) to its maximum value

$$\omega_c = 2\sqrt{\omega\omega_r}, \tag{12}$$

when the relic photon with energy ω_r moves in the laboratory system in the opposite direction to the emitted quantum with energy ω. For the relic photons $\omega_r \approx 2.4 \times 10^{-4}$ eV. Thus, the energy $\omega_c \approx 3m_e$ can only be achieved if the particle emits quanta with the energy

$$\omega = \omega_c^2/4\omega_r \approx 2 \times 10^{15} \text{ eV}. \tag{13}$$

First, let us consider the high-energy quanta which can create the electron–positron pairs in the cosmic microwave background radiation. In this case of very energetic radiation quanta, $\Delta n < 10^{-48}$ if one inserts high-energy values of $\rho \sim 0.1$. Then, for the proton with mass $m = 1$ GeV one gets an estimate

$$E_{\text{th}} > 10^{33} \text{ eV}. \tag{14}$$

The particles with such high energy have not yet been observed anywhere. Such a low index of refraction and, correspondingly, a high value of the energy threshold are determined by the low density of relic photons in the Universe and by the small total cross section of the photon–photon interaction.

The estimate of the upper limit of the intensity of the high-energy Cherenkov radiation at the path length L

$$N < \alpha\nu\sigma_{\gamma\gamma}L \tag{15}$$

is obtained from Eq. (10), if one takes into account that $\Delta\omega/\omega < 1$ and $\rho < 1$. If the path, from which the radiation is collected, is equal to $L \sim 1$ Mpc $\sim 3 \times 10^{24}$ cm and the maximum value of $\sigma_{\gamma\gamma}$ is about 1.6 μb (see [4, 5]), then for $\nu \approx 500$ photons/cm^3 the following upper limit on the number of emitted quanta is imposed according to Eq. (15):

$$N < 3 \times 10^{-5}. \tag{16}$$

Thus, the intensity of the high-energy Cherenkov radiation in the gas of relic photons is too low to be observable even if a proton passes through the Universe along hundreds of Mpc. For a primary nucleus, one should insert its total charge into Eq. (5), and, therefore, the intensity of radiation increases in proportion to the nucleus charge squared. However, the total threshold energy increases proportionally to its mass number, so that the threshold is much higher for nuclei compared to protons. At the same time, let us note that, according to Eq. (4), the threshold energy per nucleon of a nucleus is only determined by the value of Δn and, therefore, it is the same for all nuclei.

Some contribution to the polarization operator of the light–light scattering is, in principle, provided by the hadronic component of the photon structure function as well. It can be accounted for in the framework of the vector dominance model when the quanta are transformed into virtual ρ mesons which interact resonantly. The real part of the scattering amplitude is necessarily positive in one of the halves of the resonance peak, as clearly follows from the Breit–Wigner formula. The cross section $\sigma_{\gamma\gamma}$ slightly increases. Nevertheless, this does not lead either to a diminished threshold value in Eq. (14) or to an increased intensity of Cherenkov radiation because of the increase of ω due to ω_c increasing up to the values of the order of the ρ-meson mass. The hadronic contribution to the ratio $\rho = \operatorname{Re} F/\operatorname{Im} F$ can also be positive at higher energies, as is well known from experiments in all studied hadronic reactions, in complete accordance with predictions of dispersion relations. However, the threshold of the radiation again increases in this case due to the further increase of the required values of ω_c.

The estimates have shown that the above conclusions are "protected" by several orders of magnitude, as is already seen from Eqs. (14) and (16), and, therefore, they are robust.

Let us estimate the absorption of Cherenkov radiation at cosmic distances. For a plane wave e^{ikr}, it is given by the factor

$$\exp[-\omega L \operatorname{Im} n(\omega)] \approx \exp[-\nu\sigma_{\gamma\gamma}L/2], \qquad (17)$$

from which the absorption length L_{abs} is estimated as

$$L_{\text{abs}} = 2/\nu\sigma_{\gamma\gamma} > 2 \times 10^{27} \text{ cm.} \qquad (18)$$

The absorption length of the gamma-ray quantum in the relic radiation gas depends on the energy of the gamma-ray quantum only due to the cross section energy dependence, and it is so large that the damping of Cherenkov radiation can be neglected for the distances shorter than thousands of Mpc. Correspondingly, the energy losses, which determine the redshift, are very small at such "short" distances $L \ll L_{\text{abs}}$:

$$\frac{\Delta\omega}{\omega} = 1 - \exp\left(-\frac{\nu\sigma_{\gamma\gamma}L}{2}\right) \approx \frac{\nu\sigma_{\gamma\gamma}L}{2} \ll 1. \qquad (19)$$

Thus, the final conclusion is that the high-energy Cherenkov radiation by particles traversing the gas of relic photons is impossible to observe, first of all, because until now have been detected no particles with such high energies in nature exceeding the required energy threshold. Even if such particles were registered, the intensity of the high-energy Cherenkov radiation would, possibly, be too low to detect it.

The principal possibility of Cherenkov radiation by a charged particle in intergalactic space is, however, not excluded if there exists "an intergalactic medium component" with a higher density and a larger cross section of interaction with photons.

Another possibility is related to studies of quanta with energies lower than the threshold for creation of the electron–positron pair; i.e., for $\omega < 10^{15}$ eV. Even though the cross section decreases, the ratio ρ becomes very large. To estimate the index of refraction for such quanta, the classical consideration with Maxwell equations and dispersion relations [6] or the effective lagrangian with 4-photon interaction [7], describing the deviation from the classical theory by quantum effects, has been used. More optimistic estimates of $\Delta n \sim 10^{-41}$ follow, e.g., from Fig. 2 of [6], where, in our notation, the variables k and z read

$$k = m_e^4/16\pi^2\alpha^2\nu\omega_r \approx 8 \times 10^{40};$$
$$z = m_e^2/\omega\omega_r = 4m_e^2/\omega_c^2. \qquad (20)$$

This increase of Δn is due to the much larger values of ρ. This would lead to a lower threshold $E_{\text{th}} > 10^{29}$ eV. Nevertheless, this value of the threshold energy is still very high. The intensity of radiation could, however, become quite noticeable $N \sim 10$. In [7], the value of Δn at low energies was estimated at 4.7×10^{-43}. Let us remember that the notion of the medium in the classical approach can be used when the wavelength of the impinging photon is larger than typical distances inside the medium.

At the same time, Δn increases [7] with the temperature T in equilibrium as T^4. Therefore, at the early stage of the Universe, when the cosmic microwave background radiation separated from matter at a temperature of about 3000 K, the index of refraction was $\Delta n \sim 10^{-30}$; i.e., the threshold energy was $E_{\text{th}} \sim 10^{24}$ eV. This estimate is closer to realistic but still rather high energies.

Thus, the final conclusion about the extremely high-energy threshold for Cherenkov radiation in the cosmic microwave background radiation is left intact.

In laboratory, Cherenkov radiation by a particle traversing the "photon medium" can be observed for high-energy electron beams colliding with optical laser bunches. The corresponding estimates are $\Delta n \sim 6.2 \times 10^{-10}$, $E_{\text{th}} = \gamma_{\text{th}}m_e \sim 14$ GeV, and $\theta_{\text{max}} \sim \gamma_{\text{th}}^{-1} \sim 3.5 \times 10^{-5}$. It can be used for beam energy measurements, for tests of laser bunch parameters, and for an understanding of the "photon medium" properties (see hep-ph/0202060).

REFERENCES

1. I. E. Tamm and I. M. Frank, Dokl. Akad. Nauk SSSR **14**, 107 (1937); I. E. Tamm, J. Phys. (Moscow) **1**, 439 (1939).

2. M. L. Goldberger and K. M. Watson, *Collision Theory* (Wiley, New York, 1964; Mir, Moscow, 1967), pp. 689, 693, 712.

3. I. M. Dremin, Pis'ma Zh. Éksp. Teor. Fiz. **30**, 152 (1979) [JETP Lett. **30**, 140 (1979)]; Yad. Fiz. **33**, 1367 (1981) [Sov. J. Nucl. Phys. **33**, 726 (1981)].

4. R. Karplus and M. Neuman, Phys. Rev. **83**, 776 (1951).

5. B. De Tollis, Nuovo Cimento **35**, 1182 (1965).

6. V. A. Maisheev, Zh. Éksp. Teor. Fiz. **112**, 2016 (1997) [JETP **85**, 1102 (1997)].

7. M. Thoma, Europhys. Lett. **52**, 498 (2000).

Selective Photochemical Isotope "Burning" upon the Interaction of Resonant Laser Radiation with Atoms

P. A. Bokhan, D. E. Zakrevskiĭ, and N. V. Fateev*

Institute of Semiconductor Physics, Siberian Division, Russian Academy of Sciences,
pr. Akademika Lavrent'eva 13, Novosibirsk, 630090 Russia
*e-mail: fateev@isp.nsc.ru
Received December 25, 2001

The method of laser isotope separation based on selective excited-atom "burning" in a flow with buffer and reagent gases was implemented experimentally for zinc and rubidium. Selective excitation of isotopes was accomplished by the one-photon method using weak absorption lines and at the edge of the Doppler contour of atomic absorption with small isotope shift. © *2002 MAIK "Nauka/Interperiodica".*

PACS numbers: 28.60+s; 32.80-t; 42.62.Fi

The traditional methods of laser isotope separation [1] encounter considerable difficulties for many elements. First, their isotopic splitting is masked by the Doppler contour of spectral lines. In such a situation, the photoexcitation selectivity is enhanced by the traditional methods of absorption line narrowing: the atomic-beam method and the method of two-photon excitation in a standing light wave. For some atoms, these methods are inefficient. On the one hand, they are poorly accommodated even at cooled surfaces, as a result of which a well-collimated atomic beam is hard to obtain [2]. On the other hand, two-photon excitation requires the presence of two high-power tunable UV sources [3]. This renders the laser isotope-separation setup too complex and expensive. Second, even for a good selectivity and efficient excitation of low-lying working states, one does not always succeed in choosing the appropriate pathway for the ionization or transfer of a required isotope to the next excited levels.

In this work, a different method of isotope separation (two different examples of excitation) is demonstrated experimentally for the zinc and rubidium atoms and, presumably, for many other elements. The method is based on the following principles.

1. A mixture with natural-abundance isotopes in an atomic flow with inert buffer gas is excited. The drift time across the region of interaction with laser radiation is 1 s, and the number of collisions with the atoms of buffer gas is as high as 10^7. The large time of interaction with laser radiation and the large number of collisions allow the use of weak absorption lines and weak hyperfine-structure components (the populations have time to mix during the drift time) of odd isotopes to accomplish the 100% excitation of the required isotope during the drift.

2. A fast chemical reaction between the excited atoms and the molecules of reagent gas is necessary.

The products of this reaction must deposit ("burn") on the walls in the separating chamber. For the burning to be efficient, the conditions

$$k^* n\tau > 1, \quad kn\tau \ll 1, \tag{1}$$

should be met, where k^* and k are the reaction rate constants for the excited and unexcited atoms, respectively; n is the concentration of the reagent gas; and τ is the excited-state lifetime.

3. Single-photon isotope excitation. The transitions with small oscillator strengths are preferable. In this case, the excited-state lifetime is large and, hence, condition (1) can easily be fulfilled. In addition, for the elements with Doppler-masked isotope shifts, narrowband laser radiation can be used to provide velocity-selective excitation of the inhomogeneously broadened absorption contours [4]. In this case, only those atoms interact with the light field which have a certain velocity projection v onto the wave propagation direction:

$$|v_0 - v + v_0 v/c| \le \gamma, \Delta v, \tag{2}$$

where v_0 is the central frequency of the absorption line; v and Δv are the frequency and the width of the emission line, respectively; and γ is the homogeneous width of the absorption line. If the Doppler broadening is much larger than the homogeneous width, the frequency dependence of the absorption coefficient α has the form [4]

$$\alpha = \alpha_0 \exp[-4\ln 2((v - v_0)/\Delta v_d)^2], \tag{3}$$

where α_0 is the absorption coefficient at the line center and Δv_d is the Doppler width.

For a mixture of atoms and their isotopes, the absorption contour represents the sum of coefficients (3) with corresponding v_0's and weights proportional to the isotope percentages. If the laser frequency is tuned

to the isotope absorption edge, the contribution from other isotopes becomes small. In this case, the overall absorption coefficient drops materially, but the long interaction time between the laser radiation and atoms provides 100% excitation efficiency for the desired isotope, if the experimental parameters are properly chosen.

In the experiments, Zn was separated in a quartz tube 60 cm in length and 3 cm in diameter and Rb was separated in a glass tube, which were heated by an external furnace and through which a gas flow of atoms with argon and reagent-gas molecules was passed. The mixture pumping rate was ≥ 0.5 l/s, the argon pressure was (1–2) torr, and the concentration of reagent gas was $\approx 10^{16}$ cm^{-3}. The isotopes of interest entered the separation region from a reservoir heated by a separate furnace to the temperature ensuring the desired atomic concentration in the separation region. For Zn, the isotopic composition was analyzed either using probe radiation or by mass spectrometry of atoms deposited in a collector chamber, which was maintained at room temperature and into which the mixture flow was admitted. To analyze the isotopic composition of Rb, semiconducting laser probing in the region of the Rb $5S_{1/2}$–$5P_{3/2}$ transition (D_2 line; $\Delta\nu = 80$ MHz and $\lambda = 780$ nm) was performed in the direction perpendicular to the atomic flow at the end of the separation region.

The Zn atoms were excited by the pumping laser along the flow in the separation region via the intercombination transition $4s^{2}\,^1S_0$–$4p^3 P_1^0$ ($\lambda = 307$ nm), and the Rb atoms were excited to the Rydberg state $11P_{3/2}$ ($\lambda = 311$ nm) by a source of narrow-band tunable pulsed radiation described in [5]. The average laser output was ~2 W, and the beam diameter was ~1 cm at a repetition rate $f = 12$ kHz, a pulse duration of 10 nm, and a radiation line width $\Delta\nu = 45$ MHz. In this excitation scheme, the lifetimes of the upper excited states are comparatively long: $\tau = 10.5$ μs for Zn, and $\tau = 0.55$ μs for Rb. These values were obtained under real experimental conditions by measuring the luminescence decay times for the excited levels in the absence of reagent gas in the separation region.

In Fig. 1, the experimental absorption spectrum in the region of the Zn $4s^{2}\,^1S_0 \longrightarrow 4p^3 P_1^0$ transition at temperature $T = 350°$C is shown together with the calculated spectra (3) of the major Zn isotopes and the calculated overall absorption contour. One can see from Fig. 1 that the isotopic shifts are much smaller than the Doppler width. If the frequency of a monochromatic radiation with $\Delta\nu \ll \Delta\nu_d$ is detuned from the center of the Zn Doppler absorption contour, the absorption coefficients for different isotopes will be different. One may choose a radiation frequency so that only one of the isotopes is preferably excited. Figure 2 shows the spectra of Rb $5S_{1/2}$–$11P_{3/2}$ absorption in the separation chamber recorded from the radiation absorption and luminescence signal. Both spectra were identical. The spectral
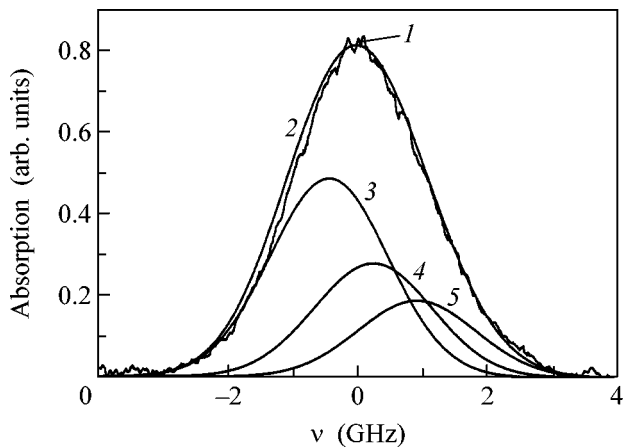

Fig. 1. Absorption spectrum in the region of the Zn $4s^{2}\,^1S_0 \longrightarrow 4p^3 P_1^0$ transition ($\lambda = 307$ nm) in a gas flow: (1) experimental spectrum at 350°C; (2) spectrum calculated by Eq. (3) for the same temperature; and (3, 4, 5) spectra calculated, respectively, for the ^{64}Zn, ^{66}Zn, and ^{68}Zn isotopes separately.
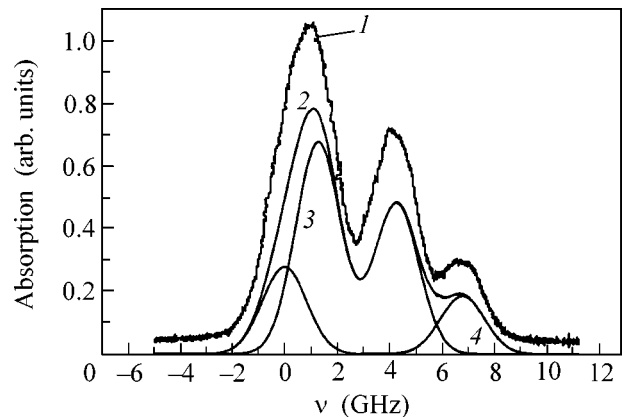

Fig. 2. Absorption spectrum in the region of the Rb $5S_{1/2} \longrightarrow 11P_{3/2}$ transition ($\lambda = 311$ nm) in a gas flow: (1) experimental spectrum at 120°C; (2) spectrum calculated for the same temperature; and (3, 4) spectra calculated, respectively, for the ^{85}Rb and ^{87}Rb isotopes separately.

behavior did not change up to an Ar pressure of ~5 torr and a Rb concentration of ~10^{13} cm^{-3}. One can see that the calculated and experimental absorption spectra (3) agree well for the operating temperature of 120°C. The calculated absorption spectra for the individual hfs components of the ^{85}Rb and ^{87}Rb isotopes are also given in Fig. 2. The excitation from these hfs components ($F = 1 \longrightarrow F = 0, 1, 2$ for ^{87}Rb and $F = 2 \longrightarrow F = 1, 2, 3$ for ^{85}Rb) provides a good selectivity for a chosen isotope.
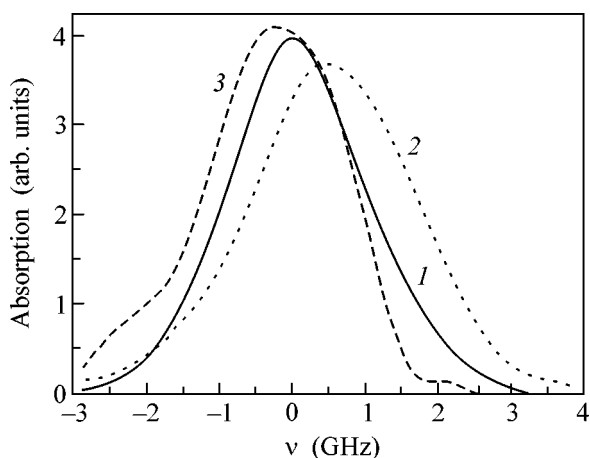
Fig. 3. Absorption of the probe laser radiation by the Zn atoms in the collector chamber in the region of $4s^2\,^1S_0 \longrightarrow$ $4p^3\,P_1^0$ ($\lambda = 307$ nm): (*1*) absorption spectrum without laser pumping in the separation region; (*2*) spectrum in the presence of laser pumping at a frequency detuned by (–)2 GHz from the absorption line center (scaled by a factor of 8); (*3*) pump frequency is detuned to (+)2 GHz from the line center (scaled by a factor of 20).
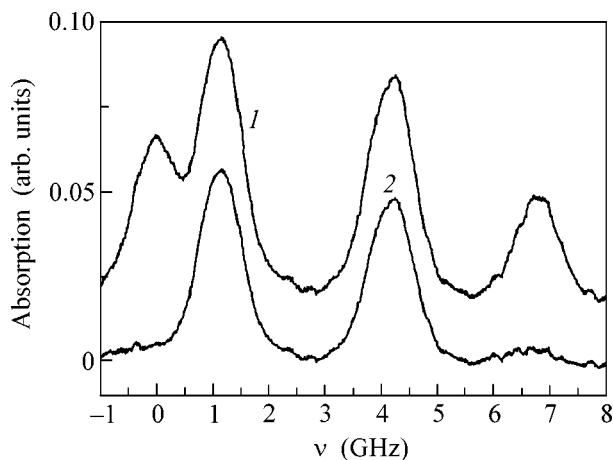

Fig. 4. Absorption of the resonance radiation in the region of the Rb $5S_{1/2}$–$5P_{3/2}$ transition ($\lambda = 780$ nm) at the end of the separation region: (*1*) without pumping laser radiation in the separation region; (*2*) in the presence of pumping radiation tuned to the transition frequency of the ^{87}Rb hfs components.

The reagent gas was chosen after testing various molecules. The reactions of many excited atoms with various hydrocarbons were examined earlier, e.g., in [6–8]. However, the products of those reactions were unstable and decomposed within hundreds of microseconds [6]. For our purposes, we have chosen complex oxygen-containing molecules: diethyl ether $(C_2H_5)_2O$ and methanol CH_3OH. In this case, the reactions of

excited-state atoms with reagent-gas molecules yield the stable ZnO compound, which is deposited on the walls of the separation chamber; i.e., the reaction proceeds according to the scheme

$$A^* + M \longrightarrow AO + R. \qquad (4)$$

The rate constants for reactions with reagent gas were determined from the luminescence time decay at different pressures of reagent gas to give $k^* = 1.61 \times 10^{-9}$ cm^3/s for the reaction of Zn($4p^3\,P_1^0$) with diethyl ether ($k < 10^{-14}$ cm^3/s) and $k^* = 1.47 \times 10^{-9}$ and 8.4×10^{-10} cm^3/s for the reactions of Rb($11P_{3/2}$) with, respectively, metanol and diethyl ether. For Rb, the value of k is more than three orders of magnitude smaller than k^*.

If the frequency of the pumping laser is tuned to the center of the Zn Doppler contour, virtually 100% of the atoms are burned in the collector chamber. This fact is evidence of the efficient excitation of Zn atoms in the separation chamber and the efficiency of the chemical reaction. As the laser frequency is detuned from the center of the Doppler contour, the absorption line in the collector chamber deforms. The corresponding experimental results obtained for an atomic concentration of $\approx 10^{13}$ cm^{-3} in the separation region are presented in Fig. 3. For a detuning of (–)2 GHz, the Doppler maximum shifts to the right. This is caused by the preferred excitation of ^{64}Zn and its subsequent burning (see Fig. 1). The reverse situation occurs if the radiation frequency is detuned by (+)2 GHz. It also follows from Fig. 3 that the number of burned atoms detected in the collector chamber exceeds the number of excited atoms in the separation chamber. This is likely due to the secondary reactions between the radical products and the unexcited atoms. A comparison of the experimental and calculated shifts of the Doppler maximum showed that more than 95% of the ^{64}Zn isotope is burned in the separation chamber. The same results were obtained by the mass spectrometric analysis of Zn deposited on the collector chamber walls. The maximum product yield was ~1 g of a substance for an exposure of 3 h.

The Rb $5S_{1/2}$–$5P_{3/2}$ absorption spectra recorded at the end of the separation chamber are shown in Fig. 4 for a Rb concentration of $\approx 10^{12}$ cm^{-3}. These spectra can be used to judge the isotopic composition of Rb atoms. Experimental results show (Fig. 4) that, as the frequency of exciting radiation is tuned to the fourth absorption peak ($F = 1 \longrightarrow F = 0, 1, 2$) of the ^{87}Rb isotope (Fig. 2), its content at the end of the separation chamber decreases to a level of less than ~10% of its initial value.

In summary, a new method of isotope separation based on selective excited-atom "burning" in a flow of argon atoms and reagent gas has been demonstrated experimentally. Its main advantage over the previous methods consists in the one-photon excitation and the high concentration of separated isotopes in the separation chamber.

We are grateful to A.Yu. Stepanov, V.A. Kim, V.A. Kochubeĭ, and N.A. Yudin for their assistance.

REFERENCES

1. V. S. Letokhov, *Nonlinear Selective Photoprocesses in Atoms and Molecules* (Nauka, Moscow, 1983).

2. P. Campbell, J. Billowes, and I. S. Grant, J. Phys. B **30**, 2351 (1997).

3. P. A. Bokhan, V. V. Buchanov, D. É. Zakrevskiĭ, *et al.*, Pis'ma Zh. Éksp. Teor. Fiz. **71**, 705 (2000) [JETP Lett. **71**, 483 (2000)].

4. V. S. Letokhov and V. P. Chebotaev, *Nonlinear Laser Superhigh-Resolution Spectroscopy* (Nauka, Moscow, 1990).

5. P. A. Bokhan, D. É. Zakrevskiĭ, S. A. Kochubeĭ, *et al.*, Kvantovaya Élektron. (Moscow) **31**, 132 (2001).

6. W. H. Breckenridge, T. W. Broadbent, and D. S. Moore, J. Phys. Chem. **79**, 1233 (1975).

7. H. Umemoto, S. Tsunashima, H. Ikeda, *et al.*, J. Chem. Phys. **101**, 4803 (1994).

8. Li-Hsyan Fan, Jye-Jong Chen, Yann-Yow Lin, and Wei-Tzou Luh, J. Phys. Chem. A **103** (10), 1300 (1999).

Translated by V. Sakun

Optical Chaos in Nonlinear Photonic Crystals[1]

K. N. Alekseev[1, 2, 3, *] and A. V. Ponomarev[3, 4]

[1] *Department of Physical Sciences, University of Oulu FIN-90014, Finland*
*e-mail: Kirill.Alekseev@oulu.fi
[2] *Max-Planck-Institute für Physik komplexer Systeme, D-01187 Dresden, Germany*
[3] *Theory of Nonlinear Processes Laboratory, Kirensky Institute of Physics, Russian Academy of Sciences, Krasnoyarsk, 660036 Russia*
[4] *Department of Physics, Krasnoyarsk State University, Krasnoyarsk, 660041 Russia*
Received January 9, 2001

We examine the spatial evolution of lightwaves in a nonlinear photonic crystal with a quadratic nonlinearity, when a second harmonic and a sum-frequency generation are simultaneously quasi-phase-matched. We find the conditions for a transition to Hamiltonian chaos for different amplitudes of lightwaves at the crystal boundary. © 2002 MAIK "Nauka/Interperiodica".

PACS numbers: 42.65.Sf; 42.70.Mp; 42.65.Ky; 42.65.Hw

Wave mixing in nonlinear optical materials is a basis of modern optical sciences and technologies. Cascading several wave-mixing processes in the same low-loss material, one can, in principle, achieve a high efficiency using a large value of the lowest order optical nonlinearity. The theoretical investigations of cascading of several scalar optical three-wave-mixing processes in bulk materials with $\chi^{(2)}$ nonlinearity has a long history [1]. In particular, Akhmanov and coworkers found the efficiency of third harmonic generation (THG) via cascading of a second harmonic generation (SHG) and a sum-frequency mixing (SFM) in a quadratic medium [2], while Komissarova and Sukhorukov described an efficient parametric amplification at a high-frequency pump in the same system [3]. Obviously, the observation of these nonlinear effects demands the simultaneous fulfillment of phase-matching conditions for several parametric processes as perfectly as possible. On the other hand, it was shown later that the systems for which several wave-mixing processes can be simultaneously phase-matched are in general nonintegrable; therefore, the competition of two (or more) parametric processes can often result in the chaotic spatial evolution of lightwaves [4, 5]. However, until recently, it was unclear as to how one can achieve phase-matching for several processes in a *homogeneous medium* employing traditional techniques, such as the use of birefringence in ferroelectric crystals.

The solution of this problem has been found rather recently [6–8]; it consists in the introduction of different types of *artificial periodicity* of a nonlinear medium, which results in the formation of nonlinear 1D and 2D superstructures termed *optical superlattices* [9] or *nonlinear photonic crystals* (NPCs) [10]. In NPCs, there is a periodic (or quasiperiodic) spatial variation of the nonlinear susceptibility tensor, while the linear susceptibility tensor is constant.

In these engineered nonlinear materials, a phase mismatch between the interacting lightwaves could be compensated by the Bragg vector of NPC. The idea of this kind of *quasi-phase-matching* (QPM) was introduced by Bloembergen and coworkers many years ago [11]. However, only recently, the rapid progress in the fabrication of high-quality ferroelectric crystals with a periodic domain inversion has made the QPM method very popular [9, 12]. We should stress that the conditions for QPM may be fulfilled for several wave-mixing processes simultaneously; the QPM also has an advantage of using the largest nonlinear coefficient.

Nowadays, there are several experiments on the observation of third and fourth harmonics in different periodically or quasiperiodically poled ferroelectric crystals with $\chi^{(2)}$ nonlinearity [7, 13, 14], which clearly demonstrate the importance of multiple mixing in NPCs for potential applications. Modern theoretical activities on the nonlinear lightwaves interactions in NPCs are mainly focused on the studies of strong energy interchange between the waves [12] (this is a development of the earlier activities [2, 3]), as well as on the formation of spatial optical solitons [15].

In this work, we describe the effect of Hamiltonian optical chaos novel for the physics of NPCs. Namely, we show that spatial evolution of three light waves participating simultaneously in SHG and SFM under the conditions of QPM is chaotic for many values of the complex amplitude of the waves at the boundary of $\chi^{(2)}$-NPC. There also exists an integrable limit, where the evolution of waves is always regular regardless of the absolute values of their complex amplitudes. The inte-

---

[1] This article was submitted by the authors in English.

grable limit corresponds to the particular values of two combinations of wave phases at the boundary of nonlinear medium. In particular, the problem of THG belongs to the integrable limit; therefore, under the conditions of recent experiments [7, 13, 14], nonlinear light dynamics should always be regular. However, even a rather small change in amplitudes and phases of waves at the boundary of crystal, with respect to those considered in [7, 13, 14], should result in a transition to chaos.

We consider a spatial evolution of three copropagating plane waves

$$E = \frac{1}{2}\sum_{j=1}^{3} A_j \exp[j(i\omega t - k_j z)] + \text{c.c.}, \quad k_j = k(j\omega)$$

in a periodically poled crystal under the conditions where SHG, $\omega + \omega \longrightarrow 2\omega$, and SFM, $\omega + 2\omega \longrightarrow 3\omega$ take place simultaneously. Equations of motion for the slowly varying complex amplitudes A_l ($l = 1, 2, 3$) of the waves are [9, 12]

$$\frac{dA_1}{dz} = -i\beta_3 g(z)A_3 A_2^* e^{-i\Delta k_3 z} - i\beta_2 g(z)A_2 A_1^* e^{-i\Delta k_2 z},$$

$$\frac{dA_2}{dz} = -i2\beta_3 g(z)A_3 A_1^* e^{-i\Delta k_3 z} - i\beta_2 g(z)A_1^2 e^{i\Delta k_2 z}, \quad (1)$$

$$\frac{dA_3}{dz} = -i3\beta_3 g(z)A_1 A_2 e^{i\Delta k_3 z},$$

where $g(z)$ is a function equal to $+1$ (or -1) in a single positive (negative) polarization domain of the ferroelectric crystal. In this work, for the sake of simplicity, we consider only a periodic alternative domain superlattice with a spatial period Λ. However, $g(z)$ can be a quasiperiodic function in the case of nonlinear quasicrystals [8, 9]. Note that we consider a typical situation $\lambda \ll \Lambda$, where λ is a wavelength [9, 12, 14].

The coupling constants between waves β_2 and β_3 are defined as

$$\beta_{2,3} = \omega d_{\text{eff}}/cn_{2,3},$$

where $d_{\text{eff}} = 2\pi\chi^{(2)}$ and $n_j \equiv n(j\omega)$ ($j = 1, 2, 3$) are the refractive indices for the different waves. Of course, $n_1 \neq n_2 \neq n_3$ because of light dispersion. However, it can be shown that $\Delta n/n \simeq \lambda/\Lambda \ll 1$ under the conditions of QPM; therefore, in what follows we will take $\beta_2 = \beta_3 \equiv \beta$. Finally, the phase mismatches involved in Eqs. (1) are $\Delta k_2 = k_2 - 2k_1$ and $\Delta k_3 = k_3 - k_2 - k_1$. Let both these mismatches be compensated by a reciprocal lattice vector of NPC, that is

$$\Delta k_2 = 2\pi m_1/\Lambda, \quad \Delta k_3 = 2\pi m_2/\Lambda, \quad (2)$$

where $m_j = \pm 1, \pm 2, \pm 5, \dots$. The methods of achieving QPM for several parametric processes in a single NPC were recently discussed in [6, 8, 10] (theory) and [7, 13, 14] (experiment).

The dynamical system (1) together with the initial conditions, which in our case are the values of complex amplitudes at the boundary of NPC, $A_j(z = 0)$, completely determine the nonlinear spatial evolution of waves. Before specification of these initial conditions, we can further simplify the equations of motion. First, we introduce new scaled amplitudes $a_l = A_l/\sqrt{l}A_0$, where $l = 1, 2, 3$ and $A_0 \equiv \max(|A_1(0)|, |A_2(0)|, |A_3(0)|)$. Second, we make the Fourier series expansion of the function $g(z)$

$$g(z) = \sum_{n=1}^{\infty} \frac{4}{\pi n}\sin\left(\frac{2\pi n z}{\Lambda}\right),$$

where index n takes only odd values. Now we substitute this expansion into Eqs. (1), take into account the QPM conditions (2), and make an averaging of the resulting equations of motion over the short characteristic spatial scale $2\pi/\Lambda$. We have the following basic equations

$$\dot{a}_1 = -a_2 a_1^* - \xi a_3 a_2^*,$$

$$\dot{a}_2 = 0.5a_1^2 - \xi a_3 a_1^*, \quad (3)$$

$$\dot{a}_3 = \xi a_1 a_2,$$

where $\xi = \sqrt{3}\, m_2/m_3$ (m_j are the quasi-phase matching orders, see Eq. (2); we assume that $m_3 \geq m_2$). The overdot in Eqs. (3) means the derivative with respect to z/l_{nl} with a characteristic nonlinear length l_{nl}, defined as

$$l_{nl} = \frac{\pi m_2}{2\sqrt{2}}\frac{1}{\beta A_0}. \quad (4)$$

In the derivation of equations of motion (3), we removed all rapidly varying terms in performing the averaging over $2\pi/\Lambda$. It can be shown that such a procedure is correct if $l_{nl} \gg \Lambda$ [16].

Equations (3) can be represented in the canonical form with the Hamiltonian function

$$H = \left[-i\left(\xi a_1^* a_2^* a_3 + \frac{1}{2}a_1^{*2}a_2\right)\right] + \text{c.c.},$$

$$i\dot{a}_l = \frac{\partial H}{\partial a_l^*}, \quad i\dot{a}_l^* = -\frac{\partial H}{\partial a_l}. \quad (5)$$

In addition to the energy of wave interaction $E \equiv H$ (Eq. (5)), the dynamical system (3) has the integral of motion

$$|a_1|^2 + 2|a_2|^2 + 3|a_3|^2 = 1 \quad (6)$$

corresponding to the conservation of energy of noninteracting waves. In the general case, the system (3) does not have other global integrals of motion; thus, it is *nonintegrable* and should demonstrate *chaotic dynamics* for many initial conditions $a_l(0)$ [17, 18]. However, for some values of ξ and some specific initial conditions, an additional local integral of motion can arise. Let us
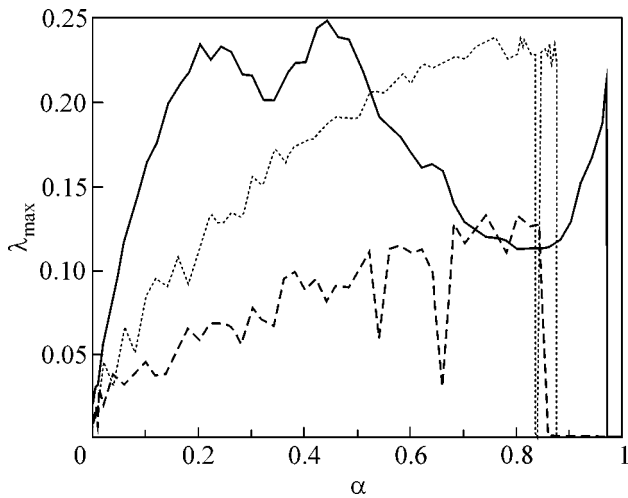
Fig. 1. Dependence of the value of the maximal Lyapunov exponent on the amplitude of the first wave at the boundary of optical superlattice α and for different phases: $\phi = -\pi/2$ (solid line), $\phi = -0.1$ (dotted line), and $\phi = -0.01$ (dashed line). The first-order QPMs (problem 1, set I).
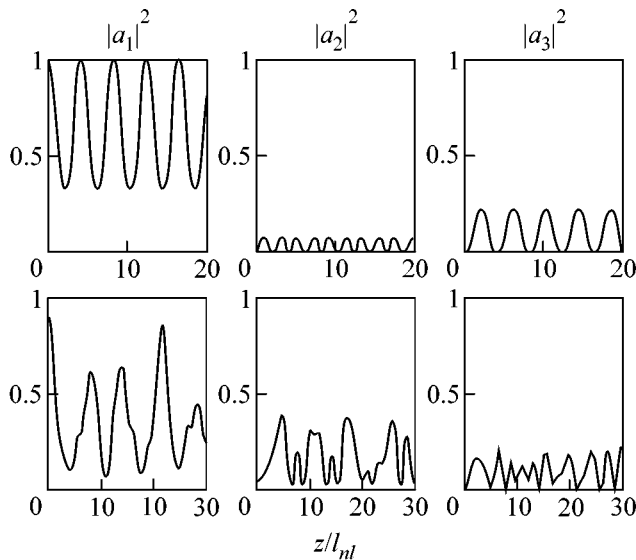

Fig. 2. Regular (upper) and chaotic (lower) spatial evolutions of scaled intensities of lightwaves at the first-order QPMs. For the upper subplot, $\alpha = 1$ and $\phi = 0$, while for the lower subplot, $\phi = 0.95$ and $\phi = \pi/2$.

list these cases, because they include physically important situations.

First, if one of the parametric processes, either SHG or SFM, is dominant ($\xi \ll 1$ or $\xi \gg 1$), then an additional integral of motion arises, which is of the Manley–Rowe type [12]. Second, the nonlinear dynamics strongly depends on the initial values of the two "resonant phases" $\psi_2(0)$ and $\psi_3(0)$, where

$$\psi_2 = 2\theta_1 - \theta_2, \quad \psi_3 = \theta_1 + \theta_2 - \theta_3, \qquad (7)$$

and θ_j ($j = 1, 2, 3$) are the lightwave phases; i.e., $a_j = |a_j|\exp(-i\theta_j)$. We found that, for $\psi_2(0) = \psi_3(0) = 0$, *the dynamics is always regular.* Moreover, using approaches [3, 19], it is possible to show that an additional local integral of motion exists in this case [20]. In particular, the problem of THG ($a_1(0) = 1$, $a_2(0) = a_3(0) = 0$) belongs to this class of initial conditions. Therefore, the spatial dynamics of lightwaves at THG is regular (cf. [21], where an analytic solution has been found).

We performed an intensive search of chaotic trajectories solving the equations of motion (3) numerically for two characteristic values of control parameter ξ that correspond to the experimental situations described in [7] and [13], correspondingly:

Set I: The QPMs of first order for both processes, $m_1 = m_3 = 1$, $\xi = \sqrt{3} \approx 1.73$;

Set II: The QPMs of the 9th and 33rd orders, $m_1 = 9$, $m_3 = 33$, $\xi = 3\sqrt{3}/11 \approx 0.472$.

We consider several types of initial conditions, which cover practically all physically interesting cases [note that all these initial conditions satisfy the restriction arising from the integral of motion (6)]:

Problem 1: $a_1(0) = \alpha$, $a_2(0) = [1 - \alpha^2]^{1/2} \times 2^{-1/2}\exp(-i\phi)$, $a_3(0) = 0$, where the real parameters ϕ and α vary in the ranges $-\pi \le \phi < \pi$ and $0 \le \alpha \le 1$, correspondingly. Obviously, here $|\psi_2(0)| = |\psi_3(0)| = |\phi|$.

Problem 2: $a_1(0) = [1 - 3\alpha^2]^{1/2} \times 3^{-1/2}\exp(-i\theta_1)$, $a_2(0) = [1 - 3\alpha^2]^{1/2} \times 3^{-1/2}\exp(-i\theta_2)$, $a_3(0) = \alpha \exp(-i\theta_3)$, where $-\pi \le \theta_j < \pi$ ($j = 1, 2, 3$) and $0 \le \alpha \le 3^{-1/2} \approx 0.57735$.

Problem 3: $a_1(0) = \alpha \exp(-i\theta_1)$, $a_2(0) = 0$, $a_3(0) = [1 - \alpha^2]^{1/2} \times 3^{-1/2}\exp(-i\theta_3)$, $-\pi \le \theta_j < \pi$ ($j = 1, 3$) and $0 \le \alpha \le 1$.

We start our analysis with problem 1. This set of initial conditions describes, in particular, the THG at $\alpha = 1$ ($\phi = 0$) and the parametric amplification with a low-frequency pump at $\alpha \ll 1$ [12]. In order to increase the efficiency of energy transformation from a basic wave of frequency ω to a wave of frequency 3ω, it was suggested recently that some nonzero signal at the frequency 2ω be mixed with a basic beam [22]. This kind of initial condition corresponds to $\alpha \longrightarrow 1$ (but $\alpha \ne 1$) with different values of phase ϕ.

To distinguish between regular and chaotic dynamics, we compute the maximal Lyapunov exponent λ_{max} for different values of initial lightwave amplitudes, α, and phases, ϕ. For chaos $\lambda_{max} > 0$, in contrast $\lambda_{max} = 0$ for a regular motion [18]. The dependence of λ_{max} on α for the first-order QPMs (set I) is depicted in Fig. 1. For $\phi = 0$, the initial values of resonant phases, $\psi_2(0)$ and $\psi_3(0)$, are zero, corresponding to the integrable limit with $\lambda_{max} = 0$ independently on the value of α (not shown in Fig. 1). However, even a small deviation from

the integrable limit, $|\psi_2(0)| = |\psi_3(0)| = |\phi| = 0.01$, results in chaotic motion for a quite wide range of initial conditions (dashed line). A further increase in the value of $|\phi|$ makes chaos more strong (dotted line, $|\phi| = 0.1$); the strongest chaos arises for $|\phi| = \pi/2$ (solid line), corresponding to the initial values of resonant phases $|\psi_{2,3}(0)|$ that are most distant from the integrable limit.

The motion is always regular for the standard THG ($\alpha = 1$), as well as for some range of α in the vicinity of $\alpha = 1$ (see the right side of Fig. 1). A regular spatial evolution of lightwaves for $\alpha = 1$ is shown in the upper subplot in Fig. 2. However, for $|\phi| = \pi/2$, strong chaos exists already for $\alpha \approx 0.95$, i.e., for $a_1(0) = 0.95$, $a_2(0) \approx 0.22i$, and $a_3(0) = 0$; see lower subplot in Fig. 2. Thus, the possibility of transition to chaos must be taken into account in the application of an additional pump of frequency 2ω in order to increase the efficiency of THG [22].

We now consider the situation corresponding to the left side of Fig. 1 with $\alpha \ll 1$. This is the parametric amplification with a low-frequency pump [12]. In this case, our analysis demonstrates that the evolution of waves is weakly chaotic for $|\psi_{2,3}(0)|$ distant from the integrable limit. In this regime, the Lyapunov exponent has some very small yet positive value; therefore, it is very difficult to distinguish between weak chaos and regular motion. In practical terms, it means that one needs to have a very long sample to see the differences between regular and weakly chaotic spatial evolutions of light waves.

We now turn to the consideration of nonlinear dynamics using the second set of QPM parameters but the same set of initial conditions (set II, problem 1). The main results on the transition to chaos are depicted in Fig. 3. Again, as in Fig. 1, $|\psi_2(0)| = |\psi_3(0)| = |\phi| = 0$ results in a regular motion, while motion is chaotic for many initial conditions if $|\phi| > 0$. However, the absolute values of the Lyapunov exponent are small: really, $\lambda_{max} \simeq 0.1$ in Fig. 1, but $\lambda_{max} \simeq 0.01$ in Fig. 3. Therefore, we conclude that the multiple interaction of waves employing high-order QPMs is more stable against a transition to chaos in comparison with the case of first-order QPMs.

We now consider a nonlinear dynamics in the case when some portion of the energy is presented at $z = 0$ in each of the interacting waves (Problem 2). We present our findings in Fig. 4. Strong chaos arises as soon as one of the resonant phases becomes different from the integrable limit $|\psi_{2,3}(0)| = 0$ ($|\psi_2(0)| = \pi$ and $|\psi_3(0)| = \pi/2$ for a solid line, $|\psi_2(0)| = \pi/2$ and $|\psi_3(0)| = 0$ for a dashed line). We should note that for the parameters corresponding to the solid curve in Fig. 4 strong chaos exists for almost all values of initial wave amplitudes α. Chaos is sufficiently weaker for the high-order QPMs in comparison with the case of first-order QPMs: *cf* a dashed line with a dashed and dotted line that correspond to the same values of phases θ_j but to the different sets of QPM parameters.
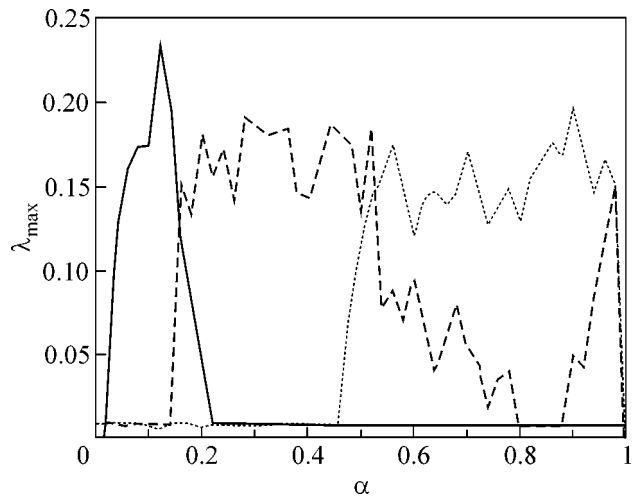
Fig. 3. The same as in Fig. 1 but for the high-order QPMs (problem 1, set II): $\phi = -\pi/2$ (solid line), $\phi = -0.1$ (dashed line), and $\phi = -0.01$ (dotted line).
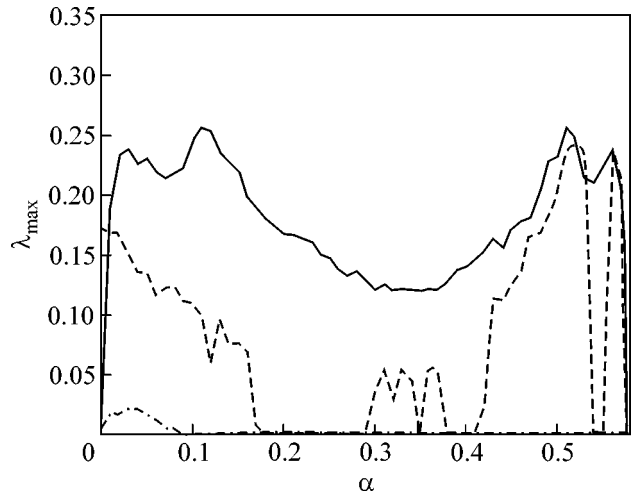

Fig. 4. Dependence of the value of the maximal Lyapunov exponent on the amplitude of the third wave at the boundary of optical superlattice α and for different phases and QPM orders (problem 2, sets I and II): $\theta_1 = \pi/2$, $\theta_2 = 0$, $\theta_3 = \pi$, first order QPMs (solid line); $\theta_1 = \theta_2 = \theta_3 = -\pi/2$, first order QPMs (dashed line); $\theta_1 = \pi/2$, $\theta_2 = 0$, $\theta_3 = \pi$, high order QPMs (dashed and dotted line).

Finally, we analyze the set of initial conditions termed as Problem 3. In particular, it includes the down conversion [3, 12] or, in other words, the fractional conversion $\omega \longrightarrow (2/3)\omega$ [19] in the case of $\alpha \ll 1$. For this set of initial conditions, we did not find visible regions of chaotic dynamics.

In order to reliably distinguish between regular and chaotic spatial evolutions of lightwaves in conditions of an experiment, one needs to have many characteristic nonlinear lengths, l_{nl}, on the total length of the crystal

L: $L/l_{nl} \gtrsim 10$ [4, 5]. Importantly, it appears possible to meet this condition in the typical NPCs. In actuality, for a periodically poled lithium niobate with a period $\Lambda = 30\,\mu m$, a crystal length $L \simeq 1$ cm, a nonlinear coefficient $d_{33} = 34$ pm/V [7, 13], and a light intensity $A_0^2 = 0.76$ GW/cm^2 ($\lambda = 1.064\,\mu m$) [23], we have $L/l_{nl} \simeq 100$. Moreover, chaos should be more easily observable in the GaAs optical superlattice with $d_{14} \geq 90$ pm/V [24].

In summary, we have shown that simultaneous multiwavelength generation in typical nonlinear photonic crystals is often chaotic. This fact must be taken into an account for the realization of compact laser multicolor sources for printers, scanners, and color displays based on quasi-phase-matched harmonics generation.

We should distinguish our results from a recent paper [25], where nonlinear spatial field dynamics and chaos were studied in a quadratic media with a periodic Bragg grating.

REFERENCES

1. S. A. Akhmanov and R. V. Khohlov, *Problems of Nonlinear Optics* (VINITI, Moscow, 1964; Gordon & Breach, New York, 1973).

2. S. A. Akhmanov, V. G. Dmitriev, and V. P. Modenov, Radiotekh. Élektron. (Moscow) **9**, 814 (1964).

3. M. V. Komissarova and A. P. Sukhorukov, Kvantovaya Élektron. (Moscow) **20**, 1025 (1993) [Quantum Electron. **23**, 893 (1993)].

4. K. N. Alekseev, G. P. Berman, A. V. Butenko, *et al.*, Kvantovaya Élektron. (Moscow) **17**, 42 (1990) [Sov. J. Quantum Electron. **20**, 359 (1990)]; J. Mod. Opt. **37**, 41 (1990).

5. N. V. Alekseeva, K. N. Alekseev, V. A. Balueva, *et al.*, Opt. Quantum Electron. **23**, 603 (1991).

6. A. L. Aleksandrovski, A. S. Chirkin, and V. V. Volkov, J. Russ. Laser Res. **18**, 101 (1997).

7. O. Pfister, J. S. Wells, L. Hollberg, *et al.*, Opt. Lett. **22**, 1211 (1997).

8. X. Liu, Z. Wang, J. Wu, and N. Ming, Phys. Rev. A **58**, 4956 (1998); K. Fradkin-Kashi and A. Ady, IEEE J. Quantum Electron. **35**, 1649 (1999); S. Saltiel and Yu. S. Kivshar, Opt. Lett. **25**, 1204 (2000).

9. Y. Y. Zhu and N. B. Ming, Opt. Quantum Electron. **31**, 1093 (1999).

10. V. Berger, Phys. Rev. Lett. **81**, 4136 (1998); N. G. R. Broderick, G. W. Ross, H. L. Offerhaus, *et al.*, Phys. Rev. Lett. **84**, 4345 (2000).

11. J. A. Armstrong, N. Bloembergen, J. Ducuing, and P. S. Pershan, Phys. Rev. **127**, 1918 (1962).

12. A. S. Chirkin, V. V. Volkov, G. D. Laptev, and E. Yu. Morozov, Kvantovaya Élektron. (Moscow) **30**, 847 (2000) [Quantum Electron. **30**, 847 (2000)] and references therein.

13. V. V. Volkov, G. D. Laptev, E. Y. Morozov, *et al.*, Kvantovaya Élektron. (Moscow) **25**, 1046 (1998) [Quantum Electron. **28**, 1020 (1998)].

14. M. L. Sundheimer, A. Villeneuve, G. I. Stegeman, and J. D. Bierlein, Electron. Lett. **30**, 1400 (1994); P. Baldi, C. G. Treviño-Palacios, G. I. Stegeman, *et al.*, Electron. Lett. **31**, 1350 (1995); S. N. Zhu, Y. Y. Zhu, and N. B. Ming, Science **278**, 843 (1997); X. Mu and Y. J. Ding, Opt. Lett. **26**, 623 (2001); G. Z. Luo, S. N. Zhu, J. L. He, *et al.*, Appl. Phys. Lett. **78**, 3006 (2001).

15. Yu. S. Kivshar, T. J. Alexander, and S. Saltiel, Opt. Lett. **24**, 759 (1999); I. Towers, A. V. Buryak, R. A. Sammut, and B. A. Malomed, J. Opt. Soc. Am. B **17**, 2018 (2000).

16. A. S. Chirkin and D. B. Yusupov, Kvantovaya Élektron. (Moscow) **9**, 1625 (1982) [Sov. J. Quantum Electron. **12**, 1041 (1982)].

17. J. Ford and G. H. Lansford, Phys. Rev. A **1**, 59 (1970).

18. A. J. Lichtenberg and M. A. Lieberman, *Regular and Stochastic Motion* (Springer-Verlag, New York, 1982; Mir, Moscow, 1984).

19. V. V. Konotop and V. Kuzmiak, J. Opt. Soc. Am. B **17**, 1874 (2000).

20. K. N. Alekseev, unpublished.

21. C. Zhang, S. X. Yang, Y. Q. Qin, *et al.*, Opt. Lett. **25**, 436 (2000).

22. O. A. Egorov and A. P. Sukhorukov, Izv. Akad. Nauk, Ser. Fiz. **62**, 2345 (1998) [Bull. Russ. Acad. Sci., Phys. **62**, 1884 (1998)].

23. P. Vidaković, D. J. Lovering, J. A. Levenson, *et al.*, Opt. Lett. **22**, 277 (1997).

24. L. A. Eyres, P. J. Tourreau, T. J. Pinguet, *et al.*, Appl. Phys. Lett. **79**, 904 (2001).

25. A. V. Buryak, I. Towers, and S. Trillo, Phys. Lett. A **267**, 319 (2000).

Photoluminescence and the Structure of Heterointerfaces of (311)A- and (311)B-Oriented GaAs/AlAs Superlattices

G. A. Lyubas[1], *, N. N. Ledentsov[2], D. Litvinov[3], D. Gerthsen[3], I. P. Soshnikov[2], and V. M. Ustinov[2]

[1] *Institute of Semiconductor Physics, Siberian Division, Russian Academy of Sciences, Novosibirsk, 630090 Russia*
* lubas@isp.nsc.ru
[2] *Ioffe Physicotechnical Institute, Russian Academy of Sciences, St. Petersburg, 194021 Russia*
[3] *University of Karlsruhe, Karlsruhe, Germany*
Received December 11, 2001; in final form, January 3, 2002

GaAs/AlAs superlattices grown simultaneously on GaAs substrates with the (311)A and (311)B orientations have been studied by photoluminescence and high-resolution transmission electron microscopy with a Fourier analysis of images. A periodic interface corrugation is observed for (311)B superlattices. A comparison of the structure of (311)A and (311)B superlattices indicates that the corrugation occurs in both cases and its period along the $[01\bar{1}]$ direction is equal to 3.2 nm. The corrugation is less pronounced in (311)B superlattices, wherein it exhibits an additional modulation (long-wavelength disorder) with the characteristic lateral size exceeding 10 nm. The vertical correlation of regions rich in GaAs and AlAs, which is well observed in (311)A superlattices, is weak in (311)B superlattices due to the occurrence of long-wavelength disorder. The optical properties of (311)B superlattices are similar to those of (100) ones and differ radically from those of (311)A superlattices. As distinct from (311)B, strong photoluminescence polarization anisotropy is observed for (311)A superlattices. It is shown that it is the interface corrugation rather than the crystallographic (311) surface orientation that determines the optical properties of (311)A corrugated superlattices with thin GaAs and AlAs layers. © 2002 MAIK "Nauka/Interperiodica".

PACS numbers: 78.55.Cr; 68.65.Cd

In recent years, studying the corrugation of the gallium arsenide surface in the case of heteroepitaxy on (311)A-oriented substrates has received much attention. This effect was discovered in 1991 [1]. It is based on the self-organization phenomenon, when the faceted (311)A GaAs surface under certain conditions is reconstructed to a periodic array of microfacets (microgrooves) directed along the crystallographic $[\bar{2}33]$ direction with a period of 3.2 nm along the $[01\bar{1}]$ direction [1, 2]. The height of the microgrooves is 1.02 nm in one of the models [1] and 0.34 nm in the other [2]. This is the determining parameter for the possibility of obtaining corrugated superlattices (CSLs), which represent quasi-one-dimensional systems with a strong effect of the size quantization of charge carriers. This last-mentioned fact is important in studying quantum phenomena at room temperature and in developing instruments working on intersubband transitions at high temperatures. The optical properties of (311)A GaAs/AlAs CSLs were studied comprehensively in [1, 3]. However, these studies were restricted to a comparison of (311)A- and (100)-oriented superlattices (SLs) [1, 3]. Recently, the phenomenon of photoluminescence (PL) polarization anisotropy was observed in such structures [3, 4]. It was found that the nature of

polarization anisotropy differs for GaAs layers differing in thickness [4]. When the thickness exceeds ~3.5 nm, the nature of polarization is mainly explained by the orientation anisotropy of the (311) surface, whereas interface corrugation is the predominant factor when the thickness is less than ~ 3.5 nm [4]. The polarization anisotropy of PL observed in [4] is in a good agreement with the data of high-resolution transmission electron microscopy (HRTEM) [1, 3, 5], where it was shown that both the GaAs/AlAs and AlAs/GaAs interfaces are corrugated in samples grown on the (311)A surface with a lateral period of 3.2 nm and a height of 1 nm. The optical properties of type II GaAs/AlAs SLs grown on the (311) surface are determined by the surface polarity. The interface structure and photoluminescence properties of SLs grown on the (311)B GaAs surface have not been studied so far. This work is devoted to studying the structure of heterointerfaces in (311)B SLs in comparison with the structure of (311)A samples. The differences in the PL properties of SLs grown on (311)A- and (311)B-oriented surfaces are analyzed.

The GaAs/AlAs SLs under study were grown by molecular-beam epitaxy on GaAs substrates with the (311)A, (311)B, and (100) orientations. The A and B directions were determined by the anisotropy of chemical etching. The period in the SLs under study was

4 nm, and the mean thickness of the GaAs and AlAs layers was similar and equaled 2 nm. The samples were examined by PL spectroscopy in the temperature range from 77 to 300 K. The PL excitation source was an Ar laser (488 nm) with a typical pump power of 10–20 mW (the power density was 5–10 W/cm^2). The PL spectra were recorded using a SDL-1 double monochromator with a resolution of 0.4 nm and a photomultiplier with an S-20 cathode. A Glan biprism was used as the polarization analyzer of the light emitted by the samples. A depolarizing wedge was arranged at the monochromator entrance slit. The SL structure was studied by high-resolution transmission electron microscopy with an appropriate image evaluation technique to enhance the contrast due to the difference in the electron extinction coefficient for AlAs and GaAs. A Philips Model CM200 FEG/ST microscope was used.

An HRTEM image of the structure of (311)B superlattice heterointerfaces is given in Fig. 1. The [311] direction is oriented upward, and the [01$\bar{1}$] direction is oriented to the right. The dark and light layers correspond to GaAs and AlAs, respectively. The image displays an indistinct corrugation with a lateral period of 3.2 nm. The lateral period of 3.2 nm is strongly blurred by long-wavelength (with a characteristic lateral size of more than 10 nm) disorder. The presence of the long-wavelength disorder leads to a weak vertical correlation of regions rich in GaAs and AlAs. As distinct from the (311)A SLs, where the elevated regions are located above the elevated ones and depressions are arranged above depressions, a correlation of this kind is virtually lacking in (311)B SLs. With the aim of performing a more in-depth analysis of the differences in the arrangement of heterointerfaces in the (311)A and

(311)B SLs, we obtained the Fourier transforms of processed HRTEM images. These are shown in Figs. 2a and 2b for (311)A and (311)B SLs. In order to distinguish the lateral periodicity more clearly, the long-wavelength component was subtracted in images in Figs. 2a and 2b. The Fourier transforms of images for the same (311)A and (311)B SLs but without subtracting are given in Figs. 2c and 2d. It is evident that both the (311)A and (311)B SLs exhibit a lateral period of 3.2 nm. This period is manifested in (311)B SLs much weaker and is strongly blurred by the long-wavelength component; however, there is still an intensity maximum. The occurrence of the lateral period for the (311)B SL correlates with the recent studies carried out by scanning tunneling microscopy [6], where periodic faceting (cleavage) of the (311)B GaAs surface was observed with a similar period. We emphasize that it is the periodic faceting of the (311)B GaAs surface that was observed in [6], whereas we observed a periodic corrugation of heterointerfaces. Finding a periodic cleavage of the surface might not signify that the alternating GaAs and AlAs layers grown on it will also be height-modulated. Note that the lateral periodicity with a period of 3.2 nm found for the (311)B SL is not as distinct as that in the (311)A SL, so it can be observed sufficiently well only after excluding the long-wavelength component. A very distinct corrugation with a height of 1 nm and a period of 3.2 nm was found in the (311)A SL in full correspondence with the model [1].

The essential differences in the arrangement of heterointerfaces in the (311)A- and (311)B-oriented SLs found here lead to a strong difference in their photoluminescence properties. Consider the PL spectra of GaAs(2 nm)/AlAs(2 nm) SLs grown on the (311)A, (311)B, and (100) surfaces in the same growth cycle
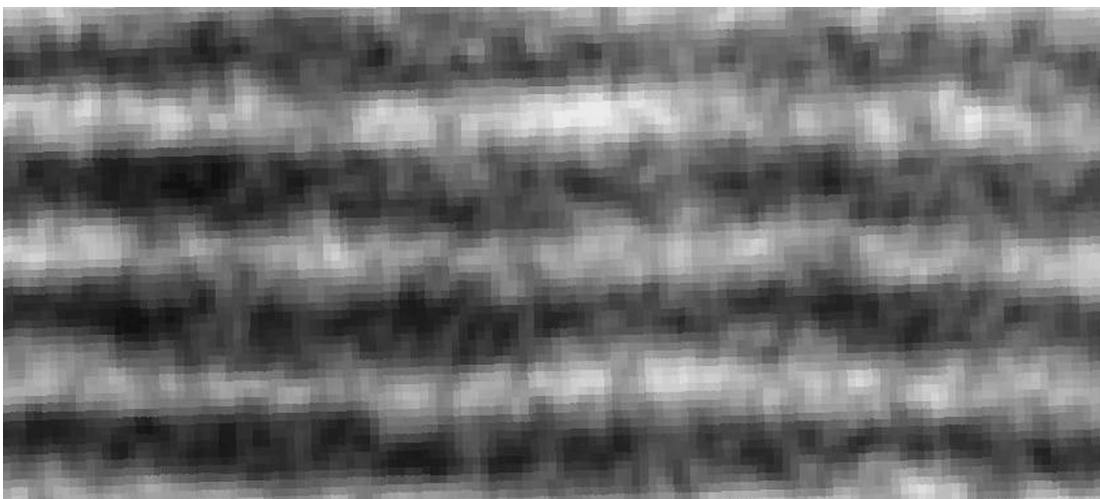

Fig. 1. Electron microscopy image of the structure of heterointerfaces in (311)B SLs. The [311] and [01$\bar{1}$] directions are oriented upward and rightward, respectively. Dark and light layers correspond to GaAs and AlAs, respectively. Indistinct corrugation with a lateral period of 3.2 nm and long-wavelength disorder with a characteristic lateral size of more than 10 nm can be seen in the figure.
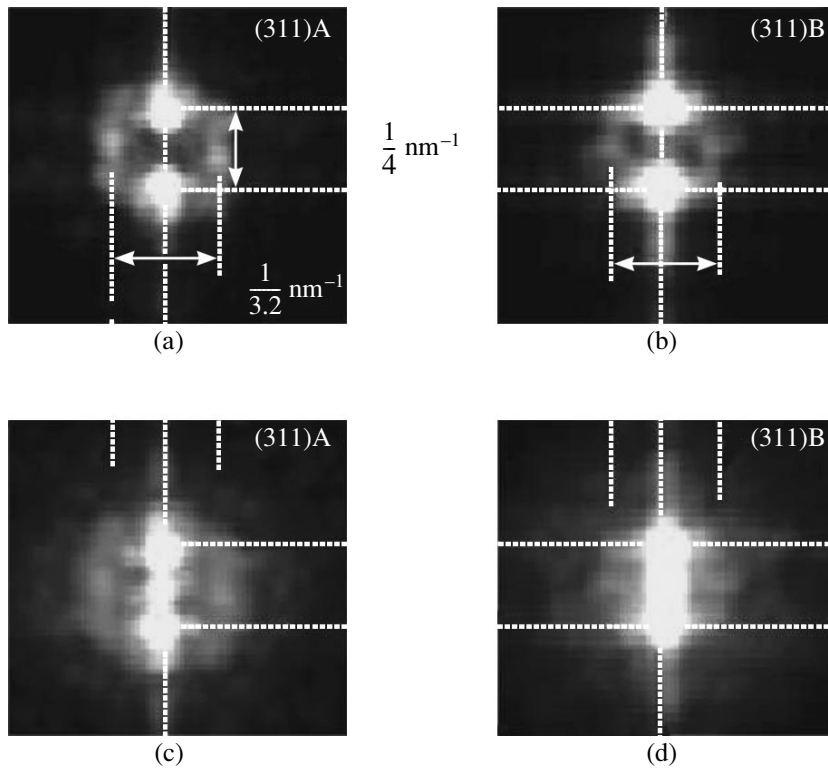
Fig. 2. Fourier transforms of HRTEM images obtained for (a) (311)A and (b) (311)B SLs with subtracting the long-wavelength component. Fourier transforms of the same SLs but without subtracting are shown in (c) and (d). A lateral period of 3.2 nm can be seen in all cases. It is manifested much weaker in the (311)B SL and is strongly blurred by the long-wavelength component; however, an intensity maximum is still evident.

and, hence, under the same conditions (see Fig. 3). The spectra are given for different temperatures. A comparison of the spectra of the (311)B and (100) SLs shows that these spectra are very similar in appearance and radically differ from the spectra of the (311)A SL. As distinct from the (311)A SL, the spectra of the (311)B and (100) SLs exhibit one maximum each, whose intensity grows with decreasing temperature. The similarity of the photoluminescence of the (311)B and (100) SLs means that corrugation produces no significant modification of electronic optical properties for the (311)B SL in contrast to the (311)A SL. A weaker corrugation and the occurrence of disorder in the (311)B SL do not allow this to happen. On the other hand, the additional size quantization of charge carriers due to distinct corrugation in the (311)A CSL leads to a significant modification of its electronic optical and quantum properties. As a result, the Γ and X conduction band minima mix together[1]; consequently the PL spectrum of the (311)A CSL exhibits two minima from both the transitions involving the X conduction band minimum and the transitions from the mixed Γ and X states. Note that this giant mixing is due to the distinct corrugation of heterointerfaces with a period of 3.2 nm and a height of

1 nm in the (311)A CSL under study. Thus, a very clear connection can be traced between the corrugation character and the optical properties of the CSL.
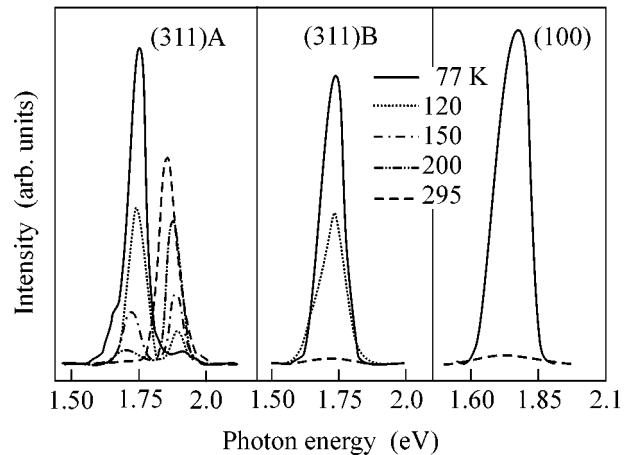

Fig. 3. Photoluminescence spectra recorded at different temperatures for GaAs(2 nm)/AlAs(2 nm) SLs grown on the (311)A, (311)B, and (100) surfaces simultaneously in one growth cycle. The polarization of light was not analyzed. The spectra of the (311)B and (100) superlattices contain one maximum each and are very similar to one another, whereas two maxima are observed in the spectra of the (311)A superlattice, which radically distinguish these spectra from the spectra of (311)B and (100) superlattices.

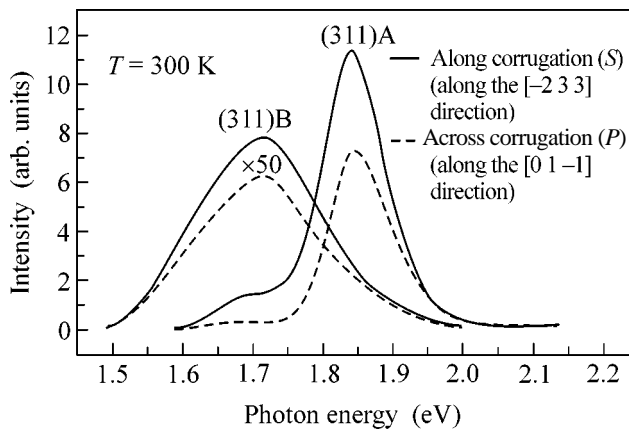[1] The essence of the mixing phenomenon was described in [3].

Fig. 4. Photoluminescence spectra recorded at room temperature for GaAs(2 nm)/AlAs(2 nm) SLs grown on the (311)A- and (311)B-oriented surfaces in one growth cycle. The light excited photoluminescence was polarized at an angle of 45° to the direction of the corrugation grooves, and the polarization of the light emitted by samples was analyzed along (line, *S* component) and across (dashed line, *P* component) the grooves. The intensity of spectra for the (311)B superlattice was magnified 50-fold.
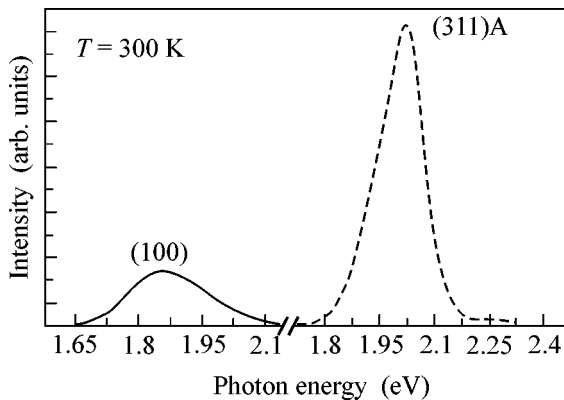

Fig. 5. Photoluminescence spectra recorded at room temperature for GaAs/AlAs SLs grown in one growth cycle on GaAs substrates with the (311)A (maximum at 2.02 eV) and (100) (maximum at 1.87 eV) orientations. The amount of deposited GaAs corresponded to a layer 1 nm thick for the (100) surface. Under these conditions, flat layers are formed on the (100) surface, whereas an array of quantum wires is formed on the (311)A surface. The maximum of photoluminescence from the superlattice containing quantum wires lies at significantly higher energy values. The increase in energy is explained by the occurrence of additional size quantization of charge carriers in quantum wires.

Figure 4 demonstrates the PL spectra of (311)A- and (311)B-oriented SLs measured at room temperature for various polarization geometries. The PL-exciting light was polarized at an angle of 45° to the direction of corrugation grooves, and the polarization of the sample-emitted light was analyzed in two geometries: along (line, *S* component) and across (dashed line, *P* component) the grooves. The (311)A and (311)B SLs were grown simultaneously in one growth cycle. It is evident that the GaAs/AlAs SL grown on the (311)A surface exhibits efficient PL at room temperature. A red glow from this SL was visible to the naked eye, and the PL intensity was more than 50 times higher than in the case of the (311)B SL (the spectra of the latter are shown in 50-fold magnification in Fig. 4). The difference is explained by the formation of well-structured corrugated layers of gallium arsenide in the (311)A SL, whose occurrence in the given sample was confirmed by direct electron microscopy investigations. The lateral localization of electrons in CSLs (preferentially, the motion of electrons in CSLs is allowed only along the corrugation grooves) decreases radiationless recombination at the surface. That was the reason for the high PL intensity at room temperature. As expected, strong polarization anisotropy was observed in the PL spectra of the (311)A CSL. The degree of polarization $(S - P)/(S + P)$ for the peak with an energy of 1.69 eV was more than 60%, and that for the peak with an energy of 1.84 eV was more than 22% (see Fig. 4). It is evident in the same figure that the PL anisotropy was considerably smaller in the case of the (311)B SL (maximum at 1.71 eV), and its degree was about 10%. The decrease in the polarization anisotropy for the (311)B SL is readily explicable and is associated with the fact that the corrugation in this SL (see Fig. 1) is not as distinct as in the (311)A SL. No variation of the polarization anisotropy was found under variations of temperature. Thus, the corrugation effect was small in the case of the (311)B SL, and the nature of polarization is mainly explained by the valence band anisotropy.

The following data are also in a good agreement with the corrugation model proposed in [1, 5]. Figure 5 displays PL spectra measured at room temperature for GaAs/AlAs SLs grown simultaneously on GaAs substrates with the (311)A and (100) orientations. In this case, the amount of GaAs deposited in one growth cycle corresponded to a layer 1 nm thick for the (100) surface. Under these conditions, flat layers are formed on the (100) surface, and quantum wires (QW) or, more exactly, wirelike clusters are formed on the (311)A surface [7]. The mean thickness of AlAs layers was larger than the corrugation height (1 nm in the model [5]); that is, it was sufficient for new AlAs facets to be formed. The maximum of PL from the SL containing flat GaAs layers lies at 1.87 eV. In the case of the SL containing QWs, the maximum is located at 2.02 eV. Hence, the maximum of PL from the SL containing QWs is displaced by 150 meV toward larger energy values as compared to the SL containing flat layers. Such a significant increase in energy is explained by the change in the dimensionality of the system in going from two-dimensional flat layers to one-dimensional QWs. The line half-width in the spectrum of PL from the (311)A SL is smaller than that for the (100) SL. The decrease in dimensionality results in a decrease in the width of subbands, which leads to narrower optical spectra. In the case of the (311)A SL, the line can be additionally

broadened because the wirelike clusters can differ in length (because the motion of carriers is confined in the direction parallel to the QW). Note that the PL intensity for the (311)A SL is approximately five times higher than that for the (100) SL. Scattering by optical phonons is strongly suppressed in one-dimensional systems. This results in a decrease in radiationless recombination and, as a consequence, in an increase in radiative recombination, which is the reason for the increase in intensity observed in QWs in our case. A certain additional increase in intensity can arise from the increase in the density of states in the case of (311)-oriented systems.

Thus, direct high-resolution electron microscopy investigations of (311)A and (311)B SLs revealed the occurrence of corrugation in both cases with a lateral period of 3.2 nm. In the case of (311)B SLs, the interface corrugation has been observed for the first time. In addition, a very distinct corrugation 1 nm in height is observed for (311)A SLs in full correspondence with the model [1]. On the other hand, corrugation in the (311)B SLs grown simultaneously with (311)A SLs is significantly less pronounced and is characterized by considerable long-wavelength disorder. The occurrence of long-wavelength disorder in (311)B SLs weakens the vertical correlation of GaAs- and AlAs-rich regions, which is clearly observed in the case of (311)A SLs. The character of interface corrugation found for (311)B SLs is such that the optical properties of these SLs cannot become similar to those of (311)A SLs, whose corrugation fully fits the model [1]. As distinct from (311)B SLs, strong photoluminescence polarization anisotropy is observed for (311)A SLs, when the light polarized in the direction along the heterointerface corrugation grooves is significantly higher in intensity than that polarized across the grooves. Polarization anisotropy in the PL spectra of (311)B SLs is significantly weaker. Thus, these results confirm the conclusion made in [4] that the nature of polarization for (311)A CSLs with thin GaAs and AlAs layers is mainly determined by the interface corrugation. It is found that (311)B SLs are similar in their optical properties to conventional (100) SLs and radically differ from (311)A CSLs. It is stated that the electronic optical properties of (311)B CSLs, as distinct from (311)A CSLs, are not markedly modified by corrugation. It is shown that it is the interface corrugation rather than the difference in crystallographic orientation between the (311) and (100) surfaces that determines the optical properties of (311)A CSLs with thin GaAs and AlAs layers.

REFERENCES

1. R. Nötzel, N. N. Ledentsov, L. A. Däweritz, *et al.*, Phys. Rev. Lett. **67**, 3812 (1991).

2. M. Wassermeier, J. Sudijono, M. D. Johnson, *et al.*, Phys. Rev. B **51**, 14721 (1995).

3. R. Nötzel, N. N. Ledentsov, L. A. Däweritz, *et al.*, Phys. Rev. B **45**, 3507 (1992).

4. G. A. Lyubas and V. V. Bolotov, Pis'ma Zh. Éksp. Teor. Fiz. **72**, 294 (2000) [JETP Lett. **72**, 205 (2000)].

5. N. N. Ledentsov, D. Litvinov, A. Rosenauer, *et al.*, J. Electron. Mater. **30**, 463 (2001).

6. Z. M. Wang, L. Däweritz, and K. H. Ploog, Appl. Phys. Lett. **78**, 712 (2001).

7. Zh. I. Alferov, A. Yu. Egorov, A. E. Zhukov, *et al.*, Fiz. Tekh. Poluprovodn. (St. Petersburg) **26**, 1715 (1992) [Sov. Phys. Semicond. **26**, 959 (1992)].

Translated by A. Bagatur'yants

Ab initio Calculations of the Equation of State and Elastic Constants of Aluminum in the Region of Negative Pressures

G. V. Sin'ko* and N. A. Smirnov

*Russian Federal Nuclear Center, Zababakhin All-Russia Research Institute of Technical Physics,
Snezhinsk, 456770 Russia*
* e-mail: g.v.sinko@vniitf.ru

The results of *ab initio* calculations are presented for the specific energy, pressure, and elastic constants of an aluminum fcc single crystal with subnormal densities at $T = 0$. Kinks in the elastic constant vs. density curves are revealed which are caused by the electronic topological transitions. An analysis of the mechanical stability of aluminum fcc crystal at negative pressures suggests that the polymorphic transition to a noncubic structure is possible. A method is suggested for taking into account the thermal nuclear excitation and the influence of zero-point vibrations on the pressure dependence of crystal density. © *2002 MAIK "Nauka/Interperiodica"*.

PACS numbers: 64.30.+t; 61.50.Ks; 62.20.Dc; 71.15.Mb

In recent experiments [1–3] with a pulsed nanosecond shock load in metals, one succeeded in producing exceedingly high tensions with negative pressures (tensile stresses) attaining 150 kbar and more. This opens up possibilities of studying polymorphic phase transformations and other solid-state phenomena in the new exotic field of state parameters. In studies of this kind, the question inevitably arises of the equation of state for the tensions as high as those mentioned above. The known theoretical and semiempirical model equations of state are aimed at describing the compression states for which the results of many measurements are known, while the tension states are calculated by extrapolating these data [1–3] to the negative pressures. However, inasmuch as the isotherms and isentropes of condensed media have minima, there is still room for doubt about the accuracy and range of applicability of this extrapolation. It is likely that an *ab initio* calculation is now the only way of making an unbiased estimate of the equation of state for a substance at high negative pressures.

In this work, we report and analyze the results of *ab initio* calculations of the specific energy, pressure, and elastic properties of aluminum single crystals with the fcc structure at $T = 0$ in the region of subnormal densities. The calculations of specific energy were carried out for fixed nuclei by the full-potential linear muffin-tin orbitals (FP-LMTO) method [4] within the framework of the density functional theory with generalized gradient corrections [5–7]. The accuracy of the calculated specific energy was 0.1 mRy/atom over the entire range of specific volumes studied.

The *ab initio* specific energies were approximated by the Rose *et al.* [8] formula that was slightly modified by supplementing it with two additional parameters:

$$E_{0e}(v) = E_\infty - \Delta E(1 + y + \alpha y^2 + \beta y^3)\exp(-y), \quad (1)$$

where

$$y = \frac{1 - x}{x}\frac{r_0}{l}, \quad x = \left(\frac{v_0}{v}\right)^{1/3}, \quad r_0 = \left(\frac{3v_0}{4\pi}\right)^{1/3}, \quad (2)$$

v is the specific volume, and v_0 is the specific volume at $P = 0$ and $T = 0$. Formula (1) is not as universal as the formula given in [8], but our experience suggests that Eq. (1) allows a higher accuracy to be obtained when approximating the *ab initio* results for the specific energy of various metal crystal structures over a wide range of densities, for which only the outer electron shells are involved in interatomic interactions. The quantities v_0, l, ΔE, E_∞, α, and β in Eq. (1) were considered as fitting parameters. The following expression for the pressure follows from Eq. (1):

$$P_{0e}(v) = 3B_0 x(x - 1)$$
$$\times \left(1 + \frac{(\alpha - 3\beta)y + \beta y^2}{1 - 2\alpha}\right)\exp(-y), \quad (3)$$

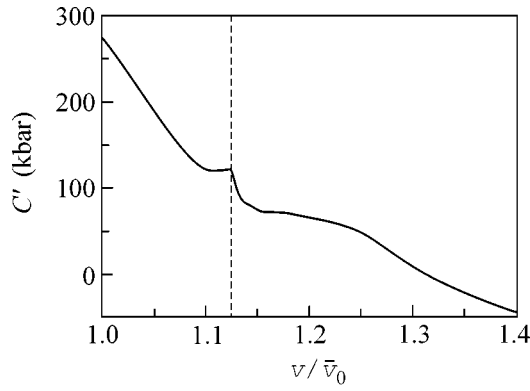where

$$B_0 = \frac{\Delta E(1 - 2\alpha)}{12\pi r_0 l^2}.$$

Fig. 1. Dependence of $C' = (C_{11} - C_{12})/2$ on the specific volume at $T = 0$. $\tilde{v}_0 = 0.3705$ cm^3/g is the experimental value of specific volume at $T = 300$ K and $P = 1$ atm.

Fig. 2. Dependence of C_{44} and pressure on the specific volume at $T = 0$. The dashed line corresponds to the pressure without zero-point vibrations. $\tilde{v}_0 = 0.3705$ cm^3/g is the experimental value of specific volume at $T = 300$ K and $P = 1$ atm.

The fitting procedure yielded the following results for the fcc aluminum:

$$v_0 = 0.3664047 \text{ cm}^3/\text{g}, \quad l = 0.1459307 \text{ cm/g}^{1/3},$$

$$\Delta E = E_\infty = 44.874894 \text{ kJ/g}, \qquad (4)$$

$$\alpha = 0.1945598, \quad \beta = 0.2324356.$$

The maximum error in approximating the calculated values of specific energy by Eq. (1) with parameters (4) is within the error of our calculations and does not exceed 1 J/g ≈ 0.02 mRy/atom. The pressure curve given by Eq. (3) reaches its minimum $P_{\min} = -116.749$ kbar at $v_{\min} = 0.5508$ cm^3/g.

The elastic constants of the strained lattice were determined after calculating its specific energy as a function of the degree of deformation for several deformation types. The elastic constants $C' = (C_{11} - C_{12})/2$ and C_{44} and the pressure are displayed in Figs. 1 and 2 as functions of specific volume. The appearance of negative elastic constants in the negative pressure region is noteworthy. This occurs because a term proportional to the pressure with a minus sign makes a contribution to the strain-induced energy increment. The presence of well-defined kinks in the curves at $v/\tilde{v}_0 \approx 1.125$ is another intriguing feature in the behavior of aluminum elastic constants at high tensile strains. These kinks are due to the electronic topological transition [9] occurring at this value of $v/\tilde{v}_0$. It will be shown below that they are responsible for the kink in the volume dependence of the Debye temperature and, as a result, for a discontinuity in the pressure curve allowing for the zero-point vibrations. Moreover, if the zero-point vibrations are not taken into account, one of the conditions for mechanical stability of cubic structures [10], namely,
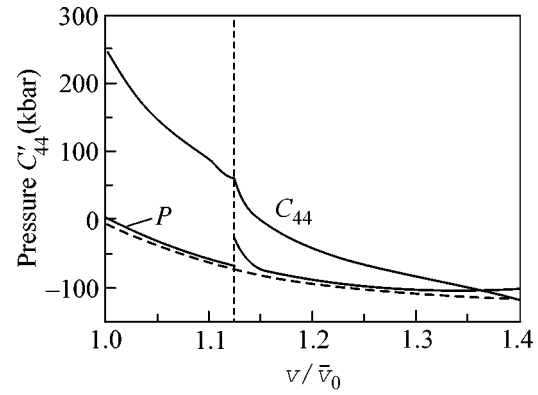
$$C_{44} > P, \qquad (5)$$

is violated before the structure becomes absolutely unstable upon crystal dilation. According to the calculations, this corresponds to the polymorphic phase transition of aluminum to the noncubic structure at negative pressures. Such a behavior of elastic constants may be responsible for the destruction of an ideal crystal subjected to tensile stresses at specific volumes smaller than it would occur in the absence of the anomaly or may stimulate the onset of melting.

The elastic constants determined for different specific volumes were used to calculate the mean sound velocity $\bar{c}(v)$ and Debye temperature $\Theta(v)$ as functions of specific volume with the aim of estimating the influence of zero-point vibrations on the pressure curve. The mean sound velocity was determined by averaging the actual sound velocity $c_s(\mathbf{n})$ over the directions of unit vectors $\mathbf{n}$ and branches $s = 1, 2, 3$ according to the formula [11]

$$\frac{1}{\bar{c}^3} = \frac{1}{3} \sum_s \int \frac{d\Omega}{4\pi} \frac{1}{c_s^3(\mathbf{n})}. \qquad (6)$$

According to [12], the true sound velocity can be found from the solution to the problem for eigenvalues of the matrix $L_{ik}(\mathbf{n})$, which is completely specified by the tensor components C_{ijkl} of elastic constants and by the pressure:

$$L_{ik}(\mathbf{n}) = \sum_{jl} C_{ijkl} n_j n_l - P \delta_{ik}. \qquad (7)$$

The corresponding equations have the form

$$\text{Det}[L_{ik}(\mathbf{n}) - \rho c^2(\mathbf{n}) \delta_{ik}] = 0, \qquad (8)$$
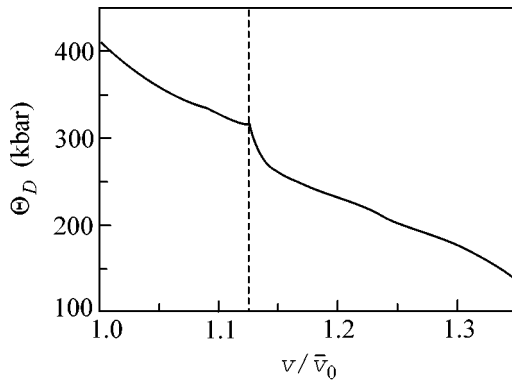
Fig. 3. Debye temperature as a function of specific volume. $\tilde{v}_0 = 0.3705$ cm^3/g is the experimental specific volume at $T = 300$ K and $P = 1$ atm.

where ρ is the crystal density. The Debye temperature is related to the mean sound velocity as

$$\Theta(v) = \frac{1}{k_B}\left(\frac{6\pi^2 N_A}{vA}\right)^{1/3}\hbar\bar{c}(v),$$

where k_B is the Boltzmann constant, N_A is Avogadro's number, and A is the atomic weight. The Debye temperatures calculated in this way are presented in Fig. 3. The volume dependence of the Debye temperature can be used for estimating the contribution of zero-point vibrations to the energy and pressure at $T = 0$ and for the calculation of the contribution to the thermodynamic functions from the nuclear thermal excitations. Unfortunately, the contribution of zero-point vibrations to the elastic constants cannot be estimated in such a simple way. One can see from Fig. 2 that the above-mentioned approximate inclusion of zero-point vibrations increases the minimum pressure and shifts the minimum to smaller specific volumes. Nevertheless, considering the model character of taking zero-point vibrations into account, the computational results may be thought of as indicating the possible polymorphic transition of the aluminum fcc crystal to the noncubic structure at negative pressures. Of course, such a transition

is possible if the aluminum crystal has not already been destroyed or does not melt because of the anomalies in elastic properties caused by the electronic topological transition. It would be of interest to explore this situation experimentally.

REFERENCES

1. G. I. Kanel, S. V. Razorenov, A. V. Utkin, *et al.*, J. Appl. Phys. **74**, 7162 (1993).

2. E. Moshe, S. Eliezer, Z. Henis, *et al.*, Appl. Phys. Lett. **76**, 1555 (2000).

3. G. I. Kanel, S. V. Razorenov, K. Baumung, and J. Singer, J. Appl. Phys. **90**, 136 (2001).

4. S. Yu. Savrasov and D. Yu. Savrasov, Phys. Rev. B **46**, 12181 (1992).

5. J. P. Perdew and Y. Wang, Phys. Rev. B **45**, 13244 (1992).

6. J. P. Perdew, J. A. Chevary, S. H. Vosko, *et al.*, Phys. Rev. B **46**, 6671 (1992).

7. U. von Barth and L. Hedin, J. Phys. C **5**, 1629 (1972).

8. J. H. Rose, J. R. Smith, F. Guinea, and J. Ferrante, Phys. Rev. B **29**, 2963 (1984).

9. V. G. Vaks and A. V. Trefilov, J. Phys.: Condens. Matter **3**, 1389 (1991).

10. J. Wang, J. Li, S. Yip, *et al.*, Phys. Rev. B **52**, 12627 (1995).

11. N. W. Ashcroft and N. D. Mermin, *Solid State Physics* (Holt, Rinehart and Winston, New York, 1976; Mir, Moscow, 1979).

12. D. C. Wallace, Solid State Phys. **25**, 301 (1970).

Translated by V. Sakun

Random Textures of the Order Parameter of Superfluid ^{3}He-B in Aerogel

I. A. Fomin

Kapitsa Institute for Physical Problems, Russian Academy of Sciences, ul. Kosygina 2, Moscow, 117334 Russia
e-mail: fomin@kapitza.ras.ru

Received January 15, 2002

A phenomenological scheme of the observed properties of superfluid ^{3}He in aerogel is proposed in the spirit of the Ginzburg-Landau theory. The effect of the aerogel on the order parameter is described by the random tensor field $\eta_{jl}(\mathbf{r})$. The tensor field exerts a considerable disorienting effect on the order parameter in the A phase of ^{3}He, but virtually unaffects the orientation of the order parameter in the B phase in zero magnetic field. The change in the texture of the order parameter emerging in the B phase in aerogel in a magnetic field is considered. It is shown that the mean square of the angle between the magnetic field direction and the anisotropy axis of the B phase is proportional to the third power of the magnetic field strength. The fluctuations of the direction of the magnetic anisotropy axis of ^{3}He-B are correlated over the familiar "healing length", which is inversely proportional to the field strength and has a macroscopic scale. © *2002 MAIK "Nauka/Interperiodica".*

PACS numbers: 67.57.-z

1. Aerogels are materials with extremely high porosity. The rigid "skeleton" formed by fibers with a diameter of ≈ 30 Å occupies less than 2% of the volume. The remaining volume can be filled with a substance under investigation. At the present time, this is the only way of introducing impurities in liquid ^{3}He in the temperature range where it becomes superfluid [1]. Aerogel does not suppress superfluidity completely; it only decreases the superconducting transition temperature T_c, which is in accordance with the concept of suppression of abnormal superconductivity and superfluidity by nonmagnetic impurities [2] on account of the fact that the estimated mean free path of quasiparticles $l \sim 1500$–1800 Å is large compared to $\xi_0 \approx 160$ Å (under the solidification pressure). The microscopic theory in the spirit of superconducting alloys [3], which takes into account the effect of impurities through an additional parameter, i.e., the transport mean free path, provides qualitatively correct description for the observed decrease in T_c and the tendency in the variation of properties of superfluid phases of ^{3}He, but does not offer a quantitative agreement with the experimental data (see the review and references in [4]). In order to obtain a more detailed description of the observed properties of superfluid ^{3}He in aerogel, a phenomenological approach should be used; i.e., the effect of the aerogel should be described by a certain set of parameters which are assumed to be preset. The number and choice of parameters are determined by the symmetry of the problem. Although this approach was discussed in [4], it has not been developed sufficiently for obtaining specific results. In particular, the important aspect concerning the correct choice of parameters characterizing the aerogel remains unclear. In the present work, a method for the phenomenological description of superfluid ^{3}He in aerogel is proposed and a practically important example of application of this approach is considered.

2. A macroscopic description is possible only for long-wave phenomena for which the characteristic spatial scale exceeds the correlation length ξ_0 in superfluid ^{3}He. In the vicinity of T_c, the additional contribution to energy density can be presented in the form

$$f_\eta = g_\eta A_{\mu j} A^*_{\mu l} \eta_{jl}(\mathbf{r}), \qquad (1)$$

where the complex 3×3 matrix $A_{\mu j}$ is the order parameter of superfluid ^{3}He, its first and second indices labeling the spin and momentum components, respectively. The random rank-two tensor $\eta_{jl}(\mathbf{r})$ is determined by the properties of the aerogel. The aerogel fibers consist of nonmagnetic SiO^2, and the interaction of helium with it is due to scattering of quasiparticles at the fibers; for this reason, tensor $\eta_{jl}(\mathbf{r})$ in formula (1) is convoluted with the momentum indices. It is also clear that $\eta_{jl}(\mathbf{r})$ can be regarded as real-valued and symmetric. We will assume that the isotropic component of the tensor $\eta_0(\mathbf{r})\delta_{jl}$ is included in the superconducting transition temperature T_c, which thus becomes a position function, the trace η_{jj} being equal to zero. It is natural to assume that the aerogel is, on average, isotropic; i.e., $\langle \eta_{jl}(\mathbf{r}) \rangle = 0$. Here and below, the angle brackets indicate averaging over the ensemble of aerogels. It is convenient to assume that the common factor g_η is equal to

the product of the density of states $N(0)$ and the volume concentration of the aerogel; in this case, tensor η_{jl} is dimensionless and its elements are on the order of unity. Under the assumptions made above, nontrivial information on the properties of an aerogel is contained in the correlation function

$$K_{jlmn}(\mathbf{r}, \mathbf{r'}) = \langle \eta_{jl}(\mathbf{r}) \eta_{mn}(\mathbf{r'}) \rangle. \qquad (2)$$

At a large distance from the wall, the aerogel is homogeneous and, hence, the correlator is determined by the difference $\mathbf{r} - \mathbf{r'}$. We will be interested in the Fourier transform of the correlator for this difference: $K_{jlmn}(\mathbf{k})$. Definition (2) leads to the symmetry properties $K_{jlmn}(\mathbf{k}) = K_{ljmn}(\mathbf{k}) = K_{jlnm}(\mathbf{k}) = K_{mnjl}(-\mathbf{k})$ as well as $K_{jjmn}(\mathbf{k}) = K_{jlmm}(\mathbf{k}) = 0$. Taking these properties into account, we can write the correlator in the form of a combination of independent tensors composed from the unit tensor δ_{jl} and the unit vector components $\hat{k}_j$:

$$\begin{aligned} K_{jlmn}(\mathbf{k}) = {}& 3\Phi_0(k)[\hat{k}_j\hat{k}_m(\delta_{ln} - \hat{k}_l\hat{k}_n) \\ &+ \hat{k}_l\hat{k}_m(\delta_{jn} - \hat{k}_j\hat{k}_n) + \hat{k}_j\hat{k}_n(\delta_{lm} - \hat{k}_l\hat{k}_m) \\ &+ \hat{k}_l\hat{k}_n(\delta_{jm} - \hat{k}_j\hat{k}_m)] + 3\Phi_1(k)[6\hat{k}_j\hat{k}_l\hat{k}_m\hat{k}_n \qquad (3) \\ &- 2(\hat{k}_j\hat{k}_l\delta_{mn} + \hat{k}_m\hat{k}_n\delta_{jl}) + \delta_{jm}\delta_{ln} + \delta_{jn}\delta_{lm}] \\ &+ \Phi_2(k)(3\hat{k}_j\hat{k}_l - \delta_{jl})(3\hat{k}_m\hat{k}_n - \delta_{mn}), \end{aligned}$$

where $\Phi_0(k)$, $\Phi_1(k)$, and $\Phi_2(k)$ are real functions of the absolute value of $\mathbf{k}$. In the description of long-wave phenomena, only the values of these functions for $\mathbf{k} = 0$ are significant. It is these three numbers that determine the orienting effect of the aerogel on the order parameter of superfluid ^{3}He. Interaction (1) is weak as compared to the terms in the free energy of superfluid ^{3}He, which determine the form of the order parameter in view of the smallness of the aerogel concentration. Thus, it is natural to assume that the same superfluid phases A and B are realized in aerogel as in pure ^{3}He. Substitution of the order parameter of the A phase into formula (1) gives $f_\eta \sim -\eta_{mn}l_ml_n$, where $\mathbf{l}$ is the direction of the orbital quantization axis in the A phase. It was proved in [5] that the random effect of aerogel on the orientation of vector $\mathbf{l}$ must lead to the disappearance of the long-range orientation order in this phase. A different situation is observed in the B phase, where the order parameter has the form

$$A_{\mu j} = \Delta e^{i\varphi} R_{\mu j}, \qquad (4)$$

where $R_{\mu j}$ is an orthogonal matrix such that $R_{\mu j}R_{\mu l} = \delta_{jl}$. By virtue of this relation, the substitution of the order parameter (4) into formula (1) gives zero. A nonzero contribution to energy can be obtained by taking into account either the surface dipole interaction or the presence of a magnetic field. The dipole interaction gives a negligibly small effect; for this reason, we will consider below only the interaction induced by the magnetic field.

3. In a magnetic field, the order parameter (4), tensor η_{mn}, and the magnetic field components H_μ can be used to compose the following nonzero scalar combination:

$$f_\eta = \frac{1}{2}\chi g_a H_\mu H_\nu R_{\mu j} R_{\nu l} \eta_{jl}(\mathbf{r}), \qquad (5)$$

where χ is the magnetic susceptibility of the normal phase of ^{3}He, and g_a is a temperature-dependent coefficient. This is the main term in the expansion of the additional energy in $\mu H/\Delta$, where μ is the magnetic moment of the nucleus of ^{3}He. The correction f_η preserves its form away from the temperature T_c as well. Matrix R in definition (4) is usually regarded as the matrix of rotation defined by the direction n of the rotation axis and the rotational angle θ. The volume dipole energy defines $\theta = \arccos(-1/4)$. Estimates similar to those obtained in [5] show that perturbation (5) cannot lead to a noticeable deviation of angle θ from the equilibrium value. Direction n in the bulk is fixed by a much weaker interaction including both the magnetic field and the dipole energy $f_H = -\chi a_H(\mathbf{nH})$, and the situation is not so clear in this case. Let us consider in greater detail the effect of the random field $\eta_{jl}(\mathbf{r})$ on the spatial distribution, or texture, of vector $\mathbf{n}$. It should be noted that the texture will also be random. In order to find the texture, we must minimize the total free energy, including the sum of the energy densities f_η and f_H, as well as the gradient energy f_∇:

$$F = \int d^3r\{f_\eta + f_H + f_\nabla\}. \qquad (6)$$

In the course of minimization, it is convenient to choose the Euler angles α, β, γ as parameters determining the matrix $R_{\mu j}$, assuming that the z axis is parallel to $\mathbf{H}$. We will assume that random deviations of the texture from equilibrium are small for fields of several hundred oersted that are normally used (this is confirmed by the results). We will also consider ^{3}He away from the walls and then $\mathbf{n} \parallel \mathbf{H}$ in the absence of aerogel; i.e., $\beta = 0$, and α and γ satisfy the relation $1 + 2\cos(\alpha + \gamma) = 0$ following from the condition $\cos\theta = -1/4$. For small deviations from equilibrium, we have $\beta \ll 1$ and the energy densities appearing in formula (6) can be written in the form $f_\eta = (1/2)\chi H^2 g_a h_j h_l \eta_{jl}$, where h is the direction transformed into the direction of the z axis under the action of rotation $R_{\mu j}$: $\mathbf{h} = (-\beta\cos\gamma, \beta\sin\gamma, 1 - \beta^2/2)$. The second term $f_H \approx (2/5)\chi a_H H^2\beta^2$. In order to simplify the expression for gradient energy, we will assume that the velocities of spin waves $c_\parallel$ and $c_\perp$, appearing in it as coefficients, are identical. This leads to an insignificant inaccuracy, but makes the obtained relations much less cumbersome. Taking into account this simplification, we obtain

$$f_\nabla = (\chi/2\gamma^2)c_\parallel^2[\beta^2(\nabla\gamma)^2 + (\nabla\beta)^2]. \qquad (7)$$

It is natural to pass to new variables: $u = \beta \cos\gamma$ and $v = \beta \sin\gamma$. As a result, the free energy will be written in the form

$$F = \chi H^2 \int d^3r \left\{ \frac{c_\parallel^2}{2\omega_L^2} [(\nabla u)^2 + (\nabla v)^2] \right.$$

$$\left. + \frac{2}{5} a_H (u^2 + v^2) + \frac{1}{2} g_a h_j h_l \eta_{jl} \right\} d^3r. \tag{8}$$

We now have $\mathbf{h} = (-u, v, 1 - (u^2 - v^2)/2)$. By varying energy (8) in u and v, we obtain, respectively, the equation for u,

$$-\frac{c_\parallel^2}{\omega_L^2} \Delta u + \frac{4}{5} a_H u = -g_a \eta_{jl} \frac{\partial}{\partial u}\left(\frac{1}{2} h_j h_l\right), \tag{9}$$

and the equation for v, which differs from Eq. (9) only in that u is replaced by v everywhere. Equation (9) can be solved by passing to the Fourier components:

$$u_\mathbf{k} = -\kappa^2 \left(\frac{5g_a}{4a_H}\right) \frac{\partial}{\partial u}\left(\frac{1}{2} h_j h_l\right) \frac{\eta_{jl}(\mathbf{k})}{\mathbf{k}^2 + \kappa^2}, \tag{10}$$

where $\kappa^2 = 4a_H \omega_L^2 / 5c_\parallel^2$. We can now find

$$\langle u^2(\mathbf{r}) \rangle = \left(\kappa^2 \frac{5g_a}{4a_H}\right)^2 \frac{\partial}{\partial u}\left(\frac{1}{2} h_j h_m\right)$$

$$\times \frac{\partial}{\partial u}\left(\frac{1}{2} h_l h_n\right) \int \frac{d^3k}{(2\pi)^3} \frac{K_{mjln}(\mathbf{k})}{(k^2 + \kappa^2)^2}. \tag{11}$$

A similar expression can also be obtained for $\langle v^2(\mathbf{r}) \rangle$. Considering that $\langle \beta^2 \rangle = \langle u^2 \rangle + \langle v^2 \rangle$ and using formula (3) for $K_{mjln}(\mathbf{k})$, we can write

$$\langle \beta^2 \rangle = \frac{3}{20\pi} \kappa^2 \left(\frac{5g_a}{4a_H}\right)^2 [2\Phi_0 + 7\Phi_1 + \Phi_2]. \tag{12}$$

The quantities Φ_0, Φ_1, and Φ_2 are the values of the corresponding functions $\Phi_0(k)$, $\Phi_1(k)$, and $\Phi_2(k)$ for $\mathbf{k} = 0$ and have the same order of magnitude as the third power of the correlation radius r_c of field $\eta_{jl}(\mathbf{r})$. We can expect that $r_c \sim 300$–1000 Å. The indeterminacy in the value of r_c strongly affects the estimate of $\langle \beta^2 \rangle$. In accordance with formula (12), the value of $\langle \beta^2 \rangle$ is determined by the product of two factors: $(\kappa r_c)^3 (5g_a/4a_H)^2$, where κ is the reciprocal "healing length" of the texture in a magnetic field, which is proportional to the mag-

netic field. In the field of 300 Oe and not very close to T_c, $\kappa \approx 20$ cm^{-1} [6]. If we put $r_c \approx 500$ Å, $(\kappa r_c)^3 \approx 10^{-12}$. Estimation of the second factor gives $\approx 10^9$; i.e., we have in all $\langle \beta^2 \rangle \approx 10^{-3}$, and the aerogel virtually unaffects the texture under these conditions. The same formula shows, however, that $\langle \beta^2 \rangle \sim H^3$ and $\langle \beta^2 \rangle \sim 1$ for an order-of-magnitude stronger magnetic field. Another important characteristic of random texture is the characteristic length over which the correlations of angle β decay. The correlation function $\langle \beta(\mathbf{r})\beta(\mathbf{r}') \rangle$ can be expressed in terms of $K_{jlmn}(\mathbf{k})$ in the same way as was done while evaluating $\langle \beta^2 \rangle$. The expression obtained for the correlator of angles is cumbersome in view of the complexity of the structure of $K_{jlmn}(\mathbf{k})$. It is only significant for us that for large values of $|\mathbf{r} - \mathbf{r}'|$, the decay of correlations of angle β is determined by the factor $\exp[-\kappa|\mathbf{r} - \mathbf{r}'|]$; i.e., the correlation length is equal to $1/\kappa$. In the field ~ 1 kOe, this length is $\sim 10^{-2}$ cm; i.e., it is not very small compared to the size of conventional experimental cells. Thus, the emerging random variation of texture is of the mesoscopic type. The properties determined by the texture may differ considerably in different experiments. The relations for the mean values must be satisfied after averaging over a large number of experiments.

ACKNOWLEDGMENTS

REFERENCES

1. J. V. Porto and J. M. Parpia, Phys. Rev. Lett. **74**, 4667 (1995).

2. A. I. Larkin, Pis'ma Zh. Éksp. Teor. Fiz. **2**, 205 (1965) [JETP Lett. **2**, 130 (1965)].

3. A. A. Abrikosov and L. P. Gor'kov, Zh. Éksp. Teor. Fiz. **39**, 1781 (1960) [Sov. Phys. JETP **12**, 1243 (1961)].

4. E. V. Thuneberg, cond-mat/9802044 (1998).

5. G. E. Volovik, Pis'ma Zh. Éksp. Teor. Fiz. **63**, 281 (1996) [JETP Lett. **63**, 301 (1996)].

6. B. I. Barker, Y. Lee, L. Polukhina, *et al.*, Phys. Rev. Lett. **85**, 2148 (2000).

Translated by N. Wadhwa

Critical Current in SFIFS Junctions[1]

A. A. Golubov[1], M. Yu. Kupriyanov[2], and Ya. V. Fominov[3, 1]

[1] Department of Applied Physics, University of Twente, 7500 AE, Enschede, The Netherlands
e-mail: a.golubov@tn.utwente.nl

[2] Nuclear Physics Institute, Moscow State University, Moscow, 119899 Russia
e-mail: mkupr@pn.sinp.msu.ru

[3] Landau Institute for Theoretical Physics, Russian Academy of Sciences, 117940 Moscow, Russia
e-mail: fominov@landau.ac.ru

Received January 17, 2002

A quantitative theory of the Josephson effect in SFIFS junctions (S denotes bulk superconductor, F is metallic ferromagnet, and I is insulating barrier) is presented in the dirty limit. A fully self-consistent numerical procedure is employed to solve the Usadel equations for arbitrary values of the F-layer thicknesses, magnetizations, and interface parameters. In the case of antiparallel ferromagnet magnetizations, the effect of critical current I_c enhancement by the exchange energy H is observed, while in the case of parallel magnetizations the junction exhibits a transition to the π state. In the limit of thin F layers, we study these peculiarities of the critical current analytically and explain them qualitatively; the scenario of the 0–π transition in our case differs from those studied before. The effect of switching between 0 and π states by changing the mutual orientation of F layers is demonstrated. © 2002 MAIK "Nauka/Interperiodica".

PACS numbers: 74.50.+r; 74.80.Dm; 74.60.Jg; 75.30.Et

Josephson structures involving ferromagnets as weak link material are presently a subject of intensive study. The possibility of the so-called "π state" (characterized by the negative sign of the critical current I_c) in SFS Josephson junctions was predicted theoretically [1–8]. The first experimental observation of the crossover from the 0 to the I_c state was reported by Ryazanov *et al.* [9] and explained in terms of temperature dependent spatial oscillations of induced superconducting ordering in the diffusive F layer.

More recently, a number of new phenomena were predicted in junctions with more than one magnetically ordered layer. First, the possibility of critical current enhancement by the exchange field in SFIFS Josephson junctions with thin F layers and antiparallel magnetization directions was discussed in the regimes of small S-layer thicknesses [10] and bulk S electrodes [11, 12]. Second, the crossover to the π state was predicted in [11] for the parallel case even in the absence of the order parameter oscillations in thin F layers. Still, the physical explanation of these effects and accurate calculation of their magnitude have not been given so far. To make such estimates in the model with thin S electrodes, one must consider KO-1 type solutions [13] and take into account spatial variation of the superconducting state in the SF bilayers; at the same time, in the bulk S case an approximate method was used in [11] beyond its applicability range [12]. This problem is of a rather general nature, since one may expect from previous

knowledge (see, e.g., review [14]) that the supercurrent in a short weak link is H independent.

The above intriguing scenario motivated us to attack the problem of the Josephson effect in SFIFS junctions by self-consistent solution of the Usadel equations for arbitrary thicknesses of the F layers, barrier transparencies, and exchange field orientations. Below, we show that the 0–π transition in the case of parallel H orientation or enhancement of I_c by H in the antiparallel case with thin F layers occurs when the effective energy shift in the ferromagnets (due to the exchange field) becomes equal to a local value of the effective energy gap induced into an F layer. Under this condition, a peak in the local density of states (DoS) near the SF interfaces is shifted to zero energy. In the models with DoS of the BCS type, this leads to logarithmic divergence of I_c in the antiparallel case at zero temperature, similarly to the well-known Riedel singularity of *ac* supercurrent in SIS tunnel junctions at voltage $eV = 2\Delta$. We also describe the general numerical method to solve the problem self-consistently and apply it for quantitative description of the 0–π transition and I_c enhancement in SFIFS junctions.

The model. We consider the structure of the SFIFS type, where I is an insulating barrier of arbitrary strength. We assume that the S layers are bulk and that the dirty limit conditions are fulfilled in the S and F metals. Although our method is applicable in the general situation of different ferromagnets and superconductors, for simplicity, below we illustrate our results in

---

[1] This article was submitted by the authors in English.

the case where equivalent S and F materials are used on both sides of the structure (although the directions of the exchange field in the two F layers may be different), both F layers have the thickness d_F, and the two SF interfaces have the same transparency. At the same time, we do not put any limitations on d_F and the transparency.

The Usadel functions G, F obey the normalization condition $G_\omega^2 + F_\omega F_{-\omega}^* = 1$, which allows the following parameterization in terms of the new function Φ:

$$G_\omega = \frac{\tilde{\omega}}{\sqrt{\tilde{\omega}^2 + \Phi_\omega \Phi_{-\omega}^*}}, \quad F_\omega = \frac{\Phi_\omega}{\sqrt{\tilde{\omega}^2 + \Phi_\omega \Phi_{-\omega}^*}}. \quad (1)$$

The quantity $\tilde{\omega} = \omega + iH$ corresponds to the general case where the exchange energy H is present. However, in the S layers, $H = 0$ and we have simply $\tilde{\omega} = \omega$.

We choose the x axis perpendicular to the plane of the interfaces with the origin at the barrier I. The Usadel equations [15] in the S and F layers have the form

$$\xi_S^2 \frac{\pi T_c}{\omega G_S} \frac{\partial}{\partial x} \left[G_S^2 \frac{\partial}{\partial x} \Phi_S \right] - \Phi_S = -\Delta, \quad (2)$$

$$\xi_F^2 \frac{\pi T_c}{\tilde{\omega} G_F} \frac{\partial}{\partial x} \left[G_F^2 \frac{\partial}{\partial x} \Phi_F \right] - \Phi_F = 0, \quad (3)$$

where T_c is the critical temperature of the superconductors, Δ is the pair potential (which is nonzero only in the S layers), ω is the Matsubara frequency, and the coherence lengths ξ are related to the diffusion constants D as $\xi_{S(F)} = \sqrt{D_{S(F)}/2\pi T_c}$. The pair potential satisfies the self-consistency equations

$$\Delta \ln \frac{T}{T_c} + \pi T \sum_\omega \frac{\Delta - G_S \Phi_S \operatorname{sgn} \omega}{|\omega|} = 0. \quad (4)$$

In this paper, we restrict ourselves to the cases of parallel and antiparallel orientations of the exchange fields H in the ferromagnets.

The boundary conditions at the SF interfaces ($x = \mp d_F$) have the form [16] (see [17] for detail)

$$\frac{\xi_S G_S^2}{\omega} \frac{\partial}{\partial x} \Phi_S = \gamma \frac{\xi_F G_F^2}{\tilde{\omega}} \frac{\partial}{\partial x} \Phi_F, \quad (5)$$

$$\pm \gamma_B \frac{\xi_F G_F}{\tilde{\omega}} \frac{\partial}{\partial x} = G_S \left(\frac{\Phi_F}{\tilde{\omega}} - \frac{\Phi_S}{\omega} \right), \quad (6)$$

with

$$\gamma_B = R_B \mathcal{A}/\rho_F \xi_F, \quad \gamma = \rho_S \xi_S/\rho_F \xi_F,$$

where R_B and $\mathcal{A}$ are the resistance and the area of the SF interfaces, respectively; and $\rho_{S(F)}$ is the resistivity of the S (F) layer. At the I interface ($x = 0$), the boundary

conditions read

$$\frac{G_{F1}^2}{\tilde{\omega}_1} \frac{\partial}{\partial x} \Phi_{F1} = \frac{G_{F2}^2}{\tilde{\omega}_2} \frac{\partial}{\partial x} \Phi_{F2}, \quad (7)$$

$$\gamma_{B,I} \frac{\xi_F G_{F1}}{\tilde{\omega}_1} \frac{\partial}{\partial x} \Phi_{F1} = G_{F2} \left(\frac{\Phi_{F2}}{\tilde{\omega}_2} - \frac{\Phi_{F1}}{\tilde{\omega}_1} \right), \quad (8)$$

with

$$\gamma_{B,I} = R_{B,I} \mathcal{A}/\rho_F \xi_F,$$

where the indices 1, 2 refer to the left and right side of the I interface, respectively.

In the bulk of the S electrodes, we assume a uniform current-carrying superconducting state

$$\Phi(x = \mp\infty) = \frac{\Delta_0 \exp(i[\mp\varphi/2 + 2mv_s x])}{1 + 2D_S m^2 v_s^2/\sqrt{\omega^2 + |\Phi|^2}}, \quad (9)$$

where m is the electron mass, v_s is the superfluid velocity, and φ is the phase difference across the junction.

The supercurrent density is constant across the system. In the F part, it is given by the expression

$$J = \frac{i\pi T}{2e\rho} \sum_\omega \frac{G^2(\omega)}{\tilde{\omega}^2} \left[\Phi_\omega \frac{\partial}{\partial x} \Phi_{-\omega}^* - \Phi_{-\omega}^* \frac{\partial}{\partial x} \Phi_\omega \right], \quad (10)$$

while an analogous formula for the S part is obtained if we substitute $\tilde{\omega} \longrightarrow \omega$. This expression, together with the boundary condition (8) and the symmetry relation $F(-\omega, H) = F(\omega, -H)$, yields the formula for the supercurrent across the I interface:

$$I = \frac{\pi T}{e R_{B,I}} \sum_\omega \operatorname{Im}[F_{F1}^*(-H_1) F_{F2}(H_2)] \quad (11)$$

(the functions F are related to Φ via Eq. (1)).

The limit of small F-layer thickness: $d_F \ll \min(\xi_F, \sqrt{D_F/2H})$. Under the condition $\gamma_B/\gamma \gg 1$, we can neglect the suppression of superconductivity in the superconductors. We further assume that the transparency of the I barrier is small, $\gamma_{B,I} \gg \max(1, \gamma_B)$, and the SF bilayers are decoupled (the exact criterion will be given below). In this case, we can set $v_s = 0$ and expand the solution of Eq. (3) in the F layers up to the second order in small spatial gradients. Applying the boundary condition (6), we obtain the solution in a form similar to that in the SN bilayer [18, 17]:

$$\Phi_{F1,F2} = \frac{\tilde{\omega}_{1,2}/\omega}{1 + \gamma_{BM} \tilde{\omega}_{1,2}/\pi T_c G_S} \Delta_0 \exp(\mp i\varphi/2), \quad (12)$$

with

$$\gamma_{BM} = \gamma_B d_F/\xi_F, \quad G_S = \omega/\sqrt{\omega^2 + \Delta_0^2}.$$

Substituting Eq. (12) into the expression for the supercurrent (11), we obtain $I(\varphi) = I_c \sin\varphi$.

For the parallel orientation of the exchange fields, $H_1 = H_2 = H$, the critical current is

$$
I_c^{(p)} = \frac{2\pi T}{e R_{B,I}} \sum_{\Omega > 0} \frac{\delta^2 G_S^2}{\Omega^2} \frac{1 - \alpha + \Omega \gamma_{BM} g_1}{(1 - \alpha + \Omega \gamma_{BM} g_1)^2 + 4\alpha g_2}, \quad (13)
$$

where $\Omega = \omega/\pi T_c$, $\delta = \Delta_0/\pi T_c$, $\alpha = (h\gamma_{BM})^2$, $h = H/\pi T_c$, $g_1 = 2G_S + \gamma_{BM}\Omega$, and $g_2 = (G_S + \gamma_{BM}\Omega)^2$.

For the antiparallel orientation, $H_1 = -H_2 = H$, the critical current is given by

$$
I_c^{(a)} = \frac{2\pi T}{e R_{B,I}}
$$
$$
\times \sum_{\Omega > 0} \frac{\delta^2 G_S^2}{\Omega^2} \frac{1}{\sqrt{(1 - \alpha + \Omega \gamma_{BM} g_1)^2 + 4\alpha g_2}}. \quad (14)
$$

At $h = 1/\gamma_{BM}$ and small Ω, the expression in the sum in Eq. (14) behaves as $1/\Omega$; thus, at low T, the critical current diverges logarithmically: $I_c^{(a)} \propto \ln(T_c/T)$. This effect was pointed out earlier in [10, 11].

The above results become physically transparent in the real energy ε representation. Making an analytical continuation in Eqs. (1) and (12) by the replacement $\omega \longrightarrow -i\varepsilon$, we obtain the expression for the DoS per one spin projection (spin "up") $N_F(\varepsilon) = \mathrm{Re}\, G_F(\varepsilon)$ in the F layers

$$
N_F(\varepsilon) = \left| \mathrm{Re} \frac{\tilde{\varepsilon}}{\sqrt{\tilde{\varepsilon}^2 - \Delta_0^2}} \right|, \quad (15)
$$
$$
\tilde{\varepsilon} = \varepsilon + \gamma_{BM}(\varepsilon - H)\sqrt{\Delta_0^2 - \varepsilon^2}/\pi T_c,
$$

which demonstrates the energy renormalization due to the exchange field. Equation (15) yields $N_F(0) = \mathrm{Re}(\gamma_{BM}h/\sqrt{(\gamma_{BM}h)^2 - 1})$, which shows that at $h = 1/\gamma_{BM}$ the singularity in the DoS is shifted to the Fermi level. Exactly at this value of h the maximum of $I_c^{(a)}$ is achieved due to overlap at two $\varepsilon^{-1/2}$ singularities. This leads to logarithmic divergence of the critical current (14) in the limit $T \longrightarrow 0$, similarly to the well-known Riedel singularity of a nonstationary supercurrent in SIS tunnel junctions at voltage $eV = 2\Delta_0$, where the energy shift is due to the electric potential. At the same value of the exchange field $h = 1/\gamma_{BM}$, the critical current changes its sign (i.e., the crossover from the 0 to the π contact occurs) for parallel magnetizations in the F layers [see Eq. (13)]. We emphasize that the scenario of the $0-\pi$ transition in our case differs from those studied before, where the π shift of the phase was either due to spatial oscillations of the order parameter in F layers or due to the proximity-induced phase rotation in S layers. In our case, the phase does not change in either layer; instead, it jumps at the SF interfaces. This scenario is most clearly illustrated in the limit of large H where

Eqs. (1) and (12) yield $F_F \propto -i\Delta \,\mathrm{sgn}\, H$, whereas $F_S \propto \Delta$; thus the phase jumps by $\pi/2$ at each of the SF interfaces, providing the total π shift between $F_{F1}(-H)$ and $F_{F2}(H)$ [it is the phase difference between these two functions that determines the supercurrent according to Eq. (11)].

The considered effects take place only for sufficiently low I-barrier transparency. Indeed, it follows from Eq. (12) that $G_F(\Omega) \propto 1/\sqrt{\Omega}$ for small Ω under the condition $h = 1/\gamma_{BM}$. As a result, the boundary condition (8) results in that, at

$$
\Omega \leq \min\left(\frac{\xi_F}{d_F \gamma_{B,I}}, \frac{\gamma_B}{\gamma_{B,I}} \right), \quad (16)
$$

the solutions (12) are not valid, since in this frequency range the effective transparency of the I interface (the parameter $G_{F1} G_{F2}/\gamma_{B,I}$ [19]) increases and the spatial gradients in the F layers become large (the limit of large gradients is called "the KO-1 case" [13, 14]). In this case, the nongradient term in Eq. (3) can be neglected and the general solution of the Usadel equation in the F layers has the KO-1 form [13]:

$$
\frac{\Phi}{\tilde{\omega}} = \frac{C - iM \arctan[M(Bx + Q)]}{1 - \eta}, \quad (17)
$$

where $M = \sqrt{(\eta^2 - 1) - C^2}$, while C, B, Q, and η are integration constants. From Eqs. (1) and (17), it follows that the Green's functions G, F and hence the contribution to the critical current from these frequencies are H independent. As a result, the barrier transparency parameter $\gamma_{B,I}$ provides the cutoff of the low-temperature logarithmic singularity of $I_c^{(a)}$ at $h = 1/\gamma_{BM}$ [see Eq. (14)]. According to Eq. (16), the critical current saturates at low temperature $T^* = T_c \min(\xi_F/d_F \gamma_{B,I}, \gamma_B/\gamma_{B,I})$. We note that any asymmetry in the SFIFS junction will also lead to the cutoff of $I_c^{(a)}$ divergency [19]. The above estimates are made for the case of low barrier transparency, $\xi_F/d_F \gamma_{B,I} \ll 1$ and $\gamma_B/\gamma_{B,I} \ll 1$. The opposite regime of high transparency deserves separate study.

The general case. For arbitrary F-layer thicknesses and interface parameters, the boundary problem (1)–(9) was solved numerically using the iterative procedure. Starting from trial values of the complex pair potentials Δ and the Green's functions $G_{S,F}$, we solve the resulting linear equations and boundary conditions for functions $\Phi_{S,F}$. After this, we recalculate $G_{S,F}$ and Δ. Then, we repeat the iterations until convergency is reached. The self-consistency of calculations is checked by the condition of conservation of the supercurrent (10) across the junction. We emphasize that our method is *fully* self-consistent; in particular, it includes the self-consistency over the superfluid velocity v_s, which is essential (contrary to the constriction case) in the quasi-one-
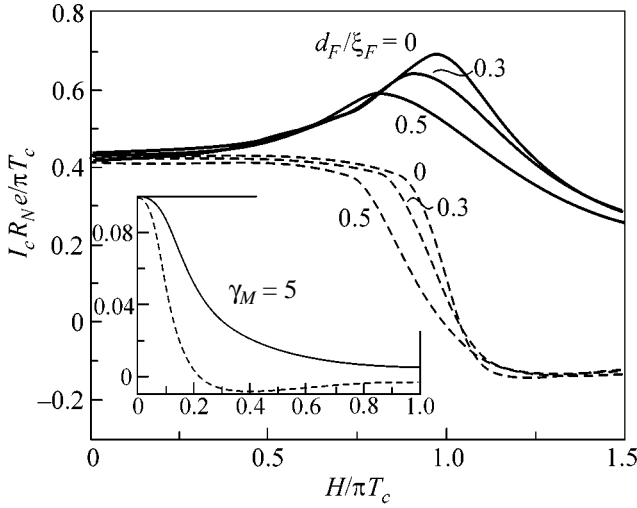
Fig. 1. Enhancement of the critical current (antiparallel magnetizations, solid lines) and the 0–π transition at which I_c changes its sign (parallel magnetizations, dashed lines) in the SFIFS junction at $T/T_c = 0.05$, $\gamma_{BM} = 1$, and $\gamma_M = 0$. Inset: the same for large values of γ_M (when $d_F \ll \xi_F$, the results depend only on this parameter).

Fig. 2. Enhancement of the critical current (antiparallel magnetizations, solid lines) and the 0–π transition at which I_c changes its sign (parallel magnetizations, dashed lines) in the SFIFS junction: influence of temperature and barrier transparency. The dotted line corresponds to $T/T_c = 0.01$ and $\xi_F/d_F\gamma_{B,I} = 0$; the parameters for other curves are given in the figure.

dimensional geometry. The details of our numerical method will be presented elsewhere [19].

Figure 1 shows $I_c(H)$ dependences calculated at $T = 0.05T_c$ from the numerical solution of the boundary problem (1)–(9) for the fixed value of $\gamma_{BM} = 1$ and a set of different F-layer thicknesses and SF interface parameters γ. The normal junction resistance is $R_N = R_{B,I} + 2R_B + 2\rho_F d_F/\mathcal{A}$. The curves $d_F/\xi_F = 0$ are the limits of the vanishing d_F/ξ_F ratio at fixed γ_{BM} and are calculated from Eqs. (13) and (14). For thin F layers, the results depend only on the combination $\gamma_M = \gamma d_F/\xi_F$. The enhancement of I_c and the crossover to the π state are clearly seen for the antiparallel and parallel orientations, respectively. In accordance with the estimates given above, these effects take place for the values of the exchange field H close to πT_c. The enhancement disappears with increasing gradients in the F layers, since the solution to Eq. (12) loses its validity. This is illustrated in Fig. 1 by increasing the thickness d_F or γ_M. In particular, in the case of large γ_M the enhancement is absent, in contrast to the statement in [11] (see [12]).

The influence of temperature and barrier transparency on the critical current anomaly is shown in Fig. 2. One can see that, in accordance with the above estimate, the cutoff of the $I_c^{(a)}$ singularity is provided by finite temperature or barrier transparency; i.e., with the decrease of the barrier strength parameter $\gamma_{B,I}$, the peak magnitude starts to drop when the ratio $d_F\gamma_{B,I}/\xi_F$ becomes comparable to T/T_c. With a further decrease of $d_F\gamma_{B,I}/\xi_F$, the singularity disappears, while the transition to the π state shifts to large values of H.
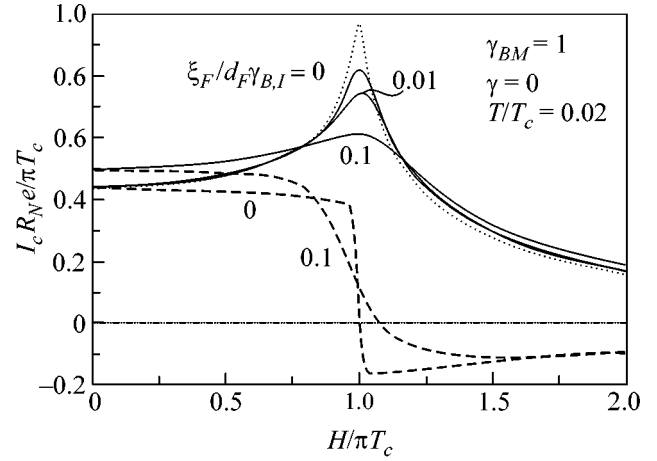
Figure 3 demonstrates the DoS in the F layers for a certain spin projection calculated numerically in the limit of small I-barrier transparency. At $H = 0$, we reproduce the well-known minigap existing in an SN bilayer. At finite H, the gap shifts in energy (asymmetrically) and the peak in the DoS reaches zero energy at $h = 1/\gamma_{BM}$. One can see that, even for a small value $\gamma_M = 0.05$, the peaks are rather broad; this is the reason why the singularity in $I_c^{(a)}$ is suppressed by γ_M very rapidly.

In the limit of finite F-layer thickness (see Fig. 4), which is of practical interest, the numerical calculations show monotonic suppression of I_c with an increase of
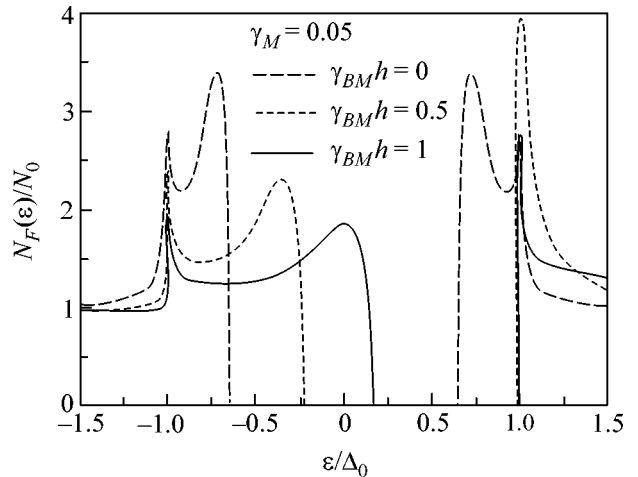

Fig. 3. Normalized density of states for spin "up" in the F layer for various exchange fields.
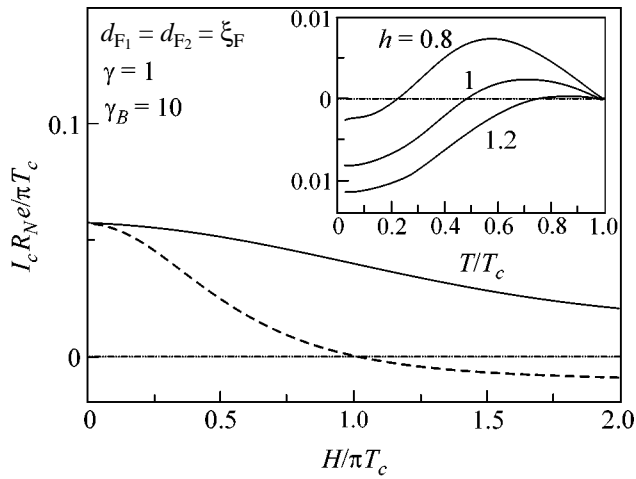
Fig. 4. Critical current in SF$_1$F$_2$S junction: switching effect. $T/T_c = 0.5$, the solid and dashed lines correspond to the antiparallel and parallel orientations of magnetizations, respectively. Inset: thermally induced 0–π crossover in the parallel case.

the exchange field H for antiparallel magnetizations of the F layers and the 0–π crossover for the parallel case. One can see from Fig. 4 that, for given temperature and thickness of the F layers, it is possible to find the value of the exchange field at which switching between parallel and antiparallel orientations will lead to switching of I_c from near-zero to a finite value (or to switching between 0 and π states). This effect may be used for engineering cryoelectronic devices manipulating spin-polarized electrons.

The case of parallel F-layer magnetizations in the absence of the I barrier corresponds to the standard SFS junction where the 0–π transition is possible due to spatial oscillations of induced superconducting ordering in the F layer. The thermally induced 0–π crossover in an SFS junction was observed in [9], where a simple theory based on the linearized Usadel equations was also presented. Here, we show such a crossover (see the inset in Fig. 4) from the fully self-consistent solution in the range of the exchange fields corresponding to that of [9]. Comparison with the experimental data and more detailed results of our model will be given elsewhere [19].

In conclusion, we have presented a general method for solving Usadel equations in SFIFS junctions self-consistently. Using our method, we have theoretically investigated the Josephson current in SFIFS and SFS junctions as a function of relative F-layer magnetizations, thicknesses, and parameters of the S/F and F/F interfaces. We have identified the physical mechanisms of the critical current enhancement and of the 0–π transition in these junctions.

REFERENCES

1. L. N. Bulaevskiĭ, V. V. Kuziĭ, and A. A. Sobyanin, Pis'ma Zh. Éksp. Teor. Fiz. **25**, 314 (1977) [JETP Lett. **25**, 290 (1977)].
2. A. I. Buzdin, L. N. Bulaevskiĭ, and S. V. Panyukov, Pis'ma Zh. Éksp. Teor. Fiz. **35**, 147 (1982) [JETP Lett. **35**, 178 (1982)].
3. A. I. Buzdin and M. Yu. Kupriyanov, Pis'ma Zh. Éksp. Teor. Fiz. **53**, 308 (1991) [JETP Lett. **53**, 321 (1991)].
4. A. I. Buzdin, B. Vujičić, and M. Yu. Kupriyanov, Zh. Éksp. Teor. Fiz. **101**, 231 (1992) [Sov. Phys. JETP **74**, 124 (1992)].
5. E. A. Koshina and V. N. Krivoruchko, Pis'ma Zh. Éksp. Teor. Fiz. **71**, 182 (2000) [JETP Lett. **71**, 123 (2000)].
6. L. Dobrosavljević-Grujić, R. Zikić, and Z. Radović, Physica C (Amsterdam) **331**, 254 (2000).
7. N. M. Chtchelkatchev, W. Belzig, Yu. V. Nazarov, and C. Bruder, Pis'ma Zh. Éksp. Teor. Fiz. **74**, 357 (2001) [JETP Lett. **74**, 323 (2001)].
8. Yu. S. Barash and I. V. Bobkova, cond-mat/0108200.
9. V. V. Ryazanov, V. A. Oboznov, A. Yu. Rusanov, *et al.*, Phys. Rev. Lett. **86**, 2427 (2001); V. V. Ryazanov, V. A. Oboznov, A. V. Veretennikov, *et al.*, Usp. Fiz. Nauk, Suppl. **171**, 81 (2001).
10. F. S. Bergeret, A. F. Volkov, and K. B. Efetov, Phys. Rev. Lett. **86**, 3140 (2001).
11. V. N. Krivoruchko and E. A. Koshina, Phys. Rev. B **63**, 224 515 (2001); **64**, 172 511 (2001).
12. In Ref. [11] there was an attempt to study the influence of the suppression parameter γ_M on the critical current in SFIFS junctions. The obtained $I_c(H)$ dependences only qualitatively show the effects discussed in [10] and in this paper. To obtain quantitative accuracy in the small γ_M limit, it is necessary to take into account self-consistently the corrections to the pair potential, as it was done in V. F. Lukichev, Fiz. Nizk. Temp. **10**, 1219 (1984) [Sov. J. Low Temp. Phys. **10**, 639 (1984)]. The calculation in the large γ_M limit in [11] is valid for $T \gg T_c/\gamma_M^2$, while the effect of $I_c^{(a)}$ enhancement exists only at low T.
13. I. O. Kulik and A. N. Omel'yanchuk, Fiz. Nizk. Temp. **3**, 945 (1977) [Sov. J. Low Temp. Phys. **3**, 459 (1977)].
14. K. K. Likharev, Rev. Mod. Phys. **51**, 101 (1979).
15. K. D. Usadel, Phys. Rev. Lett. **25**, 507 (1970).
16. M. Yu. Kupriyanov and V. F. Lukichev, Zh. Éksp. Teor. Fiz. **94**, 139 (1988) [Sov. Phys. JETP **67**, 1163 (1988)].
17. E. A. Koshina and V. N. Krivoruchko, Fiz. Nizk. Temp. **26**, 157 (2000) [Low Temp. Phys. **26**, 115 (2000)].
18. A. A. Golubov and M. Yu. Kupriyanov, Zh. Éksp. Teor. Fiz. **96**, 1420 (1989) [Sov. Phys. JETP **69**, 805 (1989)].
19. A. A. Golubov, M. Yu. Kupriyanov, and Ya. V. Fominov, in preparation.

Angular Dependence of the Upper Critical Field in Bi₂Sr₂CuO₆₊δ[1]

S. I. Vedeneev[1, 2, *], and Yu. N. Ovchinnikov[3, 4]

[1] *Lebedev Physical Institute, Russian Academy of Sciences, Moscow, 117924 Russia*
e-mail: vedeneev@sci.lebedev.ru
[2] *Grenoble High Magnetic Field Laboratory, Max-PIanck-Institut für Festkorperforschung*
and Centre National de la Recherche Scientinque, F-38042 Grenoble, France
[3] *Landau Institute for Theoretical Physics, Russian Academy of Sciences, Moscow, 117940 Russia*
[4] *Centre de Recherches sur les Très Basses Températures, Centre National de la Recherche Scientifique,*
F-38042 Grenoble, France

Received January 17, 2002

The angular dependence of the upper critical magnetic field was investigated in a wide range of temperatures in very high-quality Bi₂Sr₂CuO₆₊δ single crystals with critical temperature T_c (midpoint) ≃ 9 K in magnetic fields up to 28 T. Although the typical value of the normal state resistivity ratio $\rho_c/\rho_{ab} \approx 10^4$, the anisotropy ratio $H_{c2\,\|\,ab}/H_{c2\,\perp\,ab}$ of the upper critical fields is much smaller and shows an unexpected temperature dependence. A model based on strong anisotropy and small transparency between superconducting layers is proposed. © 2002 MAIK "Nauka/Interperiodica".

PACS numbers: 74.25.Ha; 74.60.Ec; 74.72.Hs

One of the puzzling phenomena of high-T_c super-conductors (HTSC) is the anomalous positive curvature of the temperature dependence of the upper critical field H_{c2}, which was observed in some superconducting oxides [1–4]. The magnitude of the critical field at zero temperature was far in excess of the Werthamer–Helfand–Hohenberg extrapolation [5], and no quadratic saturation of H_{c2} was found at temperatures in the mK range for low-critical-temperature Tl₂Ba₂CuO₆ single crystals [1] and Bi₂Sr₂CuO₆ films [2]. In addition, it was deduced from measurements in 61-T pulsed magnetic fields applied parallel to the c axis that the shape of $H_{c2}(T)$ in the high-T_c cuprates depends on the anisotropy of the materials, becoming more conventional as the normal state anisotropy gets smaller [6]. The authors argued that the normal state anisotropy plays a key role in determining the curvature of $H_{c2}(T)$ [6]. However, in different models [7–9], which have been proposed to account for the upward curvature in $H_{c2}(T)$, the effect of anisotropy is not important. This problem of anisotropy in the superconducting properties is related to the more general question for the understanding of high-T_c superconductivity on the basis of the normal-state properties.

In transport measurements on the low-T_c phase Bi₂Sr₂CuO₆ (Bi2201), we obtained a much smaller (nearly two orders of magnitude) anisotropy for the superconducting critical field than for the normal-state resistivity. To explain this contrasting behavior with respect to the situation for Bi₂Sr₂CaCu₂O₈ (Bi2212) where both measured anisotropies are comparable [10], we analyzed the angular dependence of the upper critical field in a model based on weakly coupled superconducting layers.

The anisotropy is usually expressed by the ratio $\gamma = \sqrt{m_c/m_{ab}}$ between the effective masses of the quasiparticles along the c axis and the ab plane, which can be related to the transport anisotropy with $\gamma \simeq \sqrt{\rho_c/\rho_{ab}}$ using $\rho = m/ne^2\tau$ for the out-of-plane resistivity ρ_c and in-plane resistivity ρ_{ab} [8, 10]. For the three-dimensional (3D) limit with the superconducting coherence length ξ_c larger than the interlayer distance s, the anisotropic Ginzburg–Landau (AGL) relation $H_{c2}(\theta) = H_{c2\,\|\,ab}(\cos^2\theta + \gamma^2\sin^2\theta)^{-0.5}$ describes the angular dependence of the upper critical field, with $\gamma = H_{c2\,\|\,ab}/H_{c2\,\perp\,ab} = \sqrt{m_c/m_{ab}}$ for the applied field $H \parallel ab$ plane and $H \perp ab$ plane [11]. Here, θ is the angle between the magnetic field and the ab-plane. For layered superconductors with a high degree of anisotropy, such that $\xi_c(T) < s$, a 2D situation with decoupled layers arises. For such a thin-film superconductor in the vicinity of a critical temperature T_c (in the GL approximation), Tinkham has proposed a qualitative model with the angular dependence $|H_{c2}(\theta)\sin\theta/H_{c2\,\perp\,ab}| + [H_{c2}(\theta)\cos\theta/H_{c2\,\|\,ab}]^2 = 1$ [12]. The thin-film model results in a cusp at $\theta = 0°$ with

---

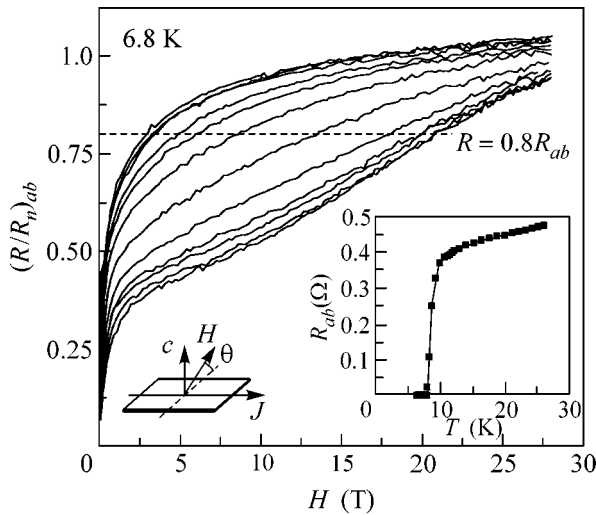[1] This article was submitted by the authors in English.

Fig. 1. In-plane resistive transitions of sample no. 1 as a function of applied field for various field orientations relative to the *ab* plane of the crystal at 6.8 K. Angle θ from above is 90°, 72°, 54°, 36°, 27°, 18°, 9°, 4.5°, 2.7°, 1.8°, 0.9°, 0°. The resistance has been normalized to extrapolated normal-state resistance R_n at the highest fields. The inset shows the temperature-dependent superconducting transition of the same sample.
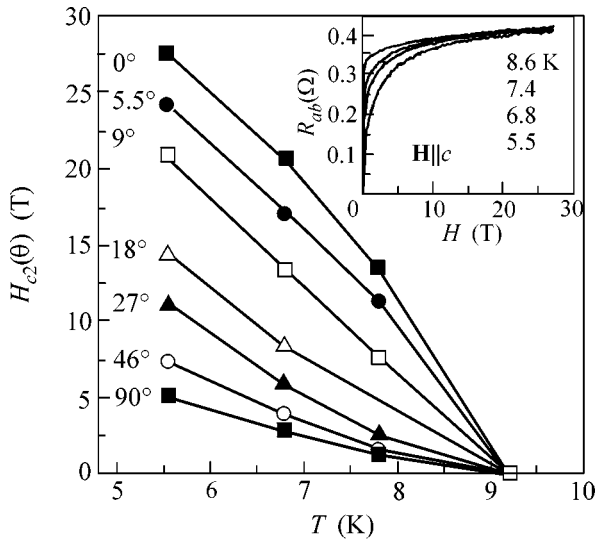

Fig. 2. Temperature dependencies of the upper critical field $H_{c2}^*(T)$ for sample no. 1 at various angles H_{c2}^* extracted from the 80%-resistive transitions of the crystals. The inset shows the magnetoresistance curves for the same sample at various temperatures with the field direction perpendicular to the *ab*-plane of the crystal.

$dH_{c2}/d\theta \neq 0$; this behaviour has been observed in superconducting multilayers [13]. An important feature is that both models predict a temperature-independent critical-field anisotropy $H_{c2\,\|\,ab}/H_{c2\,\perp\,ab}$.

For $YBa_2Cu_3O_7$ with a not too strong anisotropy (typically $\gamma \simeq 10$–30), there are indications for a dimensional crossover from 3D to 2D with decreasing temperature [14, 15]; for Bi2212 with γ values up to 1000, deviations from the AGL theory have been observed in resistivity experiments in the vicinity of T_c by Palstra *et al.* [16], but without a clear indication of the dimensional crossover. In similar experiments with a better angular resolution, Marcon *et al.* [17] and Naughton *et al.* [18] have found the 2D behavior in Bi2212 crystals. Because of the high H_{c2} values in these systems, a direct determination of the H_{c2} anisotropy can only be done close to T_c. To extend the temperature region further below T_c, the anisotropy of irreversibility has been investigated.

The low T_c of Bi2201 does not restrict the critical field studies to temperatures close to T_c while its structure and properties are closely related to HTSC. Single crystals of the pure Bi2201-phase are difficult to grow, because the crystals are nonstoichiometric and, as a rule, not perfect. For this reason, most of the measurements were carried out on single-phase La-doped Bi2201 single crystals. The three, slightly overdoped crystals investigated in this study were grown without doping by the KCL solution-melt method with the stoichiometry $Bi_{2+x}Sr_{2-(x+y)}Cu_{1+y}O_{6+\delta}$ and with excess Bi in order to have good quality single crystals [19]. The zero-field critical temperatures defined by the 10% and 90% points of the resistive transition equal to 8.1–9.8, 8.7–9.5, and 8.1–8.9 K for samples nos. 1, 2, and 3, respectively. In the inset of Fig. 1, we have plotted the temperature dependence of the resistive transition for sample no. 1. In the four-probe resistance measurements, the transport current was in the *ab*-plane of the crystals and orthogonal to the field in all cases. The angular resolution was better than half a degree with the θ = 0° orientation obtained from the highest value of $H_{c2}(0)_{c2\,\|\,ab}$.

Figure 1 shows the in-plane resistive transitions for sample no. 1 at 6.8 K as a function of applied field for various field orientations relative to the *ab*-plane of the crystal. The resistance has been normalized to the extrapolated high-field normal-state resistance R_n. The inset in Fig. 2 shows the magnetoresistance curves for the same sample at various temperatures with the field direction perpendicular to the *ab*-phase of the crystal. In spite of the strong broadening of the magnetic transitions at high temperatures one can see in the inset that the resistive transitions in the normal state are completed at $H > 13$ T, even at $T = 5.5$ K (the weak increase of the normal-state resistance is due to a magnetoresistance contribution in high magnetic fields).

The field-induced resistive transitions for samples nos. 2 and 3 were similar to those shown in Fig. 1. The influence of the flux-flow dissipation on the broadening of the superconducting transition becomes less noticeable for a critical field determination close to R_n [16, 20,

6]. In support of this, we display in Fig. 2 the $H_{c2}^*(T)$ phase diagram for sample no. 1 at various angles θ obtained from a 80% criterion of its normal-state value R_n. For the lowest θ values, these temperature dependencies are analogous to the dependence for conventional type II superconductors. The phase diagram obtained from the $R = 0.5R_n$ criterion exhibited for all field orientations a strong anomalous concave upturn of $H_{c2}^*(T)$.

In Fig. 3, we show $H_{c2}^*(\theta)$ for sample no. 1 at 6.8 and 5.55 K. The inset shows similar data for sample no. 2 at 1.42 and 0.82 and for sample no. 3 at 4.2 K (data points). For the angular dependence $H_{c2}^*(\theta)$ a good agreement is found with the 3D AGL model with anisotropy parameters $\gamma = H_{c2\,\|\,ab}/H_{c2\,\perp\,ab}$ equal to 9.8, 7.15, and 5.3 at 7.8, 6.8, and 5.55K, respectively, (crystal no. 1). This anisotropy is much lower than $\gamma = \sqrt{\rho_c/\rho_{ab}}$ found from resistivity which equals 140 at 6 K. Moreover, the obtained anisotropy parameter γ varies with temperature, which is unexpected for a similar temperature dependence of the critical fields in the two field orientations. We conclude, therefore, that the anisotropy parameter γ of our Bi2201 single crystals cannot be deduced from the angular dependence of $H_{c2}(\theta)$ using the available models as has been done before for Bi2212.

A temperature dependent critical-field anisotropy was observed in layered low-T_c 2H–TaS$_2$ [21] and MoS$_2$ [22] single crystals intercalated with a variety of organic molecules and alkali metals. The data have been analyzed using the theory of dimensional crossover developed by Klemm *et at.* [23]. Klemm *et al.* have extended the Lawrence-Doniach model [24] and found the conditions necessary for observing crossover to a 2D behavior characterized by the temperature dependent critical-field anisotropy and a strong upward curvature in $H_{c2\,\|\,ab}$ vs *T*. In our case, the $H_{c2\,\|\,ab}^*(T)$ phase diagram obtained from an 80% criterion of its R_n does not show the upward curvature in $H_{c2\,\|\,ab}^*$ and is analogous to the dependence for conventional type II superconductors (Fig. 2 and [20]).

In the following, we propose a model for the observed critical-field anisotropy based on a superconductor with a high degree of anisotropy consisting of stacked two-dimensional superconducting planes with an effective thickness *d* coupled by weak Josephson coupling [24]. The upper critical field $H_{c2\,\|\,ab}^*$ is determined by the depairing currents in the *ab*-plane, and will be finite even for $\rho_c/\rho_{ab} \longrightarrow \infty$. We neglect spin effects so that $H_{c2\,\|\,ab}$ remains smaller than the paramagnetic limit. In this model, the upper critical field at an arbitrary orientation with respect to the crystal and an arbitrary temperature is determined by lowest eigen-
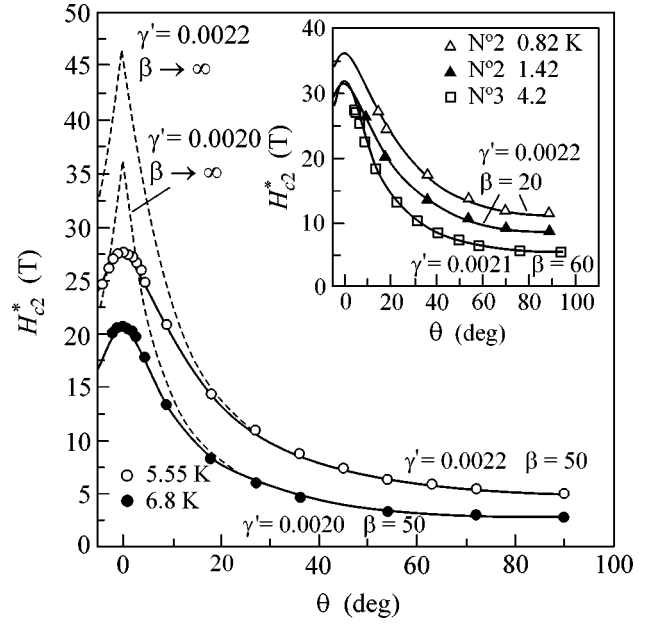

Fig. 3. Angular dependence of the upper critical field H_{c2}^* for sample no. 1 at 6.8 and 5.55 K. The inset shows similar data for the samples nos. 2 and 3 at lower temperatures. Full lines are fits of Eq. (4) to the experimental data for sample nos. 1, 2, and 3 (see also inset) with the indicated β and γ′ parameters. The long dashed lines show the result without angular broadening (β ⟶ ∞).

values of the operator $\hat{L} = -\left(\hbar\dfrac{\partial}{\partial \mathbf{r}} - \dfrac{1}{c}2ie\mathbf{A}\right)^2$, where **A** is the vector potential. For the magnetic field *H* oriented at an angle θ to the *ab*-plane (*xy* plane), the vector potential **A** can be written as

$$\mathbf{A} = (-Hy\sin\theta + Hz\cos\theta, 0, 0), \quad (1)$$

where *z* lies in the range of $-d/2 < z < d/2$. Under the assumption that the effective thickness *d* is less than the correlation length in the *ab*-plane of the crystal, the order parameter will be independent of *x* and *z* coordinates. In a strongly layered anisotropic superconductor for a magnetic field directed along one of the general axes of the crystal, the vortex cross section has the shape of an ellipse. At low transparency between layers, the small half-axis of the vortex can be less than *d*. The effective mass approximation is no longer valid. In this case, currents between the superconducting layers may be neglected and we can consider one single isolated layer with effective thickness *d*. As a result, the operator $\hat{L}$ is given by

$$\hat{L} = -\hbar^2\dfrac{\partial^2}{\partial y^2} + \dfrac{4e^2}{c^2}H^2y^2\sin^2\theta + \dfrac{4e^2}{c^2}H^2\cos^2\theta\langle z^2\rangle, \quad (2)$$

where $\langle z^2 \rangle = d^2/12$. From Eq. (2), we obtain the relationship between the angular dependent critical field $H(\theta)$ and the upper critical field $H_{c2 \perp ab}$:

$$H(\theta)\sin\theta + \gamma' H^2(\theta)\cos^2\theta = H_{c2 \perp ab}, \qquad (3)$$

where $\gamma' \simeq ed^2/6$. This expression is similar to the one given above for thin-film superconductors proposed by Tinkham [12] and Harper and Tinkham [25], but the coefficient γ' is now a material constant and hence temperature-independent. This equation is valid over a wide temperature region except for temperatures in the vicinity of T_c (see below). From a rough estimation from the experimental data in Fig. 3, we obtain the temperature-independent value $\gamma' = H_{c2 \perp ab}/H^2_{c2 \parallel ab} \simeq 0.0068 \text{ T}^{-1}$.

For small θ, we do not observe the expected cusp-like structure for the 2D model described by Eq. (3). In practice, the CuO_2 layers in the crystal are slightly misoriented with respect to the distribution of c-axis orientations. Moreover, defects may cause the enhancement of a link between layers and thus increase the effective thickness of the superconducting layers. Such crystal imperfections have no influence for high angles θ. For small θ, the expression for the angular dependence of the upper critical field $H_{c2}(\theta)$ can be rewritten with a Gaussian distribution of the c-axis orientations on a sphere

$$H_{c2}(\theta) = \frac{\beta}{\gamma'}\int_0^\infty du\, u\, e^{-\beta u^2}\frac{\sin\sqrt{\theta^2 + u^2}}{\cos^2\theta}$$
$$\times \left[\sqrt{1 + \frac{4H_{c2 \perp cb}\gamma'\cos^2\theta}{\sin^2\sqrt{\theta^2 + u^2}}} - 1\right], \qquad (4)$$

where $\beta \gg 1$ determines the angular width in the misalignment of the CuO_2 layers and the possible existence of shorted layers in the crystal. The solid curves shown in Fig. 3 are fits to Eq. (4) to our experimental data for sample no. 1 using β as a temperature independent parameter. The inset shows the same data for samples nos. 2 and 3. With the dashed lines, we have shown the cusp-like structure for $\beta \longrightarrow \infty$.

Using this analysis (at $\beta \longrightarrow \infty$) of the critical-field data, we obtained the same parameter $\gamma' = 0.0021 \pm 0.0001 T^{-1}$ for samples nos. 1, 2, and 3. Because the angular within the misalignment of the CuO_2 layers in the investigated crystals is much less than we obtained from the parameter γ' (these crystals showed X-ray rocking curves with a width of about $0.1°$–$0.3°$), this means that even a small proportion of the shorted layers is of first importance. From this value of γ' we evaluate the effective thickness of the superconducting layers $d \simeq \sqrt{6\hbar c\gamma'/e} = 2.7 \times 10^{-7}$. This value is close to the lattice parameter along the c-axis (2.46×10^{-7} cm), which looks reasonable. The critical-field anisotropy

$\gamma = H_{c2 \parallel ab}/H_{c2 \perp ab}$ now depends on temperature. Because the temperature dependence in Eq. (3) is only determined by the temperature dependence of $H_{c2 \perp ab}$ ($\sim 1 - T/T_c$ for $T_c - T \ll T_c$), one gets $\gamma \sim 1/\sqrt{1 - T/T_c}$. From measured values of $H^*_{c2 \perp ab}(T)$ data and the value of γ', we determined the magnitude of $H^*_{c2 \parallel ab}(T)$. Using a linear extrapolation of $H^*_{c2 \parallel ab}(T)$ and $H^*_{c2 \perp ab}(T)$ from T_c to zero temperature, we found $H^*_{c2 \parallel ab}(0) \simeq 90$ T and $H^*_{c2 \perp ab}(0) \simeq 16$ T for sample nos. 1 and 2, yielding $H^*_{c2 \parallel ab}/H^*_{c2 \perp ab} \simeq 5.6$ at $T = 0$ K.

The thin-film approximation ($\xi_c < s$) holds for $H_{c2}(\theta)m_c/m_{ab} > 1/\gamma'$. Near T_c with $H_{c2} \sim 1 - T/T_c$ and at a sufficiently large mass ratio m_c/m_{ab}, there is only a narrow region near T_c where this inequality does not hold, and an effective mass approach with a diffusion tensor becomes more adequate. In the studied crystals at $T = 6.8$ K, $H^*_{c2 \perp ab} = 2.9$ T, $\rho_c/\rho_{ab} = 2 \times 10^4$, and $\gamma = 0.0021$. This condition only breaks down at $1 - T/T_c \simeq 0.002$ a limit which may not be reached in view of the broadening of the superconducting transitions.

In conclusion, the effective-mass approximation is not suitable for layered superconductors with a very low transparency between the superconducting layers. In a magnetic field parallel to a layer, the vortex cross section has an elliptical shape with the small half-axis much less than the lattice parameter along the c-axis of the crystal. For this high degree of anisotropy, the proposed model of weakly coupled superconducting layers allows one to explain the observed angular dependence of the upper critical field.

REFERENCES

1. A. P. Mackenzie, S. R. Julian, G. G. Lonzarich, *et al.*, Phys. Rev. Lett. **71**, 1238 (1993).

2. M. S. Osofsky, R. J. Soulen, Jr., S. A. Wolf, *et al.*, Phys. Rev. Lett. **71**, 2315 (1993).

3. D. J. C. Walker, O. Laborde, A. P. Mackenzie, *et al.*, Phys. Rev. B **51**, 9375 (1995).

4. K. Karpinska, A. Malinowski, Marta Z. Cieplak, *et al.*, Phys. Rev. Lett. **77**, 3033 (1996).

5. N. R. Werthamer, E. Helfand, and P. C. Hohenberg, Phys. Rev. **147**, 295 (1966).

6. Y. Ando, G. S. Boebinger, A. Passner, *et al.*, Phys. Rev. B **60**, 12 475 (1999).

7. Yu. N. Ovchinnikov and V. Z. Kresin, Phys. Rev. B **52**, 3075 (1995).

8. G. Kotliar and C. M. Varma, Phys. Rev. Lett. **77**, 2296 (1996).

9. T. Koyama and M. Tachiki, Physica C (Amsterdam) **263**, 25 (1996).

10. A. Schilling, R. Jin, J. D. Guo, and H. R. Ott, Phys. Rev. Lett. **71**, 1899 (1993).

11. V. G. Kogan, Phys. Rev. B **24**, 1572 (1981).

12. M. Tinkham, Phys. Rev. **129**, 2413 (1963).

13. B. Y. Jin, J. B. Ketterson, E. J. McNiff, *et al.*, J. Low Temp. Phys. **69**, 39 (1987).

14. D. E. Farrell, J. P. Rice, D. M. Ginsberg, and J. Z. Liu, Phys. Rev. Lett. **64**, 1573 (1990).

15. B. Lundqvist, O. Rapp, and M. Andersson, Phys. Rev. B **62**, 3542 (2000) and references therein.

16. T. T. M. Palstra, B. Batlogg, L. F. Schneemeyer, *et al.*, Phys. Rev. B **38**, 5102 (1988).

17. R. Marcon, E. Silva, R. Fastampa, and M. Giura, Phys. Rev. B **46**, 3612 (1992).

18. M. J. Naughton, R. C. Yu, P. K. Davies, *et al.*, Phys. Rev. B **38**, 9280 (1988).

19. V. P. Martovitsky, J. I. Gorina, and G. A. Kaljushnaia, Solid State Commun. **96**, 893 (1995); J. I. Gorina, G. A. Kaljushnaia, V. P. Martovitsky, *et al.*, Solid State Commun. **108**, 275 (1998).

20. S. I. Vedeneev, A. G. M. Jansen, E. Haanappel, and P. Wyder, Phys. Rev. B **60**, 12 467 (1999).

21. R. V. Coleman, G. K. Eiserman, S. J. Hillenius, *et al.*, Phys. Rev. B **27**, 125 (1983).

22. J. A. Woollam and R. B. Somoano, Phys. Rev. B **13**, 3843 (1976).

23. R. A. Klemm, A. Luther, and M. R. Beasley, Phys. Rev. B **12**, 877 (1975).

24. W. Lawrence and S. Doniach, in *Proceedings of the 12th International Conference on Low Temperature Physics, Keigaku, Tokyo, 1971*, Ed. by E. Kanda, p. 361.

25. F. E. Harper and M. Tinkham, Phys. Rev. B **172**, 441 (1968).

Collective State of Interwell Excitons in GaAs/AlGaAs Double Quantum Wells under Pulse Resonance Excitation

A. V. Larionov[1, *], V. B. Timofeev[1], J. Hvam[2], and K. Soerensen[2]

[1] *Institute of Solid-State Physics, Russian Academy of Sciences, Chernogolovka, Moscow oblast, 142432 Russia*
*e-mail: larionov@issp.ac.ru
[2] *Microelectronic Centre, DK 2800 Lyngby, Denmark*
Received January 18, 2002

The time evolution and kinetics of photoluminescence (PL) spectra of interwell excitons in double GaAs/AlGaAs quantum wells (n–i–n structures) have been investigated under the pulse resonance excitation of intrawell 1sHH excitons using a pulsed tunable laser. It is found that the collective exciton phase arises with a time delay relative to the exciting pulse (several nanoseconds), which is due to density and temperature relaxation to the equilibrium values. The origination of the collective phase of interwell excitons is accompanied by a strong narrowing of the corresponding photoluminescence line (the line width is about 1.1 meV), a superlinear rise in its intensity, a long time in the change of the degree of circular polarization, a displacement of the PL spectrum toward lower energies (about 1.5 meV) in accordance with the filling of the lowest state with the exciton Bose condensate, and a significant increase in the radiative decay rate of the condensed phase. The collective exciton phase arises at temperatures $T < 6$ K and interwell exciton densities $n = 3 \times 10^{10}$ cm^{-2}. Coherent properties of the collective phase of interwell excitons and experimental manifestations of this coherence are discussed. © *2002 MAIK "Nauka/Interperiodica"*.

PACS numbers: 78.67.De; 78.55.Cr; 71.35.Lk; 78.47.+p,

1. In the last decade, double quantum wells (DQWs), p–i–n, n–i–n heterostructures, superlattices, and other tunnel-coupled quantum systems have been an object of intensive experimental and theoretical studies [1–10]. Interest in these systems is due to the possibility of separating (both in the real and momentum spaces) electrons and holes in the neighboring quantum wells followed by the formation of spatially indirect or interwell excitons (IEs) due to the Coulomb interaction. In particular, it was shown in the recent article by Berman and Lozovik [11] that, in spite of the dipole–dipole repulsion of IEs, the condensed dielectric phase of excitons may become a stable state in the electron–hole system at certain critical parameters, such as the IE dipole moment, IE density, and temperature. As applied already to real two-dimensional systems (see [12]), it is important to have a confinement in the quantum-well plane in order to reach the required critical exciton densities. As was already stated in a series of experimental works by Butov [13, 14], stimulated exciton scattering may serve as one of the manifestations of this dielectric exciton phase. This scattering manifests itself as a strong rise in the rate of exciton scattering to the lowest energy state with increasing exciton density due to the Bose nature of excitons.

This work is devoted to studying the time evolution of photoluminescence (PL) spectra and the degree of circular polarization of interwell excitons under their resonance excitation via intrawell 1sHH excitons. Previously (see [15, 16]), we showed that interwell excitons in n–i–n DQWs with a thin (four monolayers) AlAs barrier at low temperatures (2 K) and high densities (of order $n \sim 3 \times 10^{10}$ cm^{-2}) exhibit unusual properties, which, in our opinion, can be explained within the framework of collective behavior caused by the Bose nature of excitons. The results obtained can be summarized by the following: with increasing density of the optical excitation power, which increases the IE concentration, the intensity of the corresponding PL line increases superlinearly, the line itself becomes strongly narrowed and somewhat shifts toward the long-wavelength, which is accompanied by the threshold appearance and the superlinear growth of the degree of circular polarization. This phenomenon turned out to be very sensitive to temperature. We did not observe a sharp boundary in temperature, but all the events took place at $T \leq 6$ K. The aim of this work was to further investigate the previously discovered event with the time resolution of the origination and development of the collective IE phase and the kinetics of its radiative decay.

2. An n–i–n GaAs/AlGaAs heterostructure with a double GaAs/AlAs/GaAs quantum well (the width of GaAs wells ≈120 Å, and the width of the AlAs barrier ≈11 Å) was studied. The structure was grown by molecular-beam epitaxy on an n-type doped GaAs substrate (the concentration of the doping Si impurity was 10^{18} cm^{-3}) with the (001) crystallographic orientation. First, a 0.5-µm Si-doped (10^{18} cm^{-3}) GaAs buffer layer was grown on the substrate. Next, an insulating AlGaAs

($x = 0.33$) layer 0.15 µm thick was arranged. Next, GaAs/AlAs/GaAs DQWs were grown. An insulating AlGaAs layer 0.15 µm thick was arranged after the DQWs. Then, a 0.1-µm Si–doped (10^{18} cm^{-3}) GaAs layer was located. The entire structure was closed with a 100-Å GaAs layer. Mesas 1×1 mm^2 in size were made on the structure by the lithographic technique. Metal contacts of an Au + Ge + Pt alloy were deposited on the buffer layer and the doped layer on the upper part of the mesa.

Time-resolved spectra and PL decay curves were studied under conditions of pulse resonance excitation of intrawell (direct) excitons on heavy holes using a tunable femtosecond Ti-sapphire laser. To excite the required narrow spectral range (the 1sHH exciton state), the laser beam was previously passed through a dispersive medium with positive dispersion (diffraction grating), which resulted in its spectral narrowing and changed its duration (from 100 fs to 1 ps). With the aim of optical orientation of the angular momentum in the exciton, circular and linearly polarized resonance excitation was used. The time evolution of spectra and the kinetics of intensities were measured by a high-speed photomultiplier and a time-correlated photon counting system providing a time resolution of 400 ps.

3.1. Figure 1 demonstrates the time evolution of PL spectra under pulse excitation measured with various time delays relative to the exciting laser pulse at $T \simeq 2$ K and the applied voltage $U = +0.5$ V. Time-resolved spectra were detected under excitation by circularly polarized light (σ^+ component, full curves) in resonance with the 1sHH exciton and were analyzed in the σ^+ and σ^- circular polarizations. The excitation power density was selected in such a way that, on integrating over all laser pulses, the PL line width was a minimum at the highest degree of circular polarization. This condition was fulfilled at the peak power density ~30 kW/cm^2. An estimation of the IE concentration in this case gives the value $n \sim 3 \times 10^{10}$ cm^{-2}. It is under these conditions that, as was shown in [15], the collective properties of IEs are most pronounced.

At zero delays, the IE PL line is strongly polarized (more than 70%) on the high-energy side and has a width of about 3 meV. As the time delay increases, the line intensity increases superlinearly, and the line narrows and somewhat displaces toward the long-wavelength part of the spectrum. At delays of 5–6 ns, its width is a minimum and comprises about 1.1 meV. The maximum intensity of the IE PL line is reached at delays of about 3 ns. This time is necessary for the formation of IE upon the resonance tunneling of electrons and holes to the neighboring quantum wells and their relaxation in energy to the equilibrium values of density and temperature. This behavior of the IE PL line is also demonstrated by luminescence decay curves (see inset in Fig. 1). It is evident in the figure that it takes about 2.5–3 ns after the arrival of a laser pulse to attain the maximum intensity of the PL line. In this case, the max-
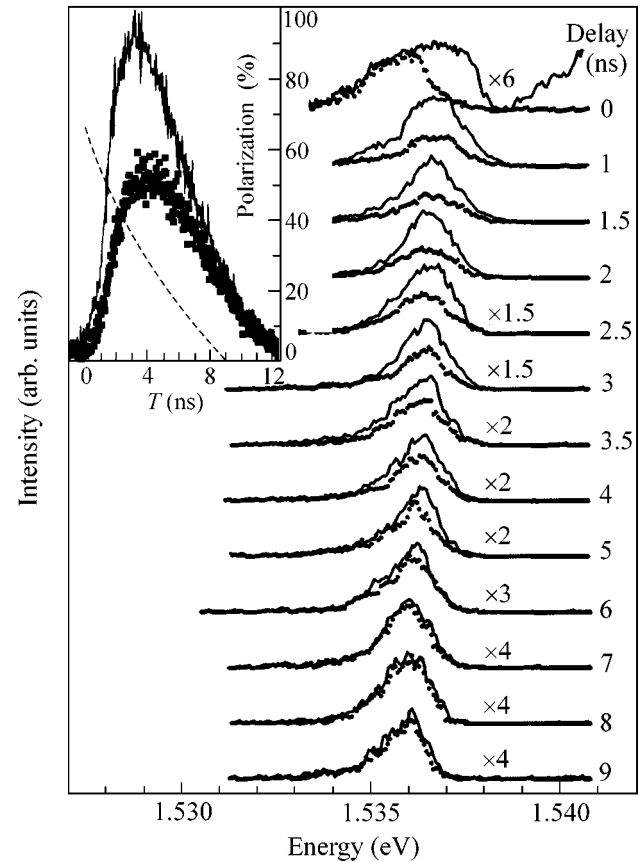

Fig. 1. Time-delayed IE PL spectra (numbers to the right of the spectra correspond to the time delay relative to the laser pulse in ns) under the resonance excitation of the direct 1sHH exciton by circularly polarized light (σ^+, full curves) integrated over 1 ns and recorded at an applied bias of +0.5 V, $T = 2$ K, and $P = 30$ kW/cm^2. The inset displays IE PL decay curves (σ^+, full curves, and σ^-, square symbols) for detection at the spectral position of 1.5365 eV. The dashed curve (the scale on the right) gives the degree of circular polarization.

imum PL intensity in the other (σ^-) polarization is additionally displaced with respect to the beginning of the laser pulse action by approximately 1 ns. At the same time, the maximum degree of circular polarization corresponds to the beginning of the laser pulse action.

The time evolution of the degree of circular polarization reflects the process of IE spin relaxation. It is evident in Fig. 1 that this process is different along the PL line contour. In the first nanosecond after the arrival of a laser pulse, the IE PL line is strongly polarized only on the high-energy side of the spectrum. Further, the degree of polarization remains equal along the entire line contour for approximately 3 ns. Then, only the high-energy part of the spectrum remains polarized. We recorded PL decay curves for different spectral positions along the line contour. The time of the change of the degree of circular polarization (spin relaxation time) at the PL line maximum and in its red edge differs
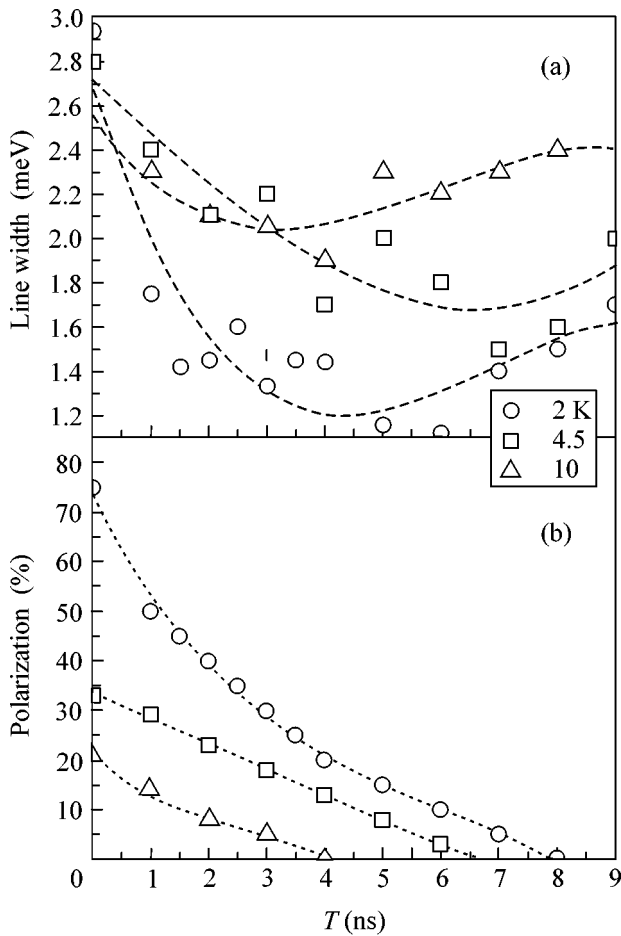
Fig. 2. (a) Temperature dependence of the IE PL line width as a function of time delay at an applied bias of +0.5 V, $T =$ 2 K, and $P = 30$ kW/cm^2. Dashed curves are given for convenience. (b) Temperature dependence of the degree of circular polarization of the IE PL line under excitation by circularly polarized light (σ^+) as a function of time delay for the spectral position of 1.5365 eV. Dashed curves are given for convenience.

by a factor of 1.5; that is, it equals 4.3 and 2.9 ns, respectively. Temperature is an important factor that, along with the excitation power density, affects all the kinetic events in which the IE participates. Figure 2 displays the width of the PL line at its half-height and the degree of circular polarization as functions of temperature. The high sensitivity of the PL line width to variations of temperature is well pronounced already from 2 to 4.5 K. There is no such strong narrowing of the line with increasing delay in the time dependences at $T =$ 4.5 K, and the dependence itself is not nonmonotonic, as it is at $T = 2$ K. At $T = 10$ K, the effect of line narrowing is virtually absent. Simultaneously, the behavior of the degree of circular polarization also changes significantly. The initial degree of circular polarization at $T =$ 4.5 K is only about 30% (more than 70% at $T = 2$ K); it drops monotonically, and becomes equal to zero at delays of more than 5 ns. At $T = 10$ K, the maximum

degree of circular polarization is less than 20%, and the line polarization vanishes after 3 ns.

2. We also measured the time evolution of IE PL spectra under resonance excitation by linearly polarized light followed by a time-resolved analysis of the degree of circular polarization. The plane of laser polarization coincided with the $\langle 110 \rangle$ crystallographic direction (see [16]).

Figure 3 illustrates time-delayed IE PL spectra at $T \simeq 2$ K and the applied voltage $U = +0.5$ V. As is the case under excitation by circularly polarized light at zero delays, the width of the IE PL line at the half-height is ~3 meV, but this line is strongly polarized (60%) along almost the entire line contour. As the delay increases, it also increases superlinearly and displaces toward lower energies (about 1 meV). After 4 ns, when the equilibrium density and temperature are attained, the IE PL line becomes as narrow as possible (1.2 meV), and the degree of circular polarization reaches saturation at a value of about 25%. The time evolution of the degree of circular polarization under excitation by linearly polarized light is also very sensitive to temperature (see Fig. 4). The degree of circular polarization does not exceed 30% even at $T = 4.5$ K; it drops monotonically, becoming negligibly small after 7 ns, and the PL line itself is polarized preferentially on the violet side. The events develop even faster at $T =$ 6 K: the maximum degree of circular polarization is about 15%, and it tends to zero at delays longer than 4 ns. Simultaneously, as the time delay changes, the PL line, whose initial width is about 3 meV, narrows at $T =$ 4.5 K by 75% (almost 2.5 times at $T = 2$ K) and by less than 40% at $T = 6$ K. The shift toward the long-wavelength part of the spectrum at $T = 4.5$ K comprises less than 0.5 meV and is absent at $T = 6$K.

Thus, as the time delay increases, the IE Pl line displaces toward the long-wavelength part of the spectrum, narrowing to the highest degree within 3–4 ns after the laser pulse action. Its degree of circular polarization (60–70%) gradually decreases to zero in a nonmonotonic way under excitation by circularly polarized light and reaches saturation (25%) under excitation by linearly polarized light. The time evolution of the line shift, width, and degree of circular polarization observed experimentally is critical with respect to temperature. With increasing temperature, the shift strongly decreases, the line width exhibits no dramatic change, the initial degree of circular polarization markedly decreases, and the spin relaxation time becomes significantly shorter. All the events indicated above take place in the temperature range up to $T_c \leq 6$ K.

4. All the experimental results outlined above confirm the suggestion that we made previously (see [15]) about the collective nature of the event that occurs with interwell excitons at low temperatures. Qualitatively, the pattern of the origination of the collective exciton phase can be described as follows. At low temperatures ($T \leq 2$ K), as the density of the optical excitation power
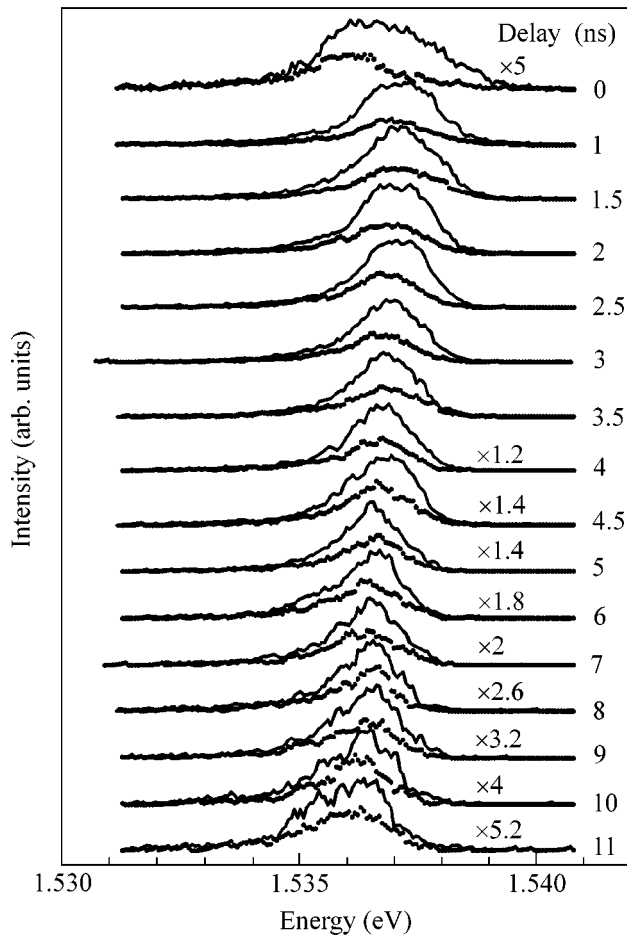
Fig. 3. Time-delayed IE PL spectra (numbers to the right of the spectra correspond to the time delay relative to the laser pulse in ns) under the resonance excitation of the direct 1sHH exciton by linearly polarized light integrated over 1 ns and recorded at an applied bias of +0.5 V, $T = 2$ K, and $P = 30$ kW/cm^2. Full curves correspond to σ^+ circular polarization, and dotted curves correspond to σ^- circular polarization.

Fig. 4. (a) Temperature dependence of the IE PL line width under excitation by linearly polarized light as a function of time delay at an applied bias of +0.5 V, $T = 2$ K and $P = 30$ kW/cm^2. Dashed curves are given for convenience. (b) Temperature dependence of the degree of circular polarization of the IE PL line under excitation by linearly polarized light as a function of time delay for the spectral position of 1.5365 eV.

increases, IEs fill the potential relief in the quantum-well plane, which arises from residual impurities, defects, and other structural imperfections. This is manifested as a narrowing of the PL line with an increase in pumping, which ceases to reflect the statistical distribution of fluctuation amplitudes of the random potential. In our opinion, the sharp narrowing of the PL line and the superlinear rise in its intensity cannot be associated with only the attainment of the percolation threshold by IEs, because this event is very sensitive to temperature, though it has no distinct temperature boundary. Berman and Lozovik showed [11] that a sufficiently dense system of IEs at certain values of the dipole moment of the interwell exciton could condense into a dielectric phase in spite of the dipole repulsion among such excitons. An essential amendment was made in [12], whose authors indicated that such a condensation in real systems can most probably occur in regions with confine-
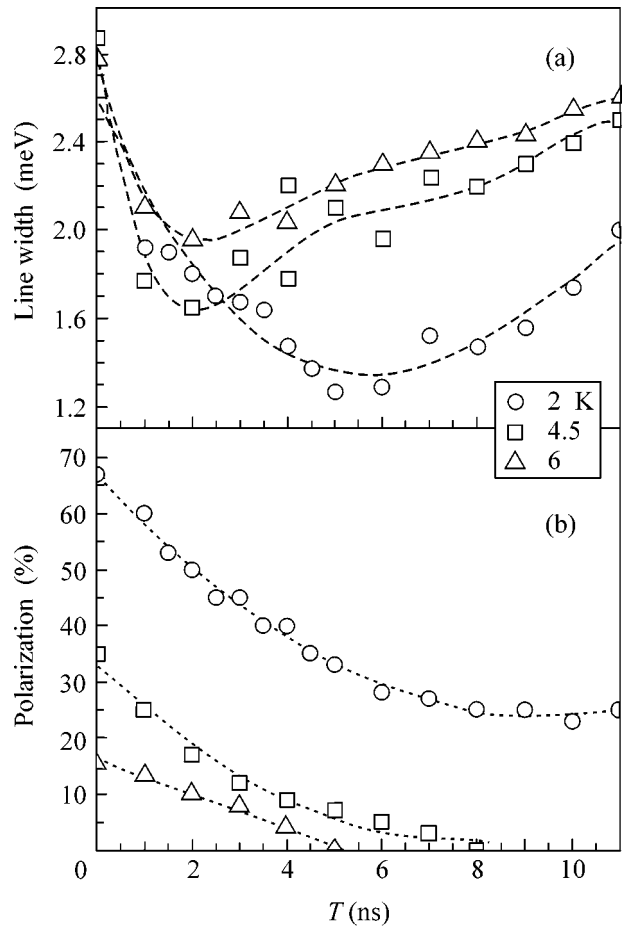
ments in the quantum-well plane. In the structures studied using the technique of epitaxial growth interrupted at heteroboundaries (in our case, the growth interruption time reached 2 min), large-scale fluctuations of the widths of quantum wells and barriers arise in the plane of heteroboundaries (the geometrical size of fluctuations in the direction of epitaxial growth is of the order of one monolayer). The characteristic linear scales of such fluctuations in the quantum-well plane reach one micrometer (see, for example, [17]). Because of such fluctuations, lateral wells or domains arise in the quantum wells themselves. As judged from the characteristic doublet structure in the photoluminescence excitation spectra of intrawell excitons measured in our samples, the depth of such domains reaches 1.5—2 meV. IEs can accumulate in these domains, because the boundaries of lateral domains prevent excitons from spreading randomly in the quantum-well plane. We

believe that it is in these domains where the density of excitons and their temperature reach critical values that the IEs demonstrate a collective behavior. Thus, as the exciton density increases, the random potential fluctuations become shielded to a certain extent. With a further increase in density exceeding the percolation threshold, the IEs become delocalized within macroscopically large domains; however, their motion is spatially confined by the dimensions of the domains in which excitons are accumulated. IEs are composite bosons; therefore, excitons must condense upon reaching the critical concentration and temperature values (analogue of Bose–Einstein condensation). Under conditions of the confinement in the quantum-well plane, the critical temperature at which this condensation takes place can be determined using the equation $T_c = \pi\hbar^2 N_{ex}/km_{ex}\ln(N_xS)$ ln (N_xS), where N_x is the exciton concentration, m_{ex} is the exciton mass, and S is the domain area. If it is assumed that the exciton mass $m_{ex} = 0.25m_0$ and the domain size is 0.5 µm^2, we obtain the critical temperature $T_c = 3$ K for the densities $N_{ex} = 5 \times 10^{10}$ cm^{-2} used in our experiment. This is very close to the values observed experimentally. It should also be noted that the measurements under our experimental conditions are carried out simultaneously with several tens of domains with regard to the fact that the smallest geometrical size of the excitation spot on a sample from which luminescence spectra are detected is about 30 µm. Considering the dispersion of the lateral sizes of domains and the integration of spectra from domains differing in lateral size, we are not surprised that we do not observe a sharp threshold of critical behavior in temperature in the experiments described above. For the same reasons, the smallest observed luminescence line width (about 1 meV) is inhomogeneous, because domains differing in size contribute to the line width. At the same time, the sharp narrowing of the interwell exciton luminescence line observed experimentally at $T < T_c$ ($T_c \sim 6$ K) and the long-wavelength shift of this line (about 1.5 meV) in accordance with the filling of the lowest energy state in the domain are clear manifestations of Bose properties of excitons.

The condensed IE phase must exhibit coherent properties. This means that IEs must possess the same phase on the scales of the de Broglie wavelength, which is close to the linear domain sizes. In our opinion, this phase coherence of excitons must, in its turn, affect the radiative annihilation rate, and this rate must increase. It is clearly evident from the kinetics of luminescence spectra that the lifetime of the collective exciton state is more than an order of magnitude shorter than the luminescence decay time of localized IEs. Thus, the increase in the radiative decay rate of IEs and the resulting increase in the degree of circular polarization of luminescence are particular manifestations of the coherence of the collective exciton state.

Note in conclusion that, experiments on measuring luminescence spectra from single domains with the use of near-field optics or scanning tunneling optical microscopy for this purpose are of special interest in the context of the results discussed above. We expect that more drastic spectral changes should be observed in this case near the critical temperature and that the homogeneous luminescence line width in the condensed phase must comprise no more than several tens of microelectron volts. In the case of weak tunnel coupling of two domains containing coherent exciton phases, phenomena similar to the Josephson effect must be observed: luminescence intensity beats and rotation of the plane of polarization.

REFERENCES

1. E. Yu. Lozovik and V. I. Yudson, Zh. Éksp. Teor. Fiz. **71**, 738 (1976) [Sov. Phys. JETP **44**, 389 (1976)].
2. T. Fukuzawa, E. E. Mendez, and J. M. Hong, Phys. Rev. Lett. **64**, 3066 (1990).
3. J. E. Golub, E. E. Mendez, J. P. Harbison, and L. T. Flores, Phys. Rev. B **41**, 8564 (1990).
4. J. A. Kash, M. Zachau, E. E. Mendez, *et al.*, Phys. Rev. Lett. **66**, 2247 (1991).
5. L. V. Butov, A. Zrenner, G. A. Abstreiter, *et al.*, Phys. Rev. Lett. **73**, 304 (1994); L. V. Butov, in *Proceedings of the 23rd International Conference on Physics of Semiconductors, Berlin, 1996.*
6. V. B. Timofeev, A. I. Filin, A. V. Larionov, *et al.*, Europhys. Lett. **41**, 435 (1998).
7. V. B. Timofeev, A. V. Larionov, A. S. Ioselevich, *et al.*, Pis'ma Zh. Éksp. Teor. Fiz. **67**, 630 (1998) [JETP Lett. **67**, 613 (1998)].
8. V. V. Krivolapchuk, E. S. Moskalenko, A. L. Zhmodikov, *et al.*, Solid State Commun. **111**, 49 (1999).
9. D. Yoshioka and A. H. MacDonald, J. Phys. Soc. Jpn. **59**, 4211 (1990).
10. X. M. Chen and J. J. Quinn, Phys. Rev. Lett. **67**, 895 (1991).
11. Yu. E. Lozovik and O. L. Berman, Zh. Éksp. Teor. Fiz. **111**, 1879 (1997) [JETP **84**, 1027 (1997)].
12. Xuejun Zhu, P. B. Littlewood, M. S. Hybersen, and T. Rice, Phys. Rev. Lett. **74**, 1633 (1995).
13. L. V. Butov, A. Imamoglu, A. V. Mintsev, *et al.*, Phys. Rev. B **59**, 1625 (1999).
14. L. V. Butov, A. L. Ivanov, A. Imamoglu, *et al.*, Phys. Rev. Lett. **86**, 5608 (2001).
15. A. V. Larionov, V. B. Timofeev, J. M. Hvam, and C. Soerensen, Pis'ma Zh. Éksp. Teor. Fiz. **71**, 174 (2000) [JETP Lett. **71**, 117 (2000)].
16. A. V. Larionov, V. B. Timofeev, J. M. Hvam, and C. Soerensen, Zh. Éksp. Teor. Fiz. **117**, 1255 (2000) [JETP **90**, 1093 (2000)].
17. S. W. Brown, T. A. Kennedy, D. Gammon, and E. S. Snow, Phys. Rev. B **54**, R17339 (1996).

Translated by A. Bagatur'yants

Nanotube Devices: A Microscopic Model

K. A. Bulashevich[1] and S. V. Rotkin[2, *]

[1] *St. Petersburg State Technical University, ul. Politekhnicheskaya 29, St. Petersburg, 195251 Russia*
[2] *Beckman Institute, UIUC, Urbana, IL 61801, USA and Ioffe Institute,*
ul. Politekhnicheskaya 26, St. Petersburg, 194021 Russia
*e-mail: rotkin@uiuc.edu
Received January 21, 2002

A microscopic model is developed for calculating electrostatic properties of nanotube devices. It is shown that the quantum-mechanical approach yields the same results as the statistical calculation in the limit of a thin tube suspended over a conducting gate at a distance exceeding the nanotube radius. A closed analytic expression is obtained for the atomistic capacitance of a straight nanotube and for a nanotube with a modest curvature. This method allows the fast and exact calculation of device parameters for the nanotube electromechanical systems and nanotube electronic devices. © *2002 MAIK "Nauka/Interperiodica".*

PACS numbers: 85.35.Kt; 61.46.+w

The high strength of carbon nanotubes, along with low lateral bending stiffness, a size comparable with the scale of modern nanotechnologies, and unique electronic properties provide good prerequisites for their use in nanotube electromechanical systems (NEMS).

The functioning of nanotweezers composed of two multiwall nanotubes with their spacing controlled by an applied voltage was demonstrated experimentally in 2001 [1]. In 2000, it was suggested that a memory cell can be created on the basis of two crossing nanotubes [2].

However, the available models and programs for simulating device characteristics of micron-scale electromechanical systems cannot be used for the calculation of NEMS without substantial modification. At the same time, *ab initio* calculations of nanotube electronic and electromechanical devices seem to be impossible. Therefore, the development of an appropriate physical model is quite topical. Continuum approximations are most promising for modeling such devices, because they provide a high accuracy and minimal computational expenses. In this work, a microscopic model is suggested for the description of electrostatic properties of NEMS, which, in conjunction with the parameterization previously developed for the continuum elasticity of nanotubes [3] and with the continuum theory of van der Waals forces, allows the derivation of basic equations for the analysis of the operation of nanotube devices in nanoelectronics.

In this work, we will apply the electrostatic model to the analysis of equilibrium charge-carrier distribution over the nanotube surface, which is necessary for modeling NEMS operation (Fig. 1). In NEMS, the nanotube shape is determined by the balance between the electrostatic and elastic forces acting on the tube. For weak bending, typical of NEMS, the elastic forces can be considered within the framework of a one-dimensional continuum model [4]. To determine the electrostatic forces, one should calculate the distribution of a charge accumulated on the nanotube under the action of the applied voltage; i.e., one should calculate the distributed capacitance. At present, the conducting nanotubes are described using classical electrostatics of macroscopic conductors, while the quantum-size effects are disregarded. This work fills this gap and gives an estimate for the resulting corrections. The capacitance of a weakly bent nanotube situated over a flat conducting contact (gate) is expressed in terms of the capacitance of a metallic cylinder of the same shape.

Theoretical model. First, we ignore all contact phenomena occurring at the contact–nanotube boundary.[1] Second, we ignore the transverse polarization of the nanotube and assume that the charge density depends, generally, only on the curvilinear coordinate l along the nanotube axis.[2]

The key approximation consists in the use of a local statistical relation between the acting potential and charge density

$$\rho(l) = e \int_0^{E_0(l)} \nu(E)\, dE, \qquad (1)$$

---

[1] In our model, the difference $\Delta W = W_M - W_{NT}$ in work functions of an electron in the contact material and the nanotube can be taken into account. In doing so, the relation for E_0 should be replaced by $E_0(l) = \Delta W - e\phi^{\text{act}}(l)$.

[2] The estimate of the relative contribution to the capacitance from the transverse polarization gives $\dfrac{R^2}{4h^2}\dfrac{1}{\log(2h/R)} \ll 1$.
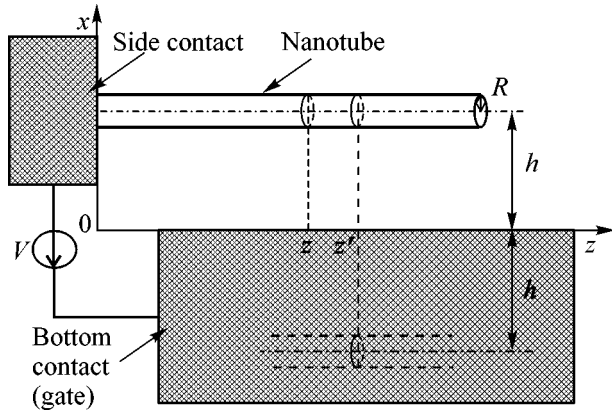
Fig. 1. Scheme of a nanotube electromechanical device. The image charge in the bottom contact (gate) is shown by dashes.
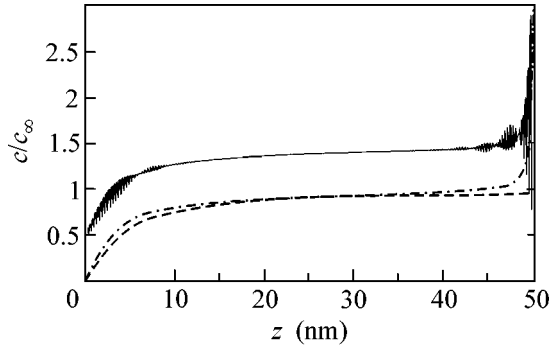

Fig. 2. Linear capacitance of a straight nanotube (in units of c_∞) vs. the distance (in nm) to the side contact. The results of quantum-mechanical calculation (solid curve) are shifted upward, because they coincide with the results of statistical calculation (dot-and-dash curve) to within oscillations (see text). The dashed curve is an approximation (10). The nanotube height is 5 nm, its radius is 0.67 nm, and its length is 50 nm.

where $E_0(l) = -e\phi^{\text{act}}(l)$ is the electroneutrality level measured from the Fermi level of the side contact, $\phi^{\text{act}}(l)$ is the acting potential on the nanotube axis reckoned from the potential of the side contact, $\nu(E)$ is the density of electronic (hole) states in the nanotube, the energy E is measured from the electroneutrality level; and $e > 0$ is the absolute value of electron charge. This model was proposed by Odintsov and Tokura for considering the Schottky barrier between the contact and the nanotube [5]. Since the density of electron wave functions in the ring direction is constant if the transverse polarization is ignored, by the acting potential in all formulas should be meant its value averaged over the nanotube cross section.

For the conducting nanotubes, the density of states near the electroneutrality level is constant and equals $\nu_M = 8/3\pi b\gamma_0$. Here, $b = 0.14$ nm and $\gamma_0 = 2.7$ eV are the bond length and the hopping integral, respectively. Then, if the condition $e|\phi^{\text{act}}| \le \frac{3}{2}\gamma_0(b/R)$, where R is the nanotube radius, is met, the charge density linearly depends on the acting potential

$$\rho(l) = -e^2\nu_M\phi^{\text{act}}(l). \qquad (2)$$

The product of the density of states into the squared electron charge $e^2\nu_M = 3.2$ is the dimensionless parameter of our problem.

Expression (1) is written in the zero-temperature limit. However, since the density of states is constant, Eq. (2) also holds for the temperatures at which carrier thermal excitations to the next subband can be ignored.

To test the statistical model, we calculated the charge distribution on a straight armchair nanotube of finite length by solving the Poisson and Schrödinger equations self-consistently. The Schrödinger equation was solved in the tight-binding approximation [6]. The resulting charge density and the corresponding value calculated by the statistical model coincided to within quantum beats due to finiteness of the nanotube length (Fig. 2). Analogous beats were observed experimentally in [7].

Semi-infinite straight nanotube over flat contact. Let us consider a single-wall nanotube arranged parallel to the flat contact at a height h (Fig. 1). The voltage V is applied between the side and bottom contacts. We will reckon the acting potential from the side contact. Then, the potential of the bottom contact is $-V$ and the charge density on the nanotube is positive.

The Green's function $G(\mathbf{r}, \mathbf{r}')$ in the region bounded by two perpendicular planes is the sum of the potentials of a probe unit charge and three image charges. The acting potential can be written as

$$\phi^{\text{act}}(\mathbf{r}) = \phi^{\text{ext}}(\mathbf{r}) + 4\pi\int G(\mathbf{r}, \mathbf{r}')\rho(\mathbf{r}')d\mathbf{r}'. \qquad (3)$$

The first term in Eq. (3) is the potential created by two contacts with the voltage V applied to them in the absence of the nanotube. By integrating the Poisson equation for two perpendicular contacts, one obtains this term in the form

$$\phi^{\text{ext}}(\mathbf{r}) = \phi^{\text{ext}}(x, z) = -V\frac{2}{\pi}\arctan\left(\frac{z}{x}\right). \qquad (4)$$

The second term is the potential created by the nanotube charge and the image charges. Substituting Eq. (3) into Eq. (2) and taking into account that the nanotube

charge density depends only on z, one obtains the integral equation for the linear charge density

$$\frac{\rho(z)}{e^2\nu_M} + \int\limits_0^\infty F(z, z')\rho(z')dz' = -\phi^{ext}(z) \qquad (5)$$

with the one-dimensional Green's function

$$F(z, z') = \frac{1}{4\pi^2}$$
$$\times \int\limits_{-\pi}^{\pi}\int\limits_{-\pi}^{\pi} 4\pi G((z, R, \alpha), (z', R, \alpha'))d\alpha d\alpha' \qquad (6)$$

as a kernel, where α and α' are the angular coordinates of the points $\mathbf{r}$ and $\mathbf{r}'$ in the nanotube-fixed cylindrical system of coordinates. The quantity $F(z, z')$ is the energy of screened Coulomb interaction between two uniformly charged rings representing cross sections of a nanotube of radius R at distances z and z' from the side contact (Fig. 1). In Eq. (6), averaging is done over the angles α and α', because the acting potential in Eq. (2) means its average over the nanotube cross section.

If the distances z and z' to the side contact are much larger than the height h, the contribution from the image charges in the side contact to the one-dimensional Green's function is on the order of $2h^2/(z + z')^3$ and, hence, can be ignored in comparison with the influence of the image charge in the bottom contact. Then, the kernel depends only on the difference $\Delta z = |z - z'|$ and behaves as

$$F(z, z') = \frac{2}{\pi\Delta z}K\left(-\frac{4R^2}{|\Delta z|^2}\right) - \frac{1}{\sqrt{(\Delta z)^2 + 4h^2}}$$
$$\approx \begin{cases} \frac{1}{\pi R}\log\left(\frac{8R}{\Delta z}\right), & \Delta z \ll R, \\ \frac{1}{\Delta z}, & R \ll \Delta z \ll 2h, \\ \frac{2h^3}{(\Delta z)^3}, & \Delta z \gg 2h, \end{cases} \qquad (7)$$

where K is the complete elliptic integral of the first kind. Let us now determine the asymptotic value of the charge density at $z \longrightarrow \infty$. The right-hand side of Eq. (5) becomes equal to the applied voltage V, and the charge density becomes

$$\rho_\infty = -\phi_\infty^{ext}c_\infty \approx Vc_\infty^{met}(1 - c_\infty^{met}/e^2\nu_M). \qquad (8)$$

In Eq. (8), $c_\infty = (1/e^2\nu_M + 1/c_\infty^{met})^{-1}$ is the nanotube atomistic capacitance and the notation

$$c_\infty^{met} = \left(\int\limits_{-\infty}^\infty F(\Delta z)d\Delta z\right)^{-1} = \frac{1}{2\log(2h/R)} \qquad (9)$$

is introduced for the capacitance of a unit length of an infinite metallic cylinder of radius R situated at a height h parallel to the flat conducting contact. Thus, the relative correction to the classical capacitance is $-c_\infty^{met}/e^2\nu_M$. For the typical values $h = 5$ nm and $R = 0.67$ nm ([10, 10] armchair nanotube), this amounts to 8%. The correction to the capacitance is inversely proportional to the nanotube density of states, so that it is inversely proportional to the number of layers in multilayer nanotubes. The correction to capacitance weakly (logarithmically) depends on the ratio of the nanotube radius to the distance from the contact.

By analogy with [5], one can analytically calculate the charge-density Fourier component for the straight semi-infinite nanotube (see Appendix). However, for the bent nanotube one fails to obtain a solution in the closed form. Away from the side contact, the charge density changes slowly compared to the one-dimensional Green's function. For this reason, to find an approximate expression for the charge density as a function of the distance to the side contact, one may factor charge density outside the integral sign in Eq. (5). As a result, one arrives at the following approximate expression describing the behavior of the charge density as it approaches its asymptotic value ρ_∞ (see Appendix):

$$\rho(z) \approx -c_\infty\phi^{ext}(z). \qquad (10)$$

To make an estimate for engineering and calculating the characteristics of nanotube electronic and electromechanical devices, we suggest that the finite-length nanotube be divided into three regions: (i) near-contact region, where the screening effect of the image charge in the side contact should be taken into account, (ii) central region, where the charge density is determined by the screening effect of the image charges in the bottom contact (gate), and (iii) end region (only for nanotubes with a free edge), where the charge density is higher than in the central region.

For example, the charge density on the straight single-wall nanotube behaves as follows: it increases linearly on the length of order h near the side contact, asymptotically approaches the value ρ_∞ following the hyperbolic law, and again then increases on the length of order R near the nanotube end (Fig. 2). Correspondingly, the electric field component along the nanotube axis is equal to $c_\infty V/e^2\nu_M h$ in the near-contact region and decreases rapidly as $c_\infty Vh^2/e^2\nu_M hz^2$ in the central region. This approximation allows for the rapid calculation of the Coulomb forces when modeling NEMS.

Bent nanotube of finite length. Let the nanotube axis form be specified by the function $\mathbf{r}(l)$. The specific

charge density on the nanotube is determined by the equation

$$\frac{\rho(l)}{e^2 \nu_M} + \int_0^L F(l, l')\rho(l')dl' = -\phi^{\text{ext}}(\mathbf{r}(l)), \qquad (11)$$

where L is the nanotube length and, similarly to Eq. (6), the one-dimensional Green's function $F(l, l')$ is equal to the energy of a screened Coulomb interaction of two uniformly charged rings representing cross sections of the nanotube at distances l and l'.

By integrating with respect to dz' and introducing the function $F_1(z, z') = F(l, l')\sqrt{1 + h'(z')^2}$, where $h(z)$ is the x coordinate of a small nanotube element at a distance z from the side contact, one obtains the equation for the charge density in the form analogous to Eq. (5),

$$\frac{\rho(z)}{e^2 \nu_M} + \int_0^\infty F_1(z, z')\rho(z')dz' = -\phi^{\text{ext}}(h(z), z). \qquad (12)$$

Let us now find the approximate solution to Eq. (12) for a deformed nanotube. Let the nanotube be initially situated at a height h_0 parallel to the bottom contact and bent under the action of electrostatic forces. The nanotube height over the bottom contact, the kernel of Eq. (12), and the charge density can be written as

$$h = h_0 + \delta h, \quad F_1 = F_0 + \delta F, \quad \rho = \rho_0 + \delta\rho, \quad (13)$$

where F_0 and ρ_0 are, respectively, the kernel and the charge density for the straight nanotube at a height h_0. Note that $\delta F < 0$ for downbending, because the screening image charges in the bottom contact become closer to the nanotube in this case. Then, assuming that the nanotube bending is small, one obtains the following equation for the correction $\delta\rho$:

$$\frac{\delta\rho(z)}{e^2 \nu_M} + \int_0^\infty F_0(z, z')\delta\rho(z')dz'$$

$$= -\int_0^\infty \delta F(z, z')\rho_0(z')dz' - \frac{\partial\phi^{\text{ext}}}{\partial h}\delta h. \qquad (14)$$

As pointed out above, the charge density in the central region of the straight nanotube increases very slowly and tends to ρ_∞. One can then factor $\rho_0 \approx \rho_\infty$ outside the integral sign on the right-hand side of Eq. (14) for the central region of the nanotube because of a fast decrease in δF. Now, the function $F_0(z, z')$ in the integral on the left-hand side of Eq. (14) has a logarithmic singularity at $z = z'$ and rapidly decreases at $|z - z'| > 2h$ [see Eq. (7)]. Since we assume that the bending is small, while the capacitance logarithmically depends on the height, the charge density is a smooth function of the coordinate z. Then, the charge-density variation can also be factored outside the integral sign on the left-

hand side of Eq. (14). Introducing notation $E_x^{\text{ext}} = -\partial\phi^{\text{ext}}/\partial h$, one obtains the following expression for the correction to the charge density:

$$\delta\rho(z) = -Vc_\infty^2 \int_0^\infty \delta F(z, z')dz' + c_\infty E_x^{\text{ext}}\delta h. \qquad (15)$$

Therefore, the capacitance of the bent nanotube is

$$c(z) = c_\infty - c_\infty^2 \int_0^\infty \delta F(z, z')dz' + \frac{1}{V}c_\infty E_x^{\text{ext}}\delta h. \qquad (16)$$

As the density of states ν_M tends to infinity, our problem reduces to determining the specific capacitance of a metallic cylinder shaped like a nanotube. After the approximate solution of Eq. (12), for the bent metallic cylinder one has

$$c^{\text{met}}(z) = c_\infty^{\text{met}} - c_\infty^{\text{met}^2} \int_0^\infty \delta F(z, z')dz'$$

$$+ \frac{1}{V}c_\infty^{\text{met}} E_x^{\text{ext}}\delta h. \qquad (17)$$

Comparing Eqs. (16) and (17) with the use of Eq. (8) for c_∞ and retaining only the leading term in the correction to the capacitance, one obtains the following relation between the capacitance of the bent nanotube and the capacitance of a bent metallic cylinder:

$$c(z) \approx c^{\text{met}}(z)\left(1 - \frac{c^{\text{met}}(z)}{e^2 \nu_M}\right). \qquad (18)$$

Equation (18) generalizes Eq. (8).

Thus, we have found a simple relation between the capacitance of a weakly bent nanotube and the capacitance of a metallic cylinder of the same shape.

The results of our calculations allow one to formulate the following principles of modeling the electrostatic properties of electromechanical and electronic nanodevices based on single- and multiwall carbon nanotubes: (1) the equilibrium one-dimensional specific charge density at the tube surface is linearly related to the external potential, with the proportionality coefficient designated below as the nanotube atomistic capacitance; (2) the nanotube atomistic capacitance is determined not only by the intrinsic properties of the nanotube material (density of states at the Fermi level) but also by the geometry of a device (in NEMS, distance from the gate) because of the one-dimensional character of charge screening in the system; (3) the nanotube atomistic capacitance can be expressed analytically through the classical capacitance of a metallic cylinder *of the same* shape and through the density of states in the nanotube; the corresponding expression holds for a single-wall nanotube in the voltage range of a few volts and for modest deformations also having no

effect on the electronic structure of the tube; and (4) the resulting expressions can be used to avoid computational difficulties in calculating the electrostatic forces in NEMS with good accuracy. The further generalization of the theory to the case of nonequilibrium charge density will be helpful in deriving equations for the analysis of the operation of nanotube electronic devices.

APPENDIX

Closed expression for the charge density on a straight semi-infinite nanotube. Formally, the influence of the image charge in the side contact can be taken into account as follows. Let us continue the charge density ρ and the external potential ϕ^{ext} to the half-space $z < 0$ in an odd way. Then, Eq. (5) can be rewritten as

$$\frac{\rho(z)}{e^2 \nu_M} + \int_{-\infty}^{\infty} F_2(z, z')\rho(z')dz' = -\phi^{\text{ext}}(z), \qquad (19)$$

where the kernel F_2 does not contain terms corresponding to the image charges in the side contact:

$$F_2(z, z') = \frac{2}{\pi|z - z'|}K\left(-\frac{4R^2}{|z - z'|^2}\right)$$
$$- \frac{1}{\sqrt{(z - z')^2 + 4h^2}}. \qquad (20)$$

Since the kernel F_2 for the infinite straight nanotube depends only on the difference $\Delta z = z - z'$, the Fourier transform converts integral equation (19) into an algebraic equation. Then, the exact solution to Eq. (19) in

the k space has the form

$$\rho_k = -\frac{\phi_k^{\text{ext}}}{1/e^2\nu_M + 2\pi F_{2k}}, \qquad (21)$$

where ϕ_k^{ext} and F_{2k} are the Fourier components of the external potential and kernel, respectively:

$$\phi_k^{\text{ext}} = -i\frac{e^{-|k|h}}{\pi k}V, \qquad (22)$$

$$F_{2k} = \frac{1}{\pi}(I_0(kR)K_0(kR) - K_0(2hk)), \qquad (23)$$

where I_0 and K_0 are modified zero-order Bessel functions [8]. The approximation in Eq. (10) is obtained from Eq. (21) by the replacement of the kernel Fourier component F_{2k} by its zero-wave vector value $F_{20} = (1/\pi)\log(2h/R)$. Inasmuch as the Fourier component ϕ_k^{ext} of the external potential rapidly decreases with an increase in the wave vector, the resulting approximation is quite accurate.

REFERENCES

1. S. Akita, Y. Nakayama, S. Mizooka, *et al.*, Appl. Phys. Lett. **79**, 1691 (2001).
2. T. Rueckes, K. Kim, E. Joselevich, *et al.*, Science **298**, 94 (2000).
3. M. Dequesnes, S. V. Rotkin, and N. R. Aluru, Nanotechnology **13**, 120 (2002).
4. M. Dequesnes, S. V. Rotkin, and N. R. Aluru, Int. J. Comput. Electron. (in press).
5. A. A. Odintsov and Y. Tokura, J. Low Temp. Phys. **118**, 509 (2000).
6. M. S. Dresselhaus, G. Dresselhaus, and P. C. Eklund, *Science of Fullerenes and Carbon Nanotubes* (Academic, San Diego, 1996).
7. L. C. Venema, J. W. G. Wildoer, J. W. Janssen, *et al.*, Science **283**, 52 (1999).
8. *Handbook of Mathematical Functions with Formulas, Graphs and Mathematical Tables*, Ed. by M. Abramowitz and I. Stegun (National Bureau of Standards, Washington, 1964; Nauka, Moscow, 1979).

Translated by V. Sakun

=== **ERRATA** ===

Erratum: "The Efficiency of Repeaters Based on the Einstein–Podolsky–Rosen Effect for Quantum Cryptography in a Damping Channel"
[*JETP Letters* 74, no. 10, 517 (2001)]

S. N. Molotkov

PACS numbers: 03.67.Dd; 03.65.Ud

In the titled article, I criticized the work of L. M. Duan *et al.* {Nature 414, 413 (2001), quant-ph/0105105; ref. [4]} and argued that, to create a through EPR pair in the damping channel, an exponentially large number of attempts are required to generate the EPR pair, rather than a polynomially large number, as was stated in [4]. My arguments disregarded the presence of the quantum memory that was used in [4] and because of which the conclusion drawn in [4] about the polynomial increase in resources is correct.

I make my apology.

Translated by V. Sakun